



Article

A Transdisciplinary Approach for Analyzing Stress Flow Patterns in Biostructures

Reena Patel ^{1,*}, Guillermo Riveros ¹, David Thompson ², Edward Perkins ¹, Jan Jeffery Hoover ¹, John Peters ³ and Antoinette Tordesillas ⁴

¹ US Army Engineer Research and Development Center, Vicksburg, MS 39180, USA; Guillermo.A.Riveros@usace.army.mil (G.R.); Edward.J.Perkins@usace.army.mil (E.P.); Jan.J.Hoover@usace.army.mil (J.J.H.)

² Department of Aerospace Engineering, Mississippi State University, Starkville, MS 39762, USA; dst@ae.msstate.edu

³ Center for Advanced Vehicular Systems (CAVS), Mississippi State University, Starkville, MS 39762, USA; john@cavs.msstate.edu

⁴ School of Mathematics and Statistics, University of Melbourne, Parkville, Victoria 3010, Australia; atordes@unimelb.edu.au

* Correspondence: Reena.R.Patel@usace.army.mil; Tel.: +1-601-634-5430

Received: 27 March 2019; Accepted: 24 April 2019; Published: 26 April 2019

Abstract: This work presents a transdisciplinary, integrated approach that uses computational mechanics experiments with a flow network strategy to gain fundamental insights into the stress flow of high-performance, lightweight, structured composites by investigating the rostrum of paddlefish. Although computational mechanics experiments give an overall distribution of stress in the structural systems, stress flow patterns formed at nascent stages of loading a biostructure are hard to determine. Computational mechanics experiments on a complex model will involve a high degree of freedom thereby making the extraction of finer details computationally expensive. To address this challenge, the evolution of the stress in the rostrum is formulated as a network flow problem generated by extracting the node and connectivity information from the numerical model of the rostrum. The flow network is weighted based on the parameter of interest, which is stress in the current research. The changing kinematics of the system is provided as input to the mathematical algorithm that computes the minimum cut of the flow network. The flow network approach is verified using two simple classical problems. When applied to the model of the rostrum, the flow network approach identifies strain localization in tensile regions, and buckling/crushing in compressive regions.

Keywords: biostructure; rostrum; paddlefish; *Polyodon spathula*; maximum-flow/minimum-cut; stress patterns

1. Introduction

A fundamental understanding of the response of a structural system to external loading conditions is important in determining if the design is able to withstand the prescribed external load. Numerous methods are available to quantify the response of a structural system to external loads. Existing methods, such as acoustic emission [1–7] and digital image correlation [8–17], offer the capability to experimentally measure/quantify/determine strains/deformations. From a modelling perspective, there are continuum-based [18–20] and discrete- or lattice-based [21–23] approaches that not only satisfy the physical laws governing the systems, but also provide abundant information required for structural analysis. Finite element analysis has been used to study the mechanical properties of bioinspired structures. Flores-Johnson et al. [24] carried out simulations on bioinspired, nacre-like composite plates. Nacre, found in mollusk shells, is a biological material that shows remarkable mechanical performance

because of its hierarchical geometry spanning multiple length scales [25]. Flores-Johnson et al. [24] found that the nacre-like plates demonstrated superior performance as compared to standard bulk plates under blast loadings. Tran et al. [26] conducted a study to analyze the response of a bioinspired composite plate based on nacre structure subjected to underwater impulsive loading. They discovered that the bioinspired composite structure spread the damage over a larger area, thereby decreasing stress. Although a considerable amount of research is performed on biostructures and bioinspired structures, there is yet a lack of understanding on what imparts superior performance to biostructures. Numerical analysis provides the overall response of the structural system under an external loading condition. However, additional information is required to understand the influence of the local topology on the global structural response and overall performance of the system. To our knowledge, advanced mathematical algorithms have not been used with continuum-based models to gain fundamental insight into the structural response of biostructures. Since biostructures are geometrically optimized at the coarsest level of hierarchy, the information obtained at the local topology level provides insights that could be used to identify optimal geometrical configurations that impart superior characteristics to biostructures.

Any conceivable problem dealing with the transmission of information can be solved by abstraction to a network or a graph [27]. These abstractions involve representing the system in terms of a transmission medium and the internal details that block the information flow, i.e., flow bottlenecks. From this viewpoint, maximum flow and minimum cut are two of the most widely used algorithmic approaches in network flow theory [27]. Maximum flow governs the amount of information that can be transmitted through the network. Minimum cut embodies a set of edges in the network that form the bottlenecks to transmission. Tordesillas et al. examined the formation of bottlenecks in transmission of force through the contact network by applying network flow theory [27–29]. The location and formation of the bottlenecks are influenced by the local as well as global characteristics of the structural system. The early identification of bottlenecks in force transmission opens new avenues for detection, as well as manipulation of the approaching failure in granular systems.

Lefort et al. [30] used image analysis that employed an integration of a numerical model with Ripley's function [31] to identify patterns in the fracture process zone (FPZ) in a quasibrittle material. Macrocracks in a quasibrittle material are formed by the combination of microcrack propagation, interaction, and coalescence, situated within the FPZ. Ripley's function is used to characterize randomness in the spatial spreading of point distributions and to identify the spreading and development of diverse patterns, e.g., cell migration [31], tree [32] and plant [33] dissemination, and disease transmission [34]. Lefort's research could open up new paths that would result in nonlocal continuum modeling at the macroscale level.

The mathematical approaches used for dense granular systems and quasibrittle materials demonstrate that local topological interactions are a major contributor to the global structural response. To gain an understanding of failure mechanisms, it is essential to capture the activity around the failure site at the nascent stage of loading. Obtaining this insight at the onset of loading may provide insight into failure mechanisms and possibly suggest novel approaches to alter the process and location of failure. Additionally, if the location of the failure is identified earlier, there is a possibility of developing a relationship that aids in quantifying the external force required for the structural system to fail at that location. This knowledge can be used for designing new structural systems, and for the assessment of existing critical infrastructure.

Biostructures have, in general, demonstrated superior characteristics as they evolved to serve multiple and specific functions [35]. The biostructure of interest here is the snout, or rostrum, of the paddlefish (*Polyodon spathula*). This large North American freshwater fish is related to sturgeons. Unlike those fish with their short thick rostra, the paddlefish has an elongated, flattened rostrum that in adults may be in the range of 29–59% of its body length, and in breadth in the range of 8–17% of body length [36]. The rostrum was once believed to be a simple digging or stirring implement, but is now known to be a complex hydrodynamic and electrosensory structure [37]. This prominent structure is easily observed and is supported internally by a distinctive skeleton of ossified cartilage comprised of

large axial rods with two posterior buttresses at the base and with numerous small stellate elements lateral to the axis (Figure 1).

The rostrum's lattice-like architecture with complex geometry appears to contribute to its unique strength and resilience. This research is motivated by an earlier feasibility study that concluded that the nonuniform geometry of the rostrum is one of its toughening mechanisms used to mitigate failure [38]. Since biostructures in general and the paddlefish rostrum in particular are made of heterogeneous materials and also have hierarchical geometry, it is difficult to identify the major contributor to their superior structural response. A fundamental understanding of how this lattice-like architecture functions has the potential to provide novel insights into applications over a wide range of disciplines (e.g., protective panels, novel building materials, body and vehicle armor, and ship design, among other possible uses). This research seeks to use an integrated transdisciplinary approach that feeds information from computational mechanics experiments on biostructures to a mathematical algorithm to identify the patterns formed at the early stages of loading of the biostructure.

Patel et al. developed the methodology of using network theory with finite element analysis in their previous work [39], which used a single source and sink combination to analyze the stress flow pattern on the rostrum. They also presented the procedure of preparing the data in an appropriate format from finite element binary database files to an abstract mathematical domain in their recent publication [40]. Patel et al. have also developed bioinspired structural systems to analyze the relationship of structural resiliency and geometrical complexity [39]. This work extends their previous research to include a multiple combination of source and sink. Since the material is in the linearly elastic regime, the solution from the mathematical algorithm can be superimposed. The addition of this aspect to the current analysis assisted in capturing the shear and flexure pattern in a four point bending of a simply supported concrete beam.



Figure 1. Paddlefish from the lower Mississippi River showing the unique rostrum of the species. (Upper photo) Adult fish 1 m long contained in a mobile swim tunnel; (lower photo) dried and skeletonized rostrum. Photo taken by Dr. Jan Jeffrey Hoover, USACE.

The paper is organized as follows. In Section 2, a brief introduction to network flow is provided, and Section 3 describes the procedure to formulate the biostructure as a network flow problem. In Section 4, the proposed approach is verified using two classical problems. Details of the computational

mechanics experiments are discussed in Section 5, followed by results in Section 6, and conclusions follow in Section 7.

2. Network Flow

A brief introduction of the basic concepts of network flow is now provided. A flow network is a directed graph with two distinguished vertices, called a source and a sink, coupled with a non-negative real-valued function called the capacity function [27,41,42].

A network N is defined as a set comprising:

1. directed graph $G(V, E)$, where V is a finite set of vertices, and E is a subset of ordered pairs of vertices representing the edges;
2. vertex $s \in V$ that has only outgoing edges represented as the source node;
3. vertex $t \in V$ that has only incoming edges represented as the sink node; and
4. positive function $c: E \rightarrow R^+$ called the capacity function.

Flow f on a network N is defined by real-valued function $f: E \rightarrow R^+$. Flow f is a feasible flow vector if it satisfies the following constraints:

1. Capacity constraint $\forall u, v \in V$ requires that $f(u, v) \leq c(u, v)$; flow cannot exceed the capacity of the respective edge.
2. Conservation of flow $\forall u, v \in V - (s, t)$ requires that
 - (a) $\sum_{v \in V} f(u, v) = 0$,
 - (b) the total flow entering a node must equal the total flow leaving that node provided the node is not a source or sink node, and
3. the total flow leaving the source node s must be equal to the total flow entering sink node t .

Given a flow network $G(V, E)$, with source s and sink t , such that there are no incoming edges at the source and no outgoing edges at the sink, the maximum flow problem involves finding a function f that satisfies the capacity and conservation constraints described above; its value is defined as follows:

$$val(f) = max(f)$$

A cut of a flow network $G(V, E)$ is defined as a set of vertices (E_1, E_2) that partition V into E_1 and $E_2 = V - E_1$, such that $s \in E_1$ and $t \in E_2$. If f is a flow, then the net flow across the cut (E_1, E_2) is defined as $f(E_1, E_2)$. The capacity of the cut (E_1, E_2) is $c(E_1, E_2)$.

A minimum $E_1 - E_2$ cut problem involves minimizing $c(E_1, E_2)$. That would mean the identification of E_1 and E_2 in such a manner so as to find the minimal capacity of the (E_1, E_2) cut.

In combinatorial optimization theory, the maximum-flow/minimum-cut theorem states that in a flow network $G(V, E)$, the maximum quantity of flow f travelling from source node s to sink node t is identical to the total weight of the edges in the minimum cut. Essentially speaking, the maximum flow in the network is equal to the smallest total weight of the edges that, if removed, would cause the source to be totally disconnected from the sink.

The network flow approach has previously been applied to characterize stress transmission in various synthetic and natural materials with complex microstructures, for example, sand [29,43], photoelastic disks [29], and concrete [5]. In these studies, microstructural data on the internal connectivity and edge capacities were obtained from high-resolution imaging experiments (e.g., X-ray CT, birefringence analysis) and discrete-element (DEM) models.

3. Formulation of the Biostructure as Network Flow Problem

The flow of stress in a structural system can be interpreted as a directed graph that facilitates the investigation of failure mechanisms. Intuitively, the transmission of information at a given point in the

structural system is the rate at which the information (i.e., variables such as stress, displacement, kinetic energy, elastic or plastic strain in the structural system) travels. Each edge in a directed graph can be compared to a channel through which information is transmitted. Each edge has a corresponding capacity that is representative of the maximum rate at which information can be passed through the edge. Vertices of the graph are the points where the edges connect. Two special nodes identified as source and sink govern the flow. The edges connected to these special nodes are assigned infinite capacity [27,29]. The selection of these special nodes is dependent on the type of boundary conditions implemented on the model. For example, if the model is subjected to constant uniform pressure in the vertical direction, the nodes on the top or bottom surface of the model are chosen to act as the source and sink, respectively. Since the flow of stress is symmetric, altering the assignment of source and sink does not change the flow pattern.

A flow network $N(V, E, A, U, s, t)$ [27,29] is constructed from the computational-mechanics model, such that:

1. V represents the nodes obtained from the finite element model of the biostructure. As shown in Figure 2a, for a hexahedral element in a finite element model, nodes are 1, 2, . . . , 8.
2. E represents the edges, connecting the nodes in V , indicating connectivity A between the nodes. The edges of a hexahedral element, as shown in Figure 2a, are $\{(1, 2), (2, 3), (3, 4), (4, 1)\}$ for Face 1.
3. Each edge $(u, v) \in E$ has a capacity U associated with it that is representative of the maximum amount of flow that could be transmitted through the edge. Capacity calculation for Edge (1, 2) is shown in Figure 2c. Capacity for Edge (1, 2) is the average of the von Mises stresses at Nodes 1 and 2.
4. Von Mises stresses (as shown in Figure 3) at each node are calculated using the average of the integration points shown in Figure 2d.

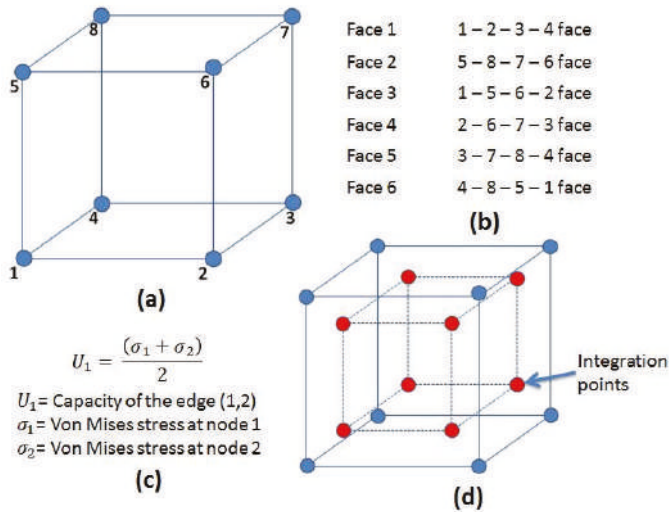


Figure 2. (a) Node numbering in an eight-node hexahedral element. (b) Hexahedral element faces in an eight-node hexahedral element. (c) Capacity calculation for edges in flow network graph. (d) Integration points on an eight-node hexahedral.

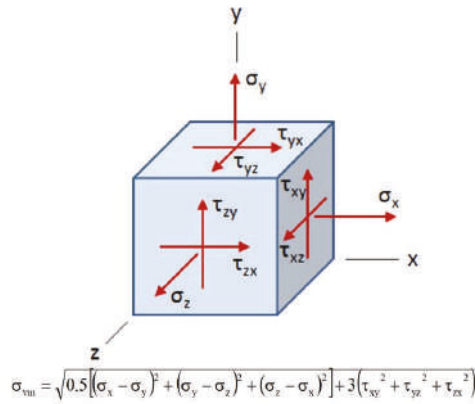


Figure 3. Von Mises stress equation expressed by the six stress components.

Each time frame from the computational-mechanics experiment is constructed as a network flow graph, where each graph depicts the flow of the variable of interest in response to the external loading condition. For each network, the maximum flow and minimum cut is calculated. As stated by the maximum-flow/minimum-cut theorem, the value of the maximum flow is equal to the capacity of the minimum cut.

The procedure outlined above for the proposed flow network approach is outlined in the flowchart shown in Figure 4. As shown in Figure 4, the flow network is constructed using the nodes and connectivity information from the computational mechanics experiment. Capacity C of the flow network was obtained from the Von Mises stresses produced from the binary output database files of the computational-mechanics experiment. The mathematical algorithm was executed on the abstract domain. The solution obtained from the mathematical algorithm was mapped back to the physical domain using the coordinate information of the nodes. Paraview was used for visualizing the solution of the mathematical algorithm. As mentioned above, the procedure of formulating the solution from finite element analysis as a flow network graph was carried out in four stages. As shown in Figure 4, in Stage 1, the flow network was constructed using the nodes and connectivity information from finite element analysis. In Stage 2, the weight of the flow network was obtained using the parameter of interest (stresses, in the current study, were also acquired from finite element analysis). In Stage 3, the flow network graph was created. In Stage 4, the flow network graph was provided as input to the mathematical algorithm that computes the minimum cut of the flow network graph. The details of the procedure involved in the four stages mentioned above is described in the previous work of Patel et al. [40].

The flow network graph in the current study was developed using data obtained from finite element simulation. The Abaqus/Standard solver was used for conducting static analysis. The choice of Abaqus/Standard for performing these analyses is justified based on the algorithm that it employs for static and low-speed dynamic events, where highly accurate stress solutions are required. Analysis was executed in two steps. Gravity load (self-weight) is applied to the models in the initialization stage. Pressure load was applied to the models in the second stage. The pressure load applied to the model was obtained by multiplying the total load with the time increment of the finite element simulation. Geometric nonlinearity was taken into account in the simulations.

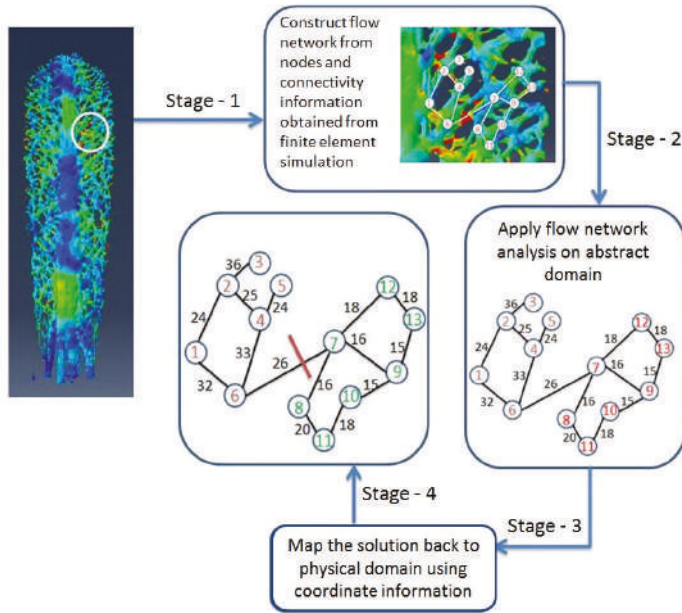


Figure 4. Flowchart depicting the steps involved in formulating a small part of rostrum as a network flow problem.

4. Verification of Approach on Known Datasets

The customary method for verifying a new approach is to use a problem that is simple enough to have an analytical solution and similar enough to the phenomena that are being simulated so that a meaningful extrapolation to the actual problem is feasible. By doing so, numerical and analytical solutions can be compared, and the fundamental shortcomings of the numerical approach used to solve the problem can be identified. To verify the current research methodology, two simple problems were chosen. The problem descriptions and methodology implementations follow in the subsections below.

4.1. Problem 1: Three-Point Bending of a Simply Supported Beam

The Abaqus/Standard solver [44] was used to carry out a computational-mechanics experiment on a simply supported concrete beam. The length of the beam was 216 inches, the width was 36 inches, and the thickness was 6 inches. A mass density of 8.67×10^{-11} slug/in³, Young’s modulus of 3×10^6 psi, and Poisson’s ratio of 0.3 were used for the concrete material model [45,46]. The Abaqus mesh consisted of 73,278 quadratic tetrahedral elements comprising 117,709 nodes. The schematic of the loading condition on the simply supported concrete beam is displayed in Figure 5.

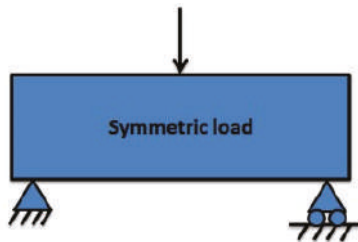


Figure 5. Schematics of three-point bending of a simply supported concrete beam.

The maximum principal stresses obtained from the computational-mechanics experiment are plotted in Figure 6, which gives the overall stress distribution in the beam subjected to a concentrated load of 100 MPa at the center. The simulation was carried out using the dynamic, explicit method in Abaqus for a total time of 0.005 s. Geometric nonlinearity effects were included. The node and connectivity information were extracted from the computational mechanics model to construct a flow network. The network was weighted based on the Von Mises stress values from the Abaqus output database file. The von Mises stresses are equivalent tensile stresses derived from the stress deviator [47].

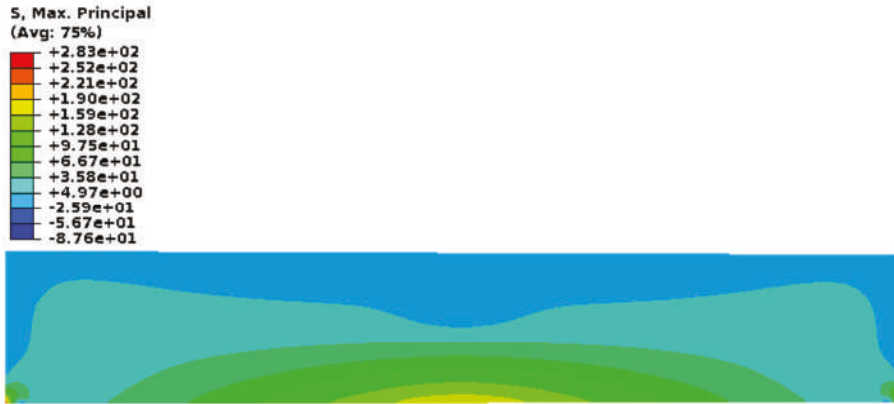


Figure 6. Maximum principal stresses for three-point bending of a simply supported concrete beam.

Source and sink combinations were selected from high-stress areas. The result of the network flow analysis is shown in Figure 7. The source in this case was chosen in the area where the load was applied. The sink was selected in the area where maximum deformation occurs for this classical problem (i.e., the midpoint of the beam parallel to where the source was selected). Figure 7 shows the result of network flow analysis. The minimum cut identified by the mathematical algorithm is represented by the blue line in Figure 7. The minimum cut denotes a set of edges in the flow network that inhibit flow transmission or form transmission bottlenecks, i.e., flow network analysis highlights the members of the beam where the failure mechanism initiates. For this problem, network analysis shows the typical behavior of a beam subjected to a concentrated load at the center line. A failure for this classical problem initiates with a crack at the bottom face sheet at the beams midspan and continues to grow as the load increases. Hence, the proposed methodology for detecting the failure mechanisms at the nascent stage of loading from the computational-mechanics experiment and flow network approach was verified using a simple problem with a known solution.

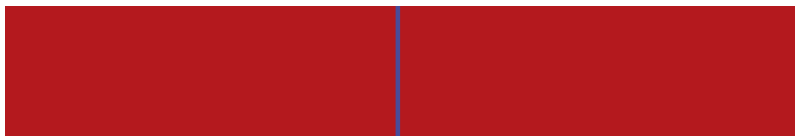


Figure 7. Flow network analysis for three-point bending of a simply supported concrete beam.

4.2. Problem 2: Four-Point Bending of a Simply Supported Beam

The dimensions and material of the model used for Problem 2 are identical to the concrete beam used in Problem 1. For this problem, the concrete beam was a simply supported beam with two equal forces applied equidistant from the supports, as shown in Figure 8 [45,46].

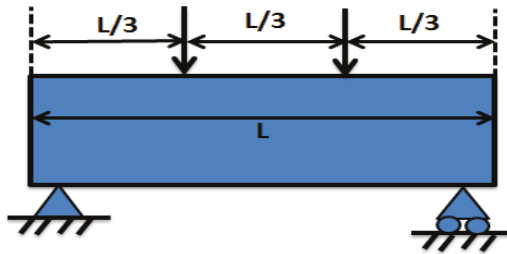


Figure 8. Schematics of four-point bending of a simply supported concrete beam.

The maximum-flow/minimum-cut algorithm was executed in seven scenarios. The source node in each scenario was chosen to be a vertex where the force is applied while the sink node in each scenario was chosen to be a point in an area where a stress transition was visually identified. The sink nodes were selected by looking at the maximum principal stresses, shown in Figure 9. Seven sink nodes were selected. The mathematical algorithm was executed seven times using this source–sink combination. The results were superimposed as the material is in the linear elastic regime.

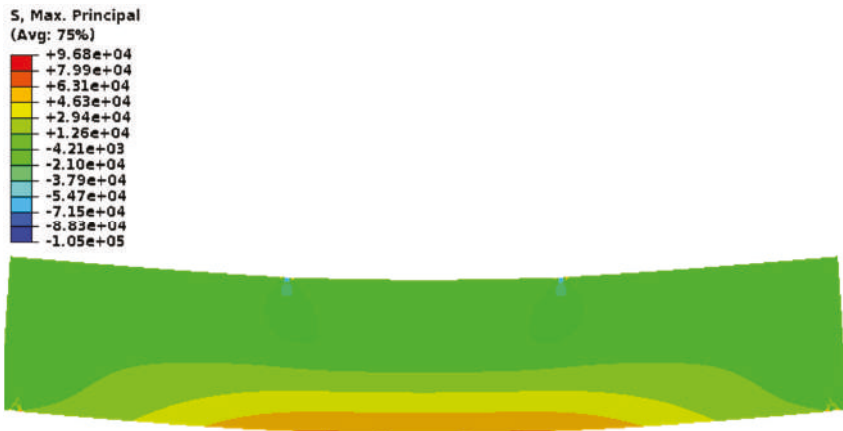


Figure 9. Maximum principal stresses for four-point bending of a simply supported concrete beam.

Figure 10 shows the superimposed result obtained by running the maximum-flow/minimum-cut algorithm. The minimum cut clearly identified the shear patterns on the left and right corners, and flexure patterns in the center are highlighted by the white lines in Figure 10. These shear and flexure patterns govern the phenomena of the failure mechanism in this classical problem. The network flow strategy identified these patterns at the onset of loading when the material was still in the linear elastic regime.



Figure 10. Flow network analysis of four-point bending of a simply supported concrete beam.

5. Computational Mechanics Experiments on the Rostrum

Computational mechanics experiments were carried out on the rostrum of the paddlefish. Simulations were performed in the U.S. Army Engineer Research and Development Centers High Performance Computing facilities located in Vicksburg, MS. The computational model was generated from the tomography (CT scan) of the paddlefish rostrum. The grey tones of the scanned image of the rostrum helped identify the three parts of the rostrum (tissue, hard cartilage, and soft cartilage). Figure 11 shows the tissue component of the rostrum. The tissue is the outermost layer of the rostrum that encompasses the hard cartilage, shown in Figure 11. The soft cartilage is located in the central portion of the rostrum. The mesh assembly cross-section shows the location of the three components of the rostrum in the actual model. The component parts of the rostrum were individually imported into commercial software Abaqus. The parts were meshed using a combination of hexahedral and tetrahedral elements. The model used in the current research comprises 119,712 hexahedral elements, 1,300,451 tetrahedral elements, 375,361 nodes, and 1,126,083 total degrees of freedom.

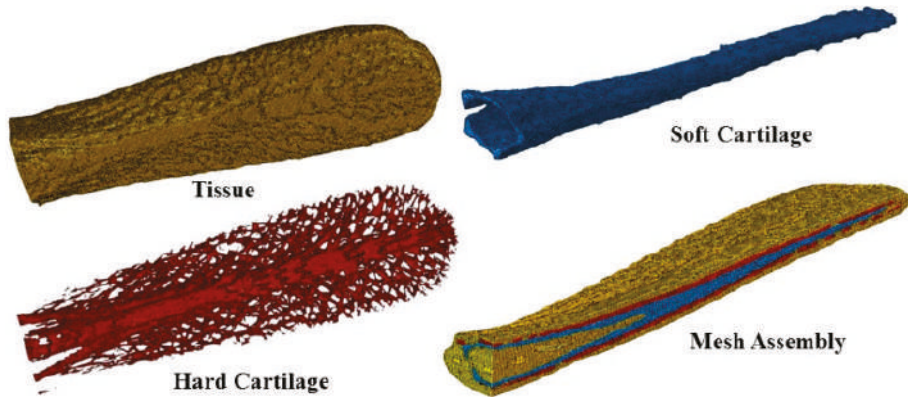


Figure 11. Abaqus mesh model of the rostrum. Dorsal view of tissue and hard cartilage on the left, lateral view of soft cartilage and oblique lateral sagittal section of mesh assembly on the right.

5.1. Material Properties

Nano-indentation experiments carried out on the rostrum revealed the material properties of the components of the rostrum [48]. The three parts of the rostrum, as shown in Figure 11, have considerably different material properties [49]. Taking this into consideration, a similar variation in material properties was maintained when selecting the materials for finite element analysis. Table 1 shows the three commercially available materials selected to represent the rostrum components shown in Figure 11.

Table 1. Commercial materials selected to model the rostrum.

Part	Commercial Material	Elastic Modulus
Tissue	Vinyl ester epoxy	2.9 GPa
Hard cartilage	Polyethylene fibers	66 GPa
Soft cartilage	Polyethylene/epoxy(as isotropic)	49,762 MPa

5.2. Force and Displacement Boundary Conditions

A uniform pressure was applied on the top surface of the rostrum, displayed in purple shading in Figure 12. A fixed-plate boundary condition was implemented on the rostrum by restraining the three components of displacement. A uniform pressure of 50 MPa was applied in the loading direction,

shown in Figure 12. Pressure was applied perpendicular to each element face on the top surface of the rostrum, displayed in purple shading in Figure 12, thereby following the surface contour.

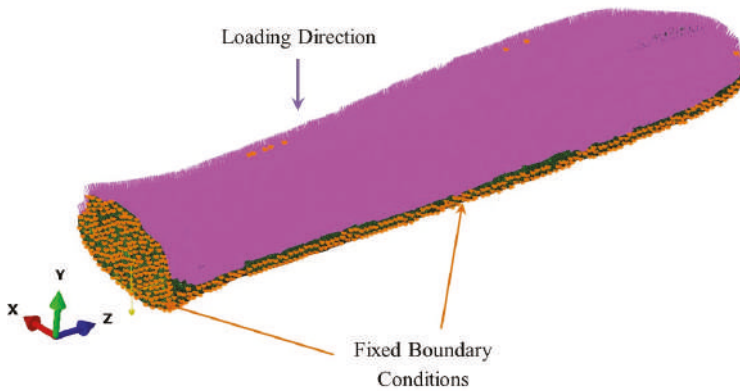


Figure 12. Force and displacement boundary conditions implemented on the rostrum.

6. Results

Although computational-mechanics experiments provide the overall distribution of stresses in the structural system, information about stress-flow patterns formed at nascent stages of loading is missing. Identification of the stress-flow patterns in the linear elastic regime may lead to novel insight into failure mechanisms through identification of the location of stress concentration areas developed due to change in geometry and material properties. To obtain these stress patterns, the rostrum is formulated as a network flow model by utilizing node and connectivity information from the computational-mechanics model. The network is weighted based on the Von Mises stresses obtained from the output database file produced from the computational-mechanics experiments on the rostrum. The maximum-flow/minimum-cut algorithm described in Reference [39] was used to identify the stress-flow patterns when the rostrum is subjected to a uniform pressure load. A seamless, platform-independent interface was developed to formulate the rostrum as a network flow problem and compute the maximum flow/minimum cut of the network.

Source and sink nodes were identified and provided as input to the maximum-flow/minimum-cut algorithm. For the rostrum, these nodes were selected based on the displacement contours shown in Figure 13. The source and sink nodes were identified at the edges and center of the maximum displacement area on the top and bottom surfaces of the rostrum, represented by red coloring in Figure 13. As verified earlier in Problem 2, the mathematical algorithm was executed three times using the source/sink combination shown in Figure 13. The results were superimposed, as the material was in the linear elastic regime. Reversing the selection of source and sink nodes on the top and bottom surfaces does not change the result obtained using the maximum-flow/minimum-cut algorithm.

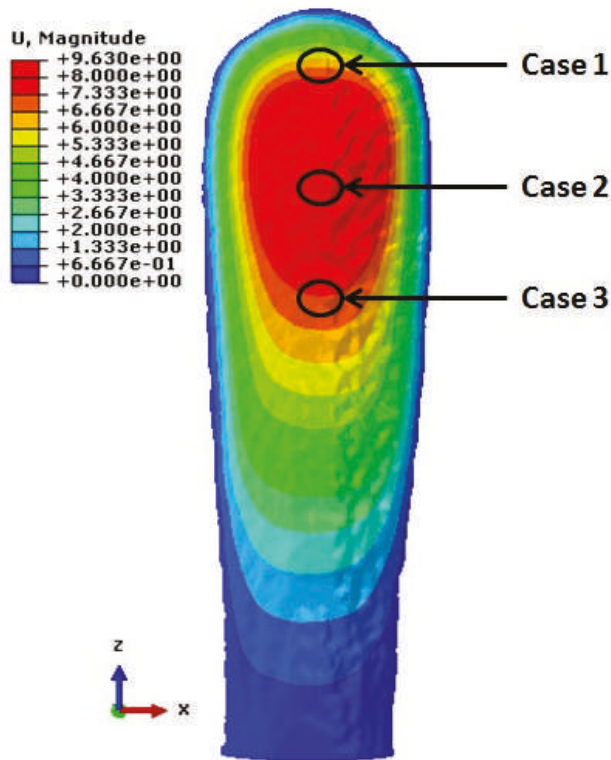


Figure 13. Displacement contours of the rostrum subjected to uniform pressure loading with a fixed plate boundary condition showing the location of source/sink. Cases 1 and 3 were chosen at the edges, and Case 2 in the center of the maximum displacement contour. Dorsal view of rostrum.

6.1. Flow Network Analysis on Soft Cartilage of the Rostrum

Figure 14a shows the maximum principal stresses on the bottom surface of the soft-cartilage part of the rostrum. Although stresses progressively increased in the early stages of loading, they were evenly distributed across the entire bottom surface, thereby providing no insight into the phenomena of the failure mechanism. In contrast, Figure 14b displays the output obtained by executing the maximum-flow/minimum-cut algorithm using the source/sink combination, shown earlier in Figure 9, and superimposing the results as validated in Problem 2. The minimum cut embodies a set of vertices that inhibit the transmission of information, i.e., stresses in the current analysis. The minimum cut on the bottom surface of the soft cartilage is along the edges where there is a change in material properties. The failure initiates at this position owing to change in geometry and material properties. The red regions at the tip and base of the bottom surface are also located at the areas where material properties change. The maximum-flow/minimum-cut algorithm detected the failure sites at nascent stages of loading.

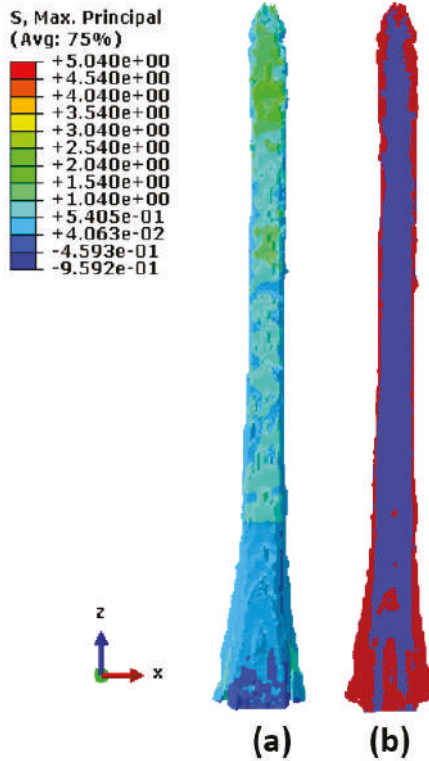


Figure 14. Soft cartilage of paddlefish rostrum. (a) Maximum principal stress obtained from finite element analysis. (b) Minimum cut obtained from mathematical analysis on bottom surface of rostrum’s soft cartilage. Nodes are colored by their respective locations on the source (red) or sink (blue) side of the minimum cut.

Figure 15a shows the maximum principal stresses on the top surface of the soft-cartilage part of the rostrum. As observed earlier in Figure 14a, finite element analysis shows stresses progressively increasing as the external load increases, as expected. On the other hand, Figure 15b shows the minimum cut obtained by running the maximum-flow/minimum-cut algorithm. The interface between the red and blue nodes is the location of the failure site. The failure for the top surface of the rostrum initiates along the edges where there is a change in the material properties. The red region at the base of the top surface falls in areas where there is contact between components with varying material properties. Hence, the flow network strategy successfully identified the local regions where failure mechanisms were expected to initiate.

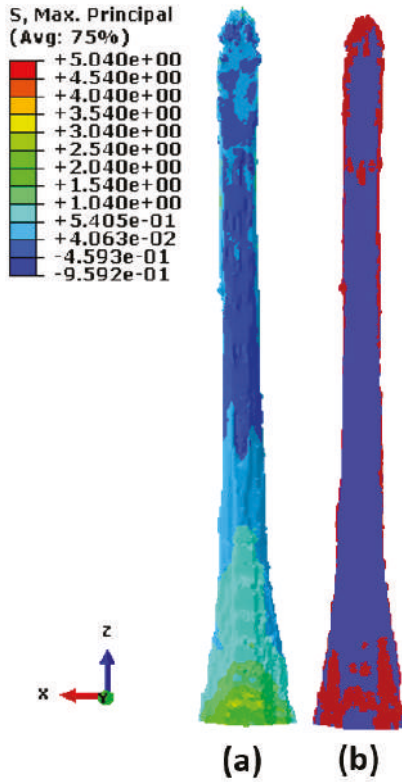


Figure 15. Soft cartilage of paddlefish rostrum. (a) Maximum principal stress obtained from finite element analysis. (b) Minimum cut obtained from mathematical analysis on top surface of rostrum’s soft cartilage. Nodes are colored by their respective locations on the source (red) or sink (blue) side of the minimum cut.

6.2. Flow Network Analysis on Hard Cartilage of Rostrum

Figure 16a shows the maximum principal stresses on the bottom surface of the hard-cartilage part of the rostrum. Overall stresses progressively increased with the increase in external loading, as expected. Figure 16b displays the minimum cut obtained from the maximum-flow/minimum-cut algorithm. Nodes are colored by their respective locations on the source (red) or sink (blue) side of the minimum cut. The failure sites are located in the interface between the red and blue nodes. As seen in Figure 16b, these regions are located in the center part of the hard cartilage. Since the lattice region of the hard cartilage is not a continuous pattern, failure does not travel through the lattice region. The minimum cut picks up a region in the lattice where stress concentration is high and nodes are prone to failure. The center part of Figure 16b clearly displays strain localization, which is a typical mode of failure of a structural system under tensile loading. Hence, the research strategy implemented in the current work successfully identified the failure mechanisms at the nascent stages of loading.

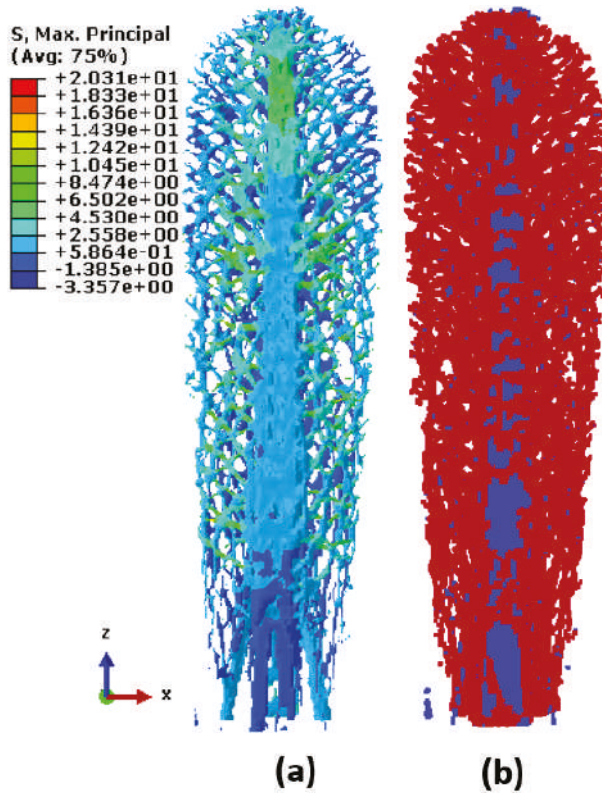


Figure 16. Hard cartilage of paddlefish rostrum. (a) Maximum principal stress obtained from finite element analysis. (b) Minimum cut obtained from mathematical analysis on bottom surface of rostrum's hard cartilage. Nodes are colored by their respective locations on the source (red) or sink (blue) side of the minimum cut.

Figure 17a displays the maximum principal stresses on the top surface of the hard-cartilage part of the rostrum. Although finite element analysis gives the overall distribution of stresses in the structural system, the underlying details that govern the phenomena of failure mechanism are hard to determine from the stresses. Figure 17b, on the contrary, shows the minimum cut obtained by executing the maximum-flow/minimum-cut algorithm. The central part of Figure 17b clearly highlights the crushing/buckling behavior that is typically seen in compressive failure. A major part of the failure sites in this case were also located in the region where there was a change in geometry and material properties, which is a typical region where failure initiates. Again, the current methodology successfully identified the sites of failure at the nascent stages of loading.

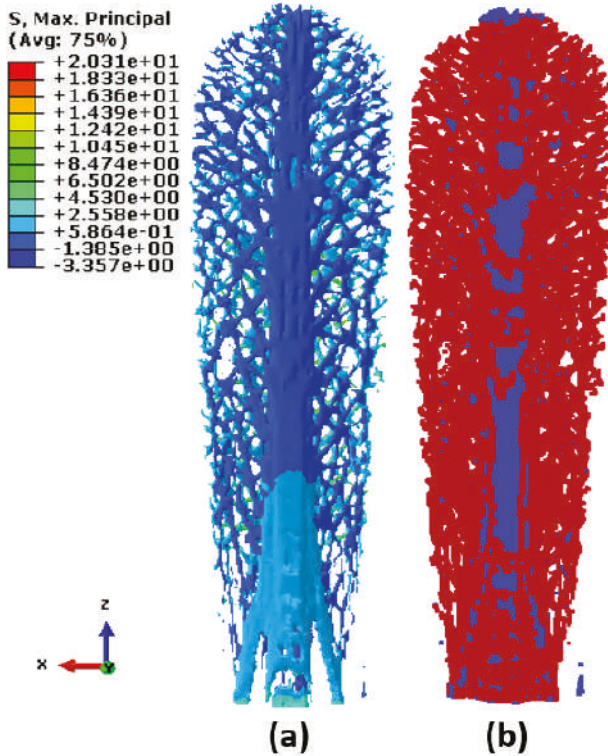


Figure 17. Hard cartilage of paddlefish rostrum. (a) Maximum principal stress obtained from finite element analysis. (b) Minimum cut obtained from mathematical analysis on top surface of rostrum's hard cartilage. Nodes are colored by their respective locations on the source (red) or sink (blue) side of the minimum cut.

6.3. Flow Network Analysis on Rostrum Tissue

Figure 18a shows the minimum cut obtained from flow network analysis on the bottom surface of the rostrum using the source–sink combination shown Figure 9. As seen in Figure 18a, the flow network captured the failure patterns at much earlier stages of loading that were not evident in the computational-mechanics results shown in Figure 18b. At low pressure levels, the strain localization patterns are captured on the tip of the central region of Figure 18a. As pressure increases, the strain-localization patterns are formed all along the central region of the rostrum tissue. Trusslike patterns are captured on the tissue part of the rostrum, as seen in Figure 18a. In contrast, the maximum principal stresses seen in Figure 18b did not show evidence of such patterns. The strain localization patterns captured through the flow network strategy are typically observed in a structural system under tensile loading. At a pressure of 7.143 MPa, Figure 18a also does not show any failure sites at the base of the tissue part of the rostrum indicative of it being stronger than the remaining part of the rostrum. This is the region that is attached to the mouth of the paddlefish, and this particular structural system is optimized for performance in this area. The flow network strategy captured this pattern at nascent stages, when the material was still in the linearly elastic regime.

Figure 19a displays the minimum cut obtained by using the flow network approach on the top surface of the rostrum. As seen in Figure 19a, at lower stresses the minimum cut is clearly formed in the right and left side of the rostrum. This is the region where the material properties of this component of the rostrum drastically change. As pressure increases, patterns are formed in the center and base

region. As pressure increases in Figure 19a, there is also an absence of failure sites at the left and right corners of the base region of the rostrum. This behavior is similar to the one observed on the top surface of the rostrum. This is indicative of the identification of the stronger part of the rostrum at the nascent stage of loading.

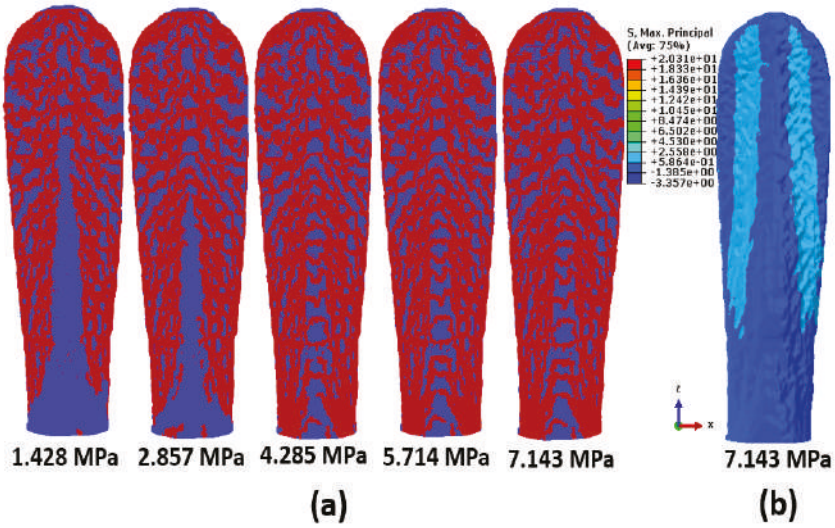


Figure 18. Tissue of paddlefish rostrum. (a) Network flow analysis on the bottom surface of rostrum subjected to uniform pressure loading with a fixed plate boundary condition. Nodes are colored by their respective locations on the source (red) or sink (blue) side of the minimum cut. (b) Maximum principal stresses on the bottom surface of rostrum.

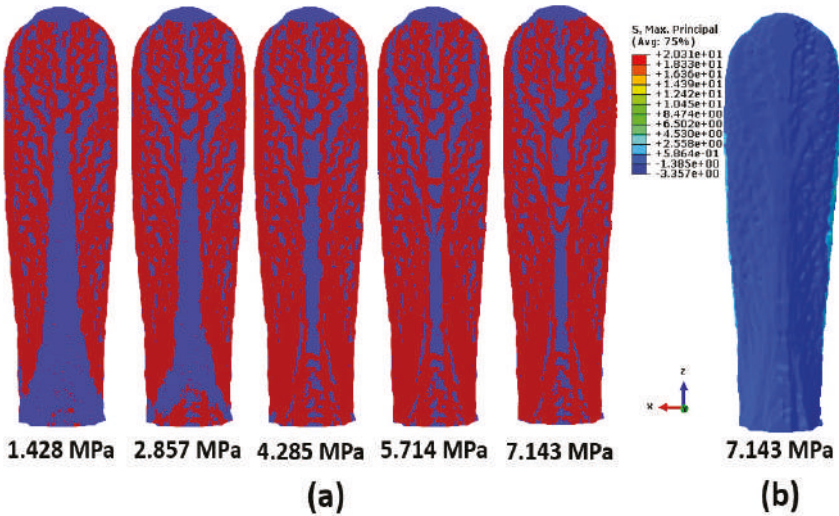


Figure 19. Tissue of paddlefish rostrum. (a) Network flow analysis on the top surface of the rostrum subjected to uniform pressure loading with a fixed plate boundary condition. Nodes are colored by their respective locations on the source (red) or sink (blue) side of the minimum cut. (b) Maximum principal stresses on the top surface of rostrum.

7. Conclusions

This work successfully used the maximum-flow/minimum-cut algorithm for early detection of failure mechanisms in the paddlefish rostrum under uniform pressure loading and a fixed plate boundary condition. The transdisciplinary approach proposed in the current study was verified using two classical problems before implementing it on the complex biostructure.

The flow network approach was able to identify failure for the problem involving the three-point bending of a simply supported concrete beam. The proposed approach was able to identify the shear and flexure patterns for four-point bending of a simply supported concrete beam. The shear and flexure patterns identified by the flow network approach govern the phenomena of the failure mechanism in this classical problem. Failure patterns were identified at the onset of loading when the material was still in the linear elastic regime.

When applied to a complex biostructure, the flow network strategy was able to identify the strain localization in the tensile region, and the crushing behavior in the compressive region of the rostrum. Additionally, the flow network approach was able to identify the failure sites at locations where the material properties as well as the geometry of the component parts of the rostrum change, i.e., at the interface regions. The interface regions are typically where the failure initiates. This information can be used to efficiently design smart structural systems. The guidance regarding the selection of the source and sink nodes was obtained from the stress and deformation contours obtained from the computational mechanics experiments.

8. Comments on the Transdisciplinary Approach

This work successfully identified the stress-flow patterns in a complex biostructure through efficient use of flow network strategy. The approach used in the current work reduces the computational time, and cost since it is not required to run finite element analysis to failure. Stress patterns were identified when the material was in the linearly elastic regime. This approach laid the foundation of an efficient design–test–build cycle for the rapid prototyping of bioinspired structures. The flow network approach reduces the size of the problem since we concentrate on the parameter of interest, i.e., stress in the current study.

Author Contributions: Investigation, R.P.; resources, A.T.; supervision, G.R.; writing—review and editing, G.R., D.T., E.P., J.J.H., and J.P.

Acknowledgments: The authors acknowledge the financial support provided by U.S. Army Engineer Research and Development Center (ERDC) under PE 0601102, Project T22 “Research in Soil and Rock Mechanics”, Task 01. The support and resources from the Engineer Research and Development Center Department of Defense Supercomputing Resource Center (ERDC DSRC) under the subproject Environmental Quality Modeling and Simulation are gratefully acknowledged. Permission was granted by the Director of the Information Technology Laboratory to publish this information.

Conflicts of Interest: The authors declare no conflict of interest.

References

1. Aggelis, D.G. Classification of cracking mode in concrete by acoustic emission parameters. *Mech. Res. Commun.* **2011**, *38*, 153–157. [[CrossRef](#)]
2. Carpinteri, A.; Lacidogna, G.; Niccolini, G.; Puzzi, S. Critical defect size distributions in concrete structures detected by the acoustic emission technique. *Meccanica* **2008**, *43*, 349–363. [[CrossRef](#)]
3. Farhidzadeh, A.; Salamone, S.; Singla, P. A probabilistic approach for damage identification and crack classification in reinforced concrete structures. *J. Intell. Mater. Syst. Struct.* **2013**, *24*, 1722–1735. [[CrossRef](#)]
4. Farhidzadeh, A.; Mpalaskas, A.C.; Matikas, T.E.; Farhidzadeh, H.; Aggelis, D.G. Fracture mode identification in cementitious materials using supervised pattern recognition of acoustic emission features. *Constr. Build. Mater.* **2014**, *67*, 129–138. [[CrossRef](#)]

5. Kageyama, K.; Murayama, H.; Ohsawa, I.; Kanai, M.; Nagata, K.; Machijima, Y. Acoustic emission monitoring of a reinforced concrete structure by applying new fiber-optic sensors. *Smart Mater. Struct.* **2005**, *14*, s52–s59. [[CrossRef](#)]
6. Ohtsu, M.; Uchida, M.; Okamoto, T.; Yuyama, S. Damage assessment of reinforced concrete beams qualified by acoustic emission. *ACI Struct. J.* **2002**, *99*, 411–417.
7. Shiotani, T.; Aggelis, D.G.; Makishima, O. Global monitoring of large concrete structures using acoustic emission and ultrasonic techniques: Case study. *J. Bridge Eng.* **2009**, *14*, 188–192. [[CrossRef](#)]
8. Bahlouli, N.; Guil, S.M.; Ahzi, S.; Laberge, M. Stress-strain response of biomaterials by a digital image correlation method: Application to tecoflex. *J. Mater. Sci. Technol.* **2004**, *20*, 114–116.
9. Carroll, J.; Efstathiou, C.; Lambros, J.; Sehitoglu, H.; Hauber, B.; Spottswood, S.; Chona, R. Investigation of fatigue crack closure using multiscale image correlation experiments. *Eng. Fract. Mech.* **2009**, *76*, 2384–2398. [[CrossRef](#)]
10. Fazzini, M.; Mistou, S.; Karama, M. Identification of elastomers by digital image correlation. In Proceedings of the 5th European Conference on Constitutive Models for Rubber, Paris, France, 4–7 September 2007.
11. Goh, C.P.; Ratnam, M.M.; Ismail, H. Large in-plane deformation mapping and determination of young’s modulus of rubber using scanner-based digital image correlation. *Exp. Tech.* **2015**, *40*, 1117–1127. [[CrossRef](#)]
12. González, G.L.; González, J.A.; Castro, J.T.; Freire, J.L. A J-integral approach using digital image correlation for evaluating stress intensity factors in fatigue cracks with closure effects. *Theor. Appl. Fract. Mech.* **2017**, *90*, 14–21. [[CrossRef](#)]
13. Lopez-Crespo, P.; Shterenlikht, A.; Yates, J.; Patterson, E.; Withers, P. Some experimental observations on crack closure and crack-tip plasticity. *Fatigue Fract. Eng. Mater. Struct.* **2009**, *32*, 418–429. [[CrossRef](#)]
14. Mudassar, A.A.; Butt, S. Improved digital image correlation method. *Opt. Lasers Eng.* **2016**, *87*, 156–167. [[CrossRef](#)]
15. Sutton, M.A.; McNeill, S.R.; Helm, J.D.; Chao, Y.J. Advances in Two-Dimensional and Three Dimensional Computer Vision. In *Photomechanics*; Springer: Berlin/Heidelberg, Germany, 2000; pp. 323–372.
16. Sutton, M.A.; Orteu, J.J.; Schreier, H. *Image Correlation for Shape, Motion and Deformation Measurements: Basic Concepts, Theory and Applications*; Springer Science and Business Media: New York, NY, USA, 2009.
17. Vasco-Olmo, J.; Díaz, F.; García-Collado, A.; Dorado-Vicente, R. Experimental evaluation of crack shielding during fatigue crack growth using digital image correlation. *Fatigue Fract. Eng. Mater. Struct.* **2015**, *38*, 223–237. [[CrossRef](#)]
18. Hallgren, M.; Bjerke, M. Non-linear finite element analyses of punching shear failure of column footings. *Cem. Concr. Compos.* **2002**, *24*, 491. [[CrossRef](#)]
19. Mamede, N.F.; Ramos, A.P.; Faria, D.M. Experimental and parametric 3D nonlinear finite element analysis on punching of flat slabs with orthogonal reinforcement. *Eng. Struct.* **2013**, *48*, 442–457. [[CrossRef](#)]
20. Shu, J.; Plos, M.; Zandi, K.; Johansson, M.; Nilenius, F. Prediction of punching behavior of RC slabs using continuum non-linear FE analysis. *Eng. Struct.* **2016**, *15*, 15–25. [[CrossRef](#)]
21. Borderie, C.L.; Lawrence, C.; Menou, A. Approche mésoscopique du comportement du béton: Apport de la représentation géométrique. *Revue Européenne de Génie Civil* **2007**, *11*, 407–421. [[CrossRef](#)]
22. Grassl, P.; Grégoire, D.; Rojas-Solano, L.B.; Pijaudier-Cabot, G. Meso-scale modelling of the size effect on the fracture process zone of concrete. *Int. J. Solids Struct.* **2012**, *49*, 1818–1827. [[CrossRef](#)]
23. Grégoire, D.; Verdon, L.B.; Lefort, V.; Grassl, P.; Saliba, J.; Regoin, J.P.; Loukili, A.; Pijaudier-Cabot, G. Mesoscale analysis of failure in quasi-brittle materials: Comparison between lattice model and acoustic emission data. *Int. J. Numer. Anal. Methods Geomech.* **2015**, *39*, 1639–6164. [[CrossRef](#)]
24. Flores-Johnson, E.; Shen, L.; Guimatsia, I.; Nguyen, G.D. A numerical study of bioinspired nacre-like composite plates under blast loading. *Compos. Struct.* **2015**, *126*, 329–336. [[CrossRef](#)]
25. Flores-Johnson, E.; Shen, L.; Guimatsia, I.; Nguyen, G.D. Numerical investigation of the impact behavior of bioinspired nacre-like aluminum composite plates. *Compos. Sci. Technol.* **2014**, *96*, 13–22. [[CrossRef](#)]
26. Tran, P.; Ngo, T.D.; Mendis, P. Bioinspired composite structures subjected to under water impulsive loading. *Comput. Mater. Sci.* **2014**, *82*, 134–139. [[CrossRef](#)]
27. Bertsekas, D.P. *Network Optimization: Continuous and Discrete Models (Optimization, Computation, and Control)*; Athena Scientific: Nashua, NH, USA, 1998.
28. Lin, Q.; Tordesillas, A. Towards an optimization theory for deforming dense granular materials: Minimum cost maximum flow solutions. *J. Ind. Manag. Optim.* **2014**, *10*, 337. [[CrossRef](#)]

29. Tordesillas, A.; Tobin, S.T.; Cil, M.; Alshibli, K.; Behringer, R.P. Network flow model of force transmission in unbonded and bonded granular media. *Phys. Rev. E* **2015**, *91*, 062204. [CrossRef]
30. Lefort, V.; Pijaudier-Cabot, G.; Grégoire, D. Analysis by Ripley's function of the correlations involved during failure in quasi-brittle materials: Experimental and numerical investigations at the mesoscale. *Eng. Fract. Mech.* **2015**, *147*, 449–467. [CrossRef]
31. Ripley, B.D. Modelling spatial patterns. *J. R. Stat. Soc. Ser. B Methodol.* **1977**, *39*, 172–212. [CrossRef]
32. Duncan, R.P. Flood disturbance and the coexistence of species in a lowland podocarp forest, south Westland, New Zealand. *J. Ecol.* **1993**, *81*, 403–416. [CrossRef]
33. Stamp, N.E.; Lucas, J.R. Spatial Patterns and Dispersal Distances of Explosively Dispersing Plants in Florida Sandhill Vegetation. *J. Ecol.* **1990**, *78*, 589–600. [CrossRef]
34. Diggle, P.J.; Chetwynd, A.G. Second-Order Analysis of Spatial Clustering for Inhomogeneous Populations. *Biometrics* **1991**, *47*, 1155–1163. [CrossRef]
35. Weiner, S.; Wagner, H.D. The material bone: Structure-Mechanical Function Relation. *Annu. Rev. Mater. Sci.* **1998**, *28*, 271–298. [CrossRef]
36. Hoover, J.J.; George, S.G.; Killgore, K.J. Rostrum size of paddlefish (*Polyodon spathula*) (*Acipenseiformes: Polyodontidae*) from the Mississippi Delta. *Copeia* **2000**, *1*, 288–290. [CrossRef]
37. Kuhajda, B.R. *Polyodontidae: Paddlefishes*; Johns Hopkins University Press: Baltimore, MD, USA, 2014.
38. Riveros, G.A.; Patel, R.R.; Hoover, J.J. Swimming and Energy Dissipation Enhancement Induced by the Rostrum of the Paddlefish (*Polyodon spathula*): A Multiphysics, Fluid-Structure Interaction Analysis. In Proceedings of the Materials Research Society Fall Meeting, Boston, MA, USA, 29 November–4 December 2015.
39. Patel, R.R.; Riveros, G.A.; Thompson, D.S.; Acosta, F.J.; Perkins, E.J.; Hoover, J.J.; Peters, J.F.; Tordesillas, A. *Early Detection of Failure Mechanisms in Resilient Biostructures: A Network Flow Study*; ERDC: Vicksburg, MS, USA, 2017.
40. Patel, R.R.; Valles, D.; Riveros, G.A.; Thompson, D.S.; Perkins, E.J.; Hoover, J.J.; Peters, J.F.; Tordesillas, A. Stress flow analysis of biostructures using the finite element method and the flow network approach. *Finite Elem. Anal. Des.* **2018**, *152*, 46–54. [CrossRef]
41. Bondy, J.A.; Murty, U.S.R. Graph Theory. In *Graduate Texts in Mathematics*; Springer: New York, NY, USA, 2008.
42. Jungnickel, D. Graphs, Networks and Algorithms. In *Algorithms and Computation in Mathematics* 5, 3rd ed.; Springer: Berlin, Germany, 2008.
43. Tordesillas, A.; Pucilowski, S.; Tobin, S.; Kuhn, M.R.; Ando, E.; Viggiani, G.; Druckrey, A.; Alshibli, K. Shear bands as bottlenecks in force transmission. *Eur. Phys. Lett.* **2015**, *110*, 58005. [CrossRef]
44. Dassault Systems. Abaqus 6.13 Using Abaqus Online Documentation. Available online: http://dsk.ippt.pan.pl/docs/abaqus/v6.13/pdf_books/HELP.pdf (accessed on 26 April 2019).
45. Riveros, G.A.; Gopalaratnam, V.S. Fracture response of reinforced concrete deep beams finite element investigation of strength and beam size. *Appl. Math.* **2013**, *4*, 1568. [CrossRef]
46. Riveros, G.A.; Gopalaratnam, V.S. *Shear Response of Reinforced Concrete Deep Beam: Validating Fracture Mechanics Based Numerical Modelling with Experiments*; American Concrete Institute: Farmington Hills, MI, USA, 2015.
47. Segalman, D.J.; Fulcher, C.W.G.; Reese, G.M.; Field, R.V., Jr. An Efficient Method for Calculating RMS von Mises Stress in a Random Vibration Environment. *J. Sound Vib.* **1998**, *230*, 393–410. [CrossRef]
48. Deang, J.; Horstemeyer, M.; Williams, L.; Perkins, E.; Allison, P.; Riveros, G. Paddlefish rostrum as a structure for bioinspiration: Analysis and modeling of the of the stress state and strain rate dependence behavior of cartilage. In Proceedings of the TMS Annual Meeting and Exhibition, Nashville, TN, USA, 14–18 February 2016.
49. Allison, P.G.; Deang, J.F.; Diaz, A.J.; Poda, A.R.; Hoover, J.J.; Horstemeyer, M.F.; Perkins, E.J. Characterization of paddlefish (*Polyodon spathula*) rostrum stellate bones. *Bioinspired Biomim. Nanobiomater.* **2013**, *3*, 63–68. [CrossRef]



© 2019 by the authors. Licensee MDPI, Basel, Switzerland. This article is an open access article distributed under the terms and conditions of the Creative Commons Attribution (CC BY) license (<http://creativecommons.org/licenses/by/4.0/>).

Article

Nonlocal FEM Formulation for Vibration Analysis of Nanowires on Elastic Matrix with Different Materials

Büşra Uzun¹ and Ömer Civalek^{2,*}

¹ Civil Engineering Department, Uludağ University, 16059 Bursa, Turkey; uzunbusra34@gmail.com

² Civil Engineering Department, Akdeniz University, 07070 Antalya, Turkey

* Correspondence: civalek@yahoo.com

Received: 12 February 2019; Accepted: 4 April 2019; Published: 6 April 2019

Abstract: In this study, free vibration behaviors of various embedded nanowires made of different materials are investigated by using Eringen's nonlocal elasticity theory. Silicon carbide nanowire (SiCNW), silver nanowire (AgNW), and gold nanowire (AuNW) are modeled as Euler–Bernoulli nanobeams with various boundary conditions such as simply supported (S-S), clamped simply supported (C-S), clamped–clamped (C-C), and clamped-free (C-F). The interactions between nanowires and medium are simulated by the Winkler elastic foundation model. The Galerkin weighted residual method is applied to the governing equations to gain stiffness and mass matrices. The results are given by tables and graphs. The effects of small-scale parameters, boundary conditions, and foundation parameters on frequencies are examined in detail. In addition, the influence of temperature change on the vibrational responses of the nanowires are also pursued as a case study.

Keywords: nonlocal elasticity theory; Galerkin weighted residual FEM; silicon carbide nanowire; silver nanowire; gold nanowire

1. Introduction

Nanoscale structures/materials have very different characteristics. Nanostructures/nanomaterials have attracted great attention because their extraordinary features, such as high strength, low density, high elasticity modulus, and high hardness [1–4], have become the focus of researchers. The aforementioned unique properties of such structures, materials, and rapid developments in nanotechnology has led to use of these structural elements in designing micro- and nanoelectro mechanical systems (MEMS and NEMS) such as resonators, atomic force microscopes, switches, actuators, and sensors.

Some experimental studies have revealed the deformation behaviors of micro-/nanosized structures [5,6]. However, experiments are very difficult and quite expensive on these scales because high precision test devices are needed. On the other hand, atomistic modeling such as molecular dynamic simulations is computationally expensive and requires a long period of time. Consequently, this option is limited to structures that have only a few atoms [7].

To understand and accurately interpret the mechanical properties and behaviors of nanoscale structures, use of models based on continuum mechanics may be a better alternative than experiments and atomistic modelling. Unfortunately, classical continuum theories are not sufficient to predict and estimate size dependency because they lack internal/additional material length scale parameters. In ultrasmall scales (micrometer dimension, nanometer dimension) interactions between atoms and molecules have increasing importance and cannot be neglected. Therefore, the solution to classical continuum theories, which does not take into account size effects, does not give accurate results. In order to obtain more accurate results, higher-order continuum theories such as couple stress theory [8–10], modified couple stress theory [11], strain gradient theory [12], modified strain gradient theory [13], and nonlocal elasticity theory [14] have been developed and contain various length scale

parameters. These theories were used by many researchers for various analyses such as buckling [15], bending [16,17], free vibration [18,19], forced vibration [20], and nonlinear vibration [21].

Rahmanian et al. [22] presented free vibrations of single-walled carbon nanotubes (SWCNT) on a Winkler elastic foundation via nonlocal elasticity theory. In this study, SWCNT was modeled as both beam and shell structures. Demir and Civalek [23] reported thermal vibration formulation of a nonlocal Euler–Bernoulli beam embedded in an elastic matrix. Finite element formulation for Eringen’s nonlocal elasticity theory was employed via Hermitian cubic shape functions. Thermal vibrational behaviors of silicon carbide nanowire on an elastic matrix were investigated for simply supported (S-S) and clamped–clamped (C-C) boundary conditions. Finite element formulations of nonlocal elastic Euler–Bernoulli and Timoshenko beam theories were achieved by Pradhan [24]. Vibration, buckling, and bending analyses of carbon nanotubes with four different boundary conditions were performed by the Galerkin finite element technique. Rajasekaran and Bakhshi Khaniki [25] reported static deformation, stability, and free vibration responses of small-scale beams. A finite element model of axial, functionally graded, nonuniform small-scale beams was investigated by using nonlocal strain gradient theory. Eltaher et al. [26] pursued free vibration analysis of functionally graded Euler–Bernoulli nanobeams by using Eringen’s nonlocal elasticity theory. Finite element results were given for a dynamic analysis of the nanobeam. Nejad and Hadi [27] studied bending analysis of non-homogeneous nanobeams. Eringen’s nonlocal elasticity theory was utilized in Euler–Bernoulli nanobeams made of bi-directional, functionally graded material. Murmu and Pradhan [28] studied the thermo-mechanical vibration response of embedded carbon nanotubes surrounded by an elastic matrix based on nonlocal elasticity theory. Reddy [29] developed nonlocal beam models based on four different beam theories. Static bending, free vibration, and buckling analyses of nanobeams are performed in this study. Tornabene et al. [30] presented a multiscale approach for three-phase carbon nanotube (CNT)/polymer/fiber-laminated nanocomposite structures. Detailed formulations can be found in the literature [31–35] about CNT-reinforcement or the finite element method (FEM). More recently, Uzun et al. [36] investigated the free vibration responses of carbon nanotubes and boron nitride nanotubes based on nonlocal elasticity theory. Nonlocal natural frequencies are obtained for various cross-section geometries.

In the present study, free vibration analysis of three kinds of nanowires resting on a Winkler elastic foundation with various boundary conditions are performed. Simply supported (S-S), clamped simply supported (C-S), clamped–clamped (C-C), and clamped-free (C-F) boundary conditions are selected. Silicon carbide nanowire (SiCNW), silver nanowire (AgNW), and gold nanowire (AuNW) are modeled as nonlocal Euler–Bernoulli beams, and their vibration behaviors are investigated using the finite element method (FEM). A Galerkin weighted residual method is utilized to govern equations and matrices, and the Winkler foundation parameter and small-scale parameter are gained. Effects of boundary conditions, temperature rise, and small-scale and Winkler foundation parameters of frequency values are investigated and compared for three kinds of nanowires.

2. Euler–Bernoulli Nanobeam Resting on a Winkler Elastic Foundation

The nonlocal stress tensor σ_{ij} at point x is expressed as follows [14]:

$$\sigma_{ij,j} = 0, \tag{1}$$

$$\sigma_{ij}(x) = \int_{\Omega} K(|x' - x|, \tau) C_{ijkl} \varepsilon_{kl} d\Omega(x'), \tag{2}$$

where $K(|x' - x|, \tau)$ is the Kernel function, $|x' - x|$ is the distance in the Euclidean form, $\tau = e_0 a / l$ is a material constant that depends upon the internal characteristic lengths (a) and external characteristic length (l), and e_0 is a material constant that is determined experimentally. C_{ijkl} and ε_{kl} represent the fourth-order elasticity and the strain tensors, respectively, and Ω is the region occupied by the body.

The nonlocal constitutive formulation is [28]:

$$[1 - \tau^2 l^2 \nabla^2] \sigma_{ij} = C_{ijkl} \varepsilon_{kl}. \tag{3}$$

x, y, z depict length, width, and height of the beam, respectively and u_1, u_2, u_3 are the displacements in the x, y, z directions. The displacements for a Bernoulli–Euler beam can be written as below [17]:

$$u_1(x, z, t) = -z \frac{\partial w(x, t)}{\partial x}, \quad u_2(x, z, t) = 0, \quad u_3(x, z, t) = w(x, t). \tag{4}$$

ε_{ij} is the strain tensor, expressed as:

$$\varepsilon_{ij} = 0.5(\partial u_{i,j} + \partial u_{j,i}). \tag{5}$$

From Equation (5) we find the strains of the Euler–Bernoulli beam as follows:

$$\varepsilon_{xx} = -z \frac{\partial^2 w(x, t)}{\partial x^2}, \quad \varepsilon_{xy} = \varepsilon_{yx} = \varepsilon_{xz} = \varepsilon_{zx} = \varepsilon_{yy} = \varepsilon_{yz} = \varepsilon_{zy} = \varepsilon_{zz} = 0. \tag{6}$$

Stress σ for the linear elastic materials is expressed as follows:

$$\sigma = E\varepsilon, \tag{7}$$

where E is the elastic modulus of the material. If ε_{xx} , the only nonzero component of strain, is written in Equation (7), σ_{xx} is obtained as:

$$\sigma_{xx} = -Ez \frac{\partial^2 w(x, t)}{\partial x^2}. \tag{8}$$

Moment (M) and the moment of inertia (I) are given by:

$$M = \int_A z \sigma_{xx} dA, \quad I = \int_A z^2 dA, \tag{9}$$

where A represents the cross-section area.

For the transverse vibration of an Euler–Bernoulli beam (shown in Figure 1) resting on a Winkler elastic foundation, the equilibrium conditions are:

$$\frac{\partial V(x, t)}{\partial x} = -q(x, t) + \rho A \frac{\partial^2 w(x, t)}{\partial x^2} + k_w w(x, t), \tag{10}$$

$$V(x, t) = \frac{\partial M(x, t)}{\partial x}, \tag{11}$$

$$\frac{\partial^2 M(x, t)}{\partial x^2} = -q(x, t) + \rho A \frac{\partial^2 w(x, t)}{\partial x^2} + k_w w(x, t), \tag{12}$$

where $\rho, q(x, t)$, and k_w are the mass density, distributed load, and Winkler foundation parameter, respectively.

The nonlocal constitutive relations can be simplified in the following form for a one-dimensional case [14,29]:

$$\sigma_{xx} - (e_0 a)^2 \frac{\partial^2 \sigma_{xx}}{\partial x^2} = E\varepsilon_{xx}. \tag{13}$$

By multiplying z on both sides of Equation (13) and integrating the cross-sectional area of the beam, we obtain:

$$\int_A z \sigma dA - (e_0 a)^2 \int_A z \frac{\partial^2 \sigma}{\partial x^2} dA = \int_A z E \varepsilon dA = 0. \tag{14}$$

Substituting Equations (6) and (9) into (14), we get:

$$M(x, t) - (e_0a)^2 \frac{\partial^2 M(x, t)}{\partial x^2} = -EI \frac{\partial^2 w(x, t)}{\partial x^2}. \tag{15}$$

By differentiating Equation (15) twice with respect to variable x and substituting Equation (12) into Equation (15), we obtain the governing equation for the vibration of an Euler–Bernoulli nanobeam resting on a Winkler elastic foundation, as below:

$$EI \frac{\partial^4 w(x, t)}{\partial x^4} + \rho A \frac{\partial w^2(x, t)}{\partial t^2} + k_w w - (e_0a)^2 \frac{\partial^2}{\partial x^2} \left[\rho A \frac{\partial^2 w(x, t)}{\partial t^2} + k_w w \right] = 0. \tag{16}$$

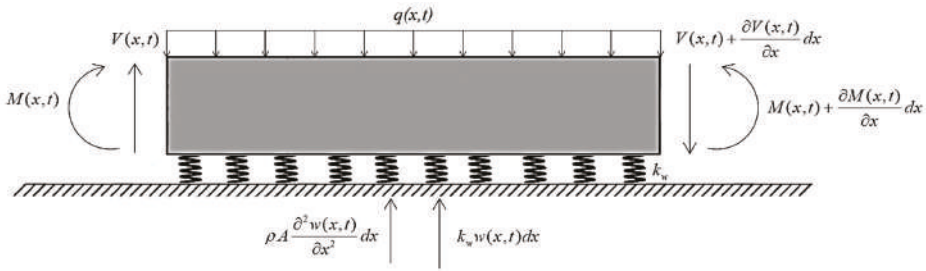


Figure 1. Euler–Bernoulli beam resting on a Winkler foundation.

3. Solution to the Vibration Problem

3.1. Galerkin Weighted Residual Method

The shape function for beam φ is as follows [37,38]:

$$\varphi = \begin{Bmatrix} \varphi_1 \\ \varphi_2 \\ \varphi_3 \\ \varphi_4 \end{Bmatrix} = \begin{Bmatrix} 1 - 3\xi^2 + 2\xi^3 \\ L(\xi - 2\xi^2 + \xi^3) \\ 3\xi^2 - 2\xi^3 \\ L(-\xi^2 + \xi^3) \end{Bmatrix}, \tag{17}$$

where $\xi = x/L$ is a non-dimensional local coordinate. In order to obtain the weak form of the governing equation of an Euler–Bernoulli nanobeam resting on a Winkler elastic foundation, the residue can be expressed as:

$$\left[EI \frac{\partial^4 w(x, t)}{\partial x^4} + \rho A \frac{\partial w^2(x, t)}{\partial t^2} + k_w w - (e_0a)^2 \frac{\partial^2}{\partial x^2} \left(\rho A \frac{\partial^2 w(x, t)}{\partial t^2} + k_w w \right) \right] = \text{residue}. \tag{18}$$

To determine the weighted residue, Equation (18) is multiplied by a weighting function φ . When the weighted residual is integrated over the length:

$$\int_0^L \left[\varphi EI \frac{\partial^4 w(x, t)}{\partial x^4} + \varphi \rho A \frac{\partial w^2(x, t)}{\partial t^2} + \varphi k_w w - \varphi (e_0a)^2 \frac{\partial^2}{\partial x^2} \left(\rho A \frac{\partial^2 w(x, t)}{\partial t^2} + k_w w \right) \right] dx = 0. \tag{19}$$

Equation (19) is integrated by parts. According to the chain rule, in the general form:

$$\int_0^L \left[EI \frac{\partial^2 \varphi}{\partial x^2} \frac{\partial^2 \varphi^T}{\partial x^2} + \rho A \varphi \varphi^T \ddot{w} + k_w \varphi \varphi^T w - (e_0a)^2 \rho A \frac{\partial \varphi}{\partial x} \frac{\partial \varphi^T}{\partial x} \ddot{w} - (e_0a)^2 k_w \frac{\partial \varphi}{\partial x} \frac{\partial \varphi^T}{\partial x} w \right] dx = 0. \tag{20}$$

By using the shape function in Equation (17) and the non-dimensional local coordinate, bending stiffness matrix K^b , Winkler foundation stiffness matrix K^w , and the mass matrix M , the following are obtained:

$$K^b = EI \int_0^L \begin{Bmatrix} \varphi_1'' \\ \varphi_2'' \\ \varphi_3'' \\ \varphi_4'' \end{Bmatrix} \begin{Bmatrix} \varphi_1'' & \varphi_2'' & \varphi_3'' & \varphi_4'' \end{Bmatrix} dx; \tag{21a}$$

$$K^b = \frac{EI}{L^3} \begin{bmatrix} 12 & 6L & -12 & 6L \\ 6L & 4L^2 & -6L & 2L^2 \\ -12 & -6L & 12 & -6L \\ 6L & 2L^2 & -6L & 4L^2 \end{bmatrix}; \tag{21b}$$

$$K^{w1} = k_w \int_0^L \begin{Bmatrix} \varphi_1 \\ \varphi_2 \\ \varphi_3 \\ \varphi_4 \end{Bmatrix} \begin{Bmatrix} \varphi_1 & \varphi_2 & \varphi_3 & \varphi_4 \end{Bmatrix} dx; \tag{22a}$$

$$K^{w1} = \frac{k_w}{420} \begin{bmatrix} 156L & 22L^2 & 54L & -13L^2 \\ 22L^2 & 4L^3 & 13L^2 & -3L^3 \\ 54L & 13L^2 & 156L & -22L^2 \\ -13L^2 & -3L^3 & -22L^2 & 4L^3 \end{bmatrix}; \tag{22b}$$

$$K^{w2} = (e_0a)^2 k_w \int_0^L \begin{Bmatrix} \varphi_1' \\ \varphi_2' \\ \varphi_3' \\ \varphi_4' \end{Bmatrix} \begin{Bmatrix} \varphi_1' & \varphi_2' & \varphi_3' & \varphi_4' \end{Bmatrix} dx; \tag{23a}$$

$$K^{w2} = \frac{(e_0a)^2 k_w}{30L} \begin{bmatrix} 36 & 3L & -36 & 3L \\ 3L & 4L^2 & -3L & -L^2 \\ -36 & -3L & 36 & -3L \\ 3L & -L^2 & -3L & 4L^2 \end{bmatrix}; \tag{23b}$$

$$M^1 = \rho A \int_0^L \begin{Bmatrix} \varphi_1 \\ \varphi_2 \\ \varphi_3 \\ \varphi_4 \end{Bmatrix} \begin{Bmatrix} \varphi_1 & \varphi_2 & \varphi_3 & \varphi_4 \end{Bmatrix} dx; \tag{24a}$$

$$M^1 = \frac{\rho A}{420} \begin{bmatrix} 156L & 22L & 54L & -13L^2 \\ 22L^2 & 4L^3 & 13L^2 & -3L^3 \\ 54L & 13L^2 & 156L & -22L^2 \\ -13L^2 & -3L^3 & -22L^2 & 4L^3 \end{bmatrix}; \tag{24b}$$

$$M^2 = (e_0a)^2 \rho A \int_0^L \begin{Bmatrix} \varphi_1' \\ \varphi_2' \\ \varphi_3' \\ \varphi_4' \end{Bmatrix} \begin{Bmatrix} \varphi_1' & \varphi_2' & \varphi_3' & \varphi_4' \end{Bmatrix} dx; \tag{25a}$$

$$M^2 = \frac{(e_0a)^2 \rho A}{30L} \begin{bmatrix} 36 & 3L & -36 & 3L \\ 3L & 4L^2 & -3L & -L^2 \\ -36 & -3L & 36 & -3L \\ 3L & -L^2 & -3L & 4L^2 \end{bmatrix}. \tag{25b}$$

The vibration of the Euler–Bernoulli beam is found as follows:

$$|K - \omega^2 M| = 0, \tag{26}$$

where $K = K^b + K^{w1} + K^{w2}$, $M = M^1 + M^2$, and ω is frequency.

3.2. Thermal Effect on the Vibrational Response of Embedded Nanowires

Here, the effect of temperature change on the natural frequencies of embedded nanowires in a thermal environment is investigated. Equation (16) can be rewritten in the presence of thermal loading as:

$$(EI - N^T(e_0a)^2) \frac{\partial^4 w}{\partial x^4} + k_w w + (N^T - k_w(e_0a)^2) \frac{\partial^2 w}{\partial x^2} + \rho A \frac{\partial^2 w}{\partial t^2} - \rho A(e_0a)^2 \frac{\partial^4 w}{\partial x^2 \partial t^2} = 0, \tag{27}$$

where the additional term N^T is the axial load resulting from the temperature change and can be defined as [28]:

$$N^T = \frac{EA}{1 - 2\nu} \alpha \Delta T, \tag{28}$$

in which α is the thermal expansion coefficient in the axial direction, ΔT is the temperature change, and ν is Poisson’s ratio. It is notable that only an axial load resulting from temperature change exists for the nanowires in this study [28].

The following Navier’s solution procedure is applied to achieve simply supported (S-S) nanowires as an illustrative example:

$$w(x, t) = \sum_{n=1}^{\infty} W_n \sin \beta e^{i\omega_n t}, \tag{29}$$

where n is the mode number, W_n is the unknown Fourier coefficient, and $\beta = \frac{n\pi x}{L}$. Using Equation (29) in Equation (27) yields the following relation for small-scale-dependent natural frequencies of embedded S-S nanowires that includes the thermal effect:

$$\omega_n = \sqrt{\frac{\beta^4 (EI - N^T(e_0a)^2) + k_w - \beta^2 (N^T - k_w(e_0a)^2)}{\rho A (1 + \beta^2(e_0a)^2)}}. \tag{30}$$

4. Results and Discussion

In this section, frequency values of nanowires were obtained with various non-dimensional small-scale parameters (e_0a/L), different non-dimensional Winkler foundation parameters (K_W), different boundary conditions, and different number of elements (N). The material properties for the three nanowires are listed in Table 1. The results obtained were shown in tables and graphs. The dimensionless Winkler parameter used for the results is expressed as the formula below:

$$K_W = \frac{k_w L^4}{EI}. \tag{31}$$

Table 1. Material properties of the nanowires.

Material Properties	SiCNW	AuNW	AgNW
E (GPa)	524.8	79	82.7
ν	0.14	0.42	0.37
ρ (kg/m ³)	3100	19,320	10,490
α (1/)	3.7×10^{-6}	14.2×10^{-6}	19.68×10^{-6}

Table 2 presents the natural frequencies of nanowires with C-C, C-S, S-S, and C-F boundary conditions. Finite element solutions for the three nanowires were compared with each other. It was clearly observed from the table that the highest frequency value occurred for both SiCNW and the C-C boundary condition, while the lowest value was seen in both AuNW and C-F boundary conditions.

Table 2. The first three natural frequencies (GHz) of isolated nanowires for four different boundary conditions ($K_W = 0, e_0a/L = 0.1$).

Mode Number	SiCNW			
	C-C	C-S	S-S	C-F
1	21.8286	15.0969	9.7369	3.5540
2	52.7211	43.2195	34.5672	19.7887
3	88.6384	77.4034	66.8450	48.0785
Mode Number	AuNW			
	C-C	C-S	S-S	C-F
1	3.3525	2.3186	1.4954	0.5458
2	8.0970	6.6378	5.3089	3.0392
3	13.6133	11.8878	10.2662	7.3840
Mode Number	AgNW			
	C-C	C-S	S-S	C-F
1	4.6550	3.2195	2.0764	0.7579
2	11.2430	9.2167	7.3716	4.2200
3	18.9025	16.5066	14.2550	10.2529

Tables 3–6 show natural frequencies of embedded simply supported nanowires for $K_W = 1, K_W = 10, K_W = 100,$ and $K_W = 1000,$ respectively, with different e_0a/L values. It was found from these tables that frequency values increased as K_W values increased, but frequencies decreased by increasing e_0a/L . Moreover, it was evident that small-scale effects became more considerable for higher modes.

Table 3. The first three natural frequencies (GHz) of embedded nanowires corresponding to various values of e_0a/L ($K_W = 1$).

Mode Number	SiCNW			
	e_0a/L			
	0.0	0.1	0.2	0.3
1	10.2583	9.7916	8.7034	7.4989
2	40.8373	34.5827	25.4413	19.1602
3	91.8603	66.8530	43.0600	30.6452
Mode Number	AuNW			
	e_0a/L			
	0.0	0.1	0.2	0.3
1	1.5755	1.5038	1.3367	1.1517
2	6.2719	5.3113	3.9073	2.9427
3	14.1081	10.2675	6.6133	4.7066
Mode Number	AgNW			
	e_0a/L			
	0.0	0.1	0.2	0.3
1	2.1876	2.0881	1.8560	1.5992
2	8.7087	7.3749	5.4255	4.0860
3	19.5896	14.2567	9.1827	6.5352

Table 4. The first three natural frequencies (GHz) of embedded nanowires for various values of e_0a/L ($K_W = 10$).

SiCNW				
Mode Number	e_0a/L			
	0.0	0.1	0.2	0.3
1	10.7171	10.2713	9.2398	8.1152
2	40.9550	34.7215	25.6298	19.4097
3	91.9126	66.9249	43.1716	30.8018
AuNW				
Mode Number	e_0a/L			
	0.0	0.1	0.2	0.3
1	1.6460	1.5775	1.4191	1.2464
2	6.2900	5.3326	3.9363	2.9810
3	14.1162	10.2785	6.6304	4.7306
AgNW				
Mode Number	e_0a/L			
	0.0	0.1	0.2	0.3
1	2.2855	2.1904	1.9704	1.7306
2	8.7338	7.4045	5.4656	4.1392
3	19.6007	14.2720	9.2065	6.5686

Table 5. The first three natural frequencies (GHz) of embedded nanowires with respect to various values of e_0a/L ($K_W = 100$).

SiCNW				
Mode Number	e_0a/L			
	0.0	0.1	0.2	0.3
1	14.5292	14.2035	13.4764	12.7318
2	42.1135	36.0808	27.4431	21.7480
3	92.4347	67.6401	44.2722	32.3263
AuNW				
Mode Number	e_0a/L			
	0.0	0.1	0.2	0.3
1	2.2314	2.1814	2.0697	1.9554
2	6.4679	5.5414	4.2148	3.3401
3	14.1964	10.3883	6.7994	4.9648
AgNW				
Mode Number	e_0a/L			
	0.0	0.1	0.2	0.3
1	3.0984	3.0290	2.8739	2.7151
2	8.9809	7.6944	5.8524	4.6379
3	19.7121	14.4245	9.4412	6.8937

Table 6. The first three natural frequencies (GHz) of embedded nanowires against various values of $\epsilon_0 a/L$ ($K_W = 1000$).

SiCNW				
Mode Number	$\epsilon_0 a/L$			
	0.0	0.1	0.2	0.3
1	34.2564	34.1196	33.8234	33.5336
2	52.3064	47.5839	41.4190	37.8864
3	97.5017	74.4150	54.0595	44.8040
AuNW				
Mode Number	$\epsilon_0 a/L$			
	0.0	0.1	0.2	0.3
1	5.2612	5.2402	5.1947	5.1502
2	8.0333	7.3081	6.3612	5.8187
3	14.9746	11.4288	8.3026	6.8811
AgNW				
Mode Number	$\epsilon_0 a/L$			
	0.0	0.1	0.2	0.3
1	7.3053	7.2761	7.2130	7.1512
2	11.1545	10.1475	8.8328	8.0794
3	20.7926	15.8693	11.5284	9.5546

In Table 7, the frequency values of C-C nanowires are given by analytical and finite element solutions for $\epsilon_0 a/L = 0.2$. For the finite element solution, as the element number increased, the results approached the real value.

Effects of both temperature rise and the Winkler parameter on the first three natural frequencies of nanowires are revealed in Table 8. It is apparent from the table that an increase temperature rise led to a decrease in frequency, contrary to the Winkler parameter. Also, it can be emphasized that the frequencies of AuNW were more affected than the other nanowires because of their related material properties, given in Table 1. Moreover, it can be observed that the influence of temperature rise was more prominent for lower modes and smaller Winkler parameters.

Table 7. Convergence of the present results with the analytical results of different element numbers.

SiCNW								
Mode Number	N							Analytical
	4	5	6	7	8	9	10	
1	18.9418	18.9252	18.9189	18.9162	18.9148	18.9141	18.9137	18.9129
2	38.0339	37.8398	37.7549	37.7155	37.6955	37.6845	37.6781	37.6656
3	56.8236	57.2104	56.8478	56.6515	56.5467	56.4878	56.4529	56.3826
AuNW								
Mode Number	N							Analytical
	4	5	6	7	8	9	10	
1	2.9091	2.9066	2.9056	2.9052	2.9050	2.9049	2.9048	2.9047
2	5.8413	5.8115	5.7985	5.7924	5.7894	5.7877	5.7867	5.7848
3	8.7271	8.7865	8.7308	8.7007	8.6846	8.6755	8.6702	8.6594
AgNW								
Mode Number	N							Analytical
	4	5	6	7	8	9	10	
1	4.0394	4.0359	4.0345	4.0340	4.0337	4.0335	4.0334	4.0332
2	8.1109	8.0695	8.0514	8.0430	8.0387	8.0364	8.0350	8.0323
3	12.1179	12.2003	12.1230	12.0811	12.059	12.0462	12.0388	12.0238

Table 8. The first three small-scale-dependent natural frequencies (GHz) of embedded nanowires for different Winkler parameters and temperature changes ($e_0a/L = 0.1$, $d = 1$ nm, and $L = 20$ d).

Mode Number	SiCNW					
	$\Delta T = 0$			$\Delta T = 30\text{ }^\circ\text{C}$		
	$K_w = 100$	$K_w = 500$	$K_w = 1000$	$K_w = 100$	$K_w = 500$	$K_w = 1000$
1	17.7768	31.4013	42.7034	17.3120	31.1405	42.5119
2	45.1580	52.0507	59.5551	44.4297	51.4201	59.0047
3	84.6569	88.5259	93.1362	83.7854	87.6928	92.3448
Mode Number	AuNW					
	$\Delta T = 0$			$\Delta T = 30\text{ }^\circ\text{C}$		
	$K_w = 100$	$K_w = 500$	$K_w = 1000$	$K_w = 100$	$K_w = 500$	$K_w = 1000$
1	2.7628	4.8802	6.6368	0.9103	4.1246	6.1026
2	7.0182	8.0895	9.2558	4.6945	6.1824	7.6454
3	13.157	13.7583	14.4748	10.5767	11.3159	12.177
Mode Number	AgNW					
	$\Delta T = 0$			$\Delta T = 30\text{ }^\circ\text{C}$		
	$K_w = 100$	$K_w = 500$	$K_w = 1000$	$K_w = 100$	$K_w = 500$	$K_w = 1000$
1	3.8362	6.7764	9.2153	1.8782	5.8932	8.5868
2	9.7450	11.2325	12.8519	7.0859	9.0229	10.9734
3	18.2689	19.1038	20.0987	15.2661	16.2559	17.4143

Effects of nanoscale and foundation parameters on the first five natural frequencies are respectively depicted in Figures 2 and 3. It can be concluded from these figures that size dependency was more pronounced for higher modes, while the natural frequencies in lower modes were more affected from foundation parameters. As stated before, it was clear that the natural frequencies decreased and increased by increasing e_0a/L and K_w , respectively.

Figure 4 displays the variation of fundamental frequencies of the three embedded nanowires with respect to temperature rise for various small-scale parameter values. It can be recognized from the figure that the effect of e_0a/L was more prominent for SiCNW than the other ones. On the other hand, the influence of temperature rise was more significant for gold and silver nanowires than the silicon carbide nanowire.

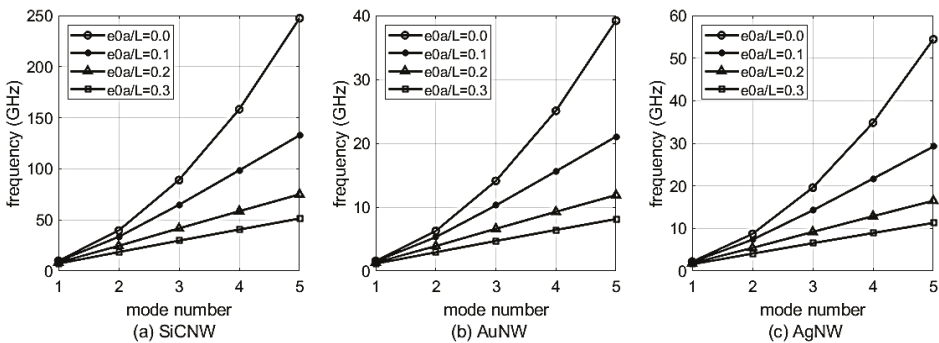


Figure 2. Variation of the first five natural frequencies of nanowires with respect to e_0a/L .

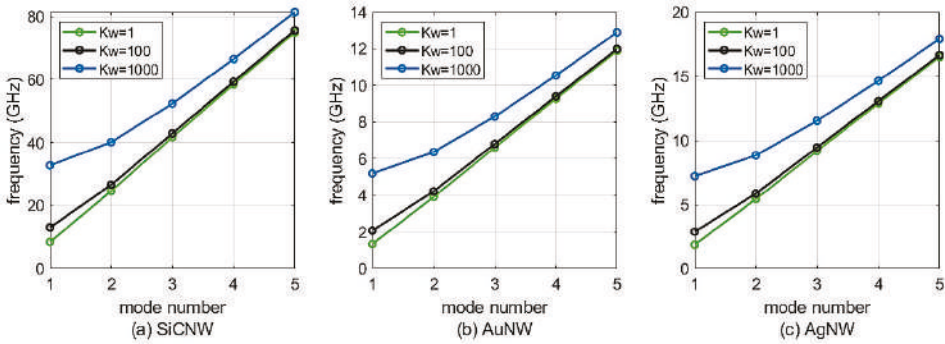


Figure 3. Effect of the Winkler parameter on the first five natural frequencies of nanowires.

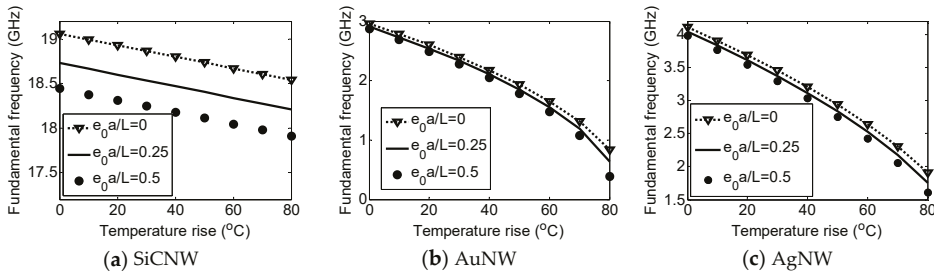


Figure 4. Variation of the fundamental frequency for several e_0a/L against temperature rise ($L = 30$ d, $K_w = 1000$).

5. Conclusions

Three types of nanowires, SiCNW, AgNW, and AuNW, are modeled as nonlocal Euler–Bernoulli nanobeams resting on a Winkler elastic foundation. Frequency values of these nanowires are obtained via a finite element solution, and results are given by tables and graphs. The effect of temperature change on the vibrational responses of simply supported nanowires is also examined as a case study. It can be concluded from the results that among all boundary conditions, C-C has the highest frequency values and C-F has the lowest ones. Also, it can be emphasized that by increasing the Winkler parameter value, frequency values increase, while by increasing non-dimensional small-scale parameter (e_0a/L), frequency value decreases. When we compare the frequency values of nanowires, SiCNW has the highest frequency values, while AuNW has the lowest frequency values because of its different material properties. Additionally, it is revealed that the effects of temperature change and small-scale parameters on the frequencies of nanowires are both considerable and negligible depending on the values of the involved material properties.

Author Contributions: All authors contributed extensively to the present study. The derivation of the governing equations, obtaining and discussion of the numerical results, and writing the manuscript have been performed by B.U. and Ö.C.

Acknowledgments: This study was supported by The Scientific and Technological Research Council of Turkey (TÜBİTAK) with Project no: 117M495. This support is gratefully acknowledged.

Conflicts of Interest: The authors declare no conflict of interest.

References

1. Makeev, M.A.; Srivastava, D.; Menon, M. Silicon carbide nanowires under external loads: An atomistic simulation study. *Phys. Rev. B* **2006**, *74*, 165303. [[CrossRef](#)]
2. Schulz, M.; Shanov, V.; Yin, Z. (Eds.) *Nanotube Superfiber Materials: Changing Engineering Design*; William Andrew: Norwich, NY, USA, 2013.
3. Numanoğlu, H.M. *Nanoyapıların Kiriş ve Çubuk Modellerinin Yerel Olmayan Elastisite Teorisi Kullanılarak Titreşim Analizi*; Akdeniz Üniversitesi: Antalya, Turkey, 2017. (In Turkish)
4. Vazinishayan, A.; Yang, S.; Duongthipthewa, A.; Wang, Y. Effects of cross-section on mechanical properties of Au nanowire. *AIP Adv.* **2016**, *6*, 025006. [[CrossRef](#)]
5. Poole, W.J.; Ashby, M.F.; Fleck, N.A. Micro-hardness of annealed and work-hardened copper polycrystals. *Scr. Mater.* **1996**, *34*, 559–564. [[CrossRef](#)]
6. Mc Farland, A.W.; Colton, J.S. Role of material microstructure in plate stiffness with relevance to microcantilever sensors. *J. Micromech. Microeng.* **2005**, *15*, 1060–1067. [[CrossRef](#)]
7. Zhang, C.-L.; Shen, H.-S. Predicting the elastic properties of double-walled carbon nanotubes by molecular dynamics simulation. *J. Phys. D Appl. Phys.* **2008**, *41*, 055404. [[CrossRef](#)]
8. Toupin, R.A. Elastic materials with couple-stresses. *Arch. Ration. Mech. Anal.* **1962**, *11*, 385–414. [[CrossRef](#)]
9. Mindlin, R.D.; Tiersten, H.F. Effects of couple-stresses in linear elasticity. *Arch. Ration. Mech. Anal.* **1962**, *11*, 415–448. [[CrossRef](#)]
10. Koiter, W.T. Couple stresses in the theory of elasticity, I and II. *Proc. K. Ned. Akad. Wet. B* **1964**, *67*, 17–44.
11. Yang, F.; Chong, A.C.M.; Lam, D.C.C.; Tong, P. Couple stress based strain gradient theory for elasticity. *Int. J. Solids Struct.* **2002**, *39*, 2731–2743. [[CrossRef](#)]
12. Mindlin, R.D. Second gradient of strain and surface-tension in linear elasticity. *Int. J. Solids Struct.* **1965**, *1*, 417–438. [[CrossRef](#)]
13. Lam, D.C.C.; Yang, F.; Chong, A.C.M.; Wang, J.; Tong, P. Experiments and theory in strain gradient elasticity. *J. Mech. Phys. Solids* **2003**, *51*, 1477–1508. [[CrossRef](#)]
14. Eringen, A.C. On differential equations of nonlocal elasticity and solutions of screw dislocation and surface waves. *J. Appl. Phys.* **1983**, *54*, 4703–4710. [[CrossRef](#)]
15. Nejad, M.Z.; Hadi, A.; Rastgoo, A. Buckling analysis of arbitrary two-directional functionally graded Euler–Bernoulli nano-beams based on nonlocal elasticity theory. *Int. J. Eng. Sci.* **2016**, *103*, 1–10. [[CrossRef](#)]
16. Akgöz, B.; Civalek, Ö. Bending analysis of FG microbeams resting on Winkler elastic foundation via strain gradient elasticity. *Compos. Struct.* **2015**, *134*, 294–301. [[CrossRef](#)]
17. Akgöz, B.; Civalek, Ö. Bending analysis of embedded carbon nanotubes resting on an elastic foundation using strain gradient theory. *Acta Astronaut.* **2016**, *119*, 1–12.
18. Togun, N.; Bağdatlı, S.M. The vibration of nanobeam resting on elastic foundation using modified couple stress theory. *Tehnički Glasnik* **2018**, *12*, 221–225. [[CrossRef](#)]
19. Pradhan, S.C.; Phadikar, J.K. Nonlocal elasticity theory for vibration of nanoplates. *J. Sound Vib.* **2009**, *325*, 206–223. [[CrossRef](#)]
20. Uymaz, B. Forced vibration analysis of functionally graded beams using nonlocal elasticity. *Compos. Struct.* **2013**, *105*, 227–239. [[CrossRef](#)]
21. Togun, N. Nonlocal beam theory for nonlinear vibrations of a nanobeam resting on elastic foundation. *Bound. Value Probl.* **2016**, *1*, 57. [[CrossRef](#)]
22. Rahmanian, M.; Torkaman-Asadi, M.A.; Firouz-Abadi, R.D.; Kouchakzadeh, M.A. Free vibrations analysis of carbon nanotubes resting on Winkler foundations based on nonlocal models. *Phys. B Condens. Mat.* **2016**, *484*, 83–94. [[CrossRef](#)]
23. Demir, Ç.; Civalek, Ö. A new nonlocal FEM via Hermitian cubic shape functions for thermal vibration of nano beams surrounded by an elastic matrix. *Compos. Struct.* **2017**, *168*, 872–884. [[CrossRef](#)]
24. Pradhan, S.C. Nonlocal finite element analysis and small scale effects of CNTs with Timoshenko beam theory. *Finite Elem. Anal. Des.* **2012**, *50*, 8–20. [[CrossRef](#)]
25. Rajasekaran, S.; Bakhshi Khaniki, H. Finite element static and dynamic analysis of axially functionally graded nonuniform small-scale beams based on nonlocal strain gradient theory. *Mech. Adv. Mat. Struct.* **2018**, *1*–15. [[CrossRef](#)]

26. Eltaher, M.A.; Emam, S.A.; Mahmoud, F.F. Free vibration analysis of functionally graded size-dependent nanobeams. *Appl. Math. Comput.* **2012**, *218*, 7406–7420. [[CrossRef](#)]
27. Nejad, M.Z.; Hadi, A. Eringen's non-local elasticity theory for bending analysis of bi-directional functionally graded Euler–Bernoulli nano-beams. *Int. J. Eng. Sci.* **2016**, *106*, 1–9. [[CrossRef](#)]
28. Murmu, T.; Pradhan, S.C. Thermo-mechanical vibration of a single-walled carbon nanotube embedded in an elastic medium based on nonlocal elasticity theory. *Comput. Mat. Sci.* **2009**, *46*, 854–859. [[CrossRef](#)]
29. Reddy, J.N. Nonlocal theories for bending, buckling and vibration of beams. *Int. J. Eng. Sci.* **2007**, *45*, 288–307. [[CrossRef](#)]
30. Tornabene, F.; Baccocchi, M.; Fantuzzi, N.; Reddy, J.N. Multiscale Approach for Three-Phase CNT/Polymer/Fiber Laminated Nanocomposite Structures. *Polym. Compos.* **2019**, *40*, 102–126. [[CrossRef](#)]
31. Fantuzzi, N. New insights into the strong formulation finite element method for solving elastostatic and elastodynamic problems. *Curved Layer. Struct.* **2014**, *1*, 93–126.
32. Civalek, O. Free vibration of carbon nanotubes reinforced (CNTR) and functionally graded shells and plates based on FSDT via discrete singular convolution method. *Compos. Part B Eng.* **2017**, *111*, 45–59. [[CrossRef](#)]
33. Civalek, O. Nonlinear dynamic response of laminated plates resting on nonlinear elastic foundations by the discrete singular convolution-differential quadrature coupled approaches. *Compos. Part B Eng.* **2013**, *50*, 171–179. [[CrossRef](#)]
34. Civalek, O.; Demir, C. Buckling and bending analyses of cantilever carbon nanotubes using the Euler-Bernoulli beam theory based on non-local continuum model. *Asian J. Civ. Eng.* **2011**, *12*, 651–661.
35. Civalek, O. *Finite Element Analysis of Plates and Shells*; Firat University: Elazığ, Turkey, 1998. (In Turkish)
36. Uzun, B.; Numanoğlu, H.M.; Civalek, O. Free Vibration Analysis of BNNT with Different Cross-Sections via Nonlocal FEM. *J. Comput. Appl. Mech.* **2018**, *49*, 252–260.
37. Omurtag, M.H. *Çubuk Sonlu Elemanlar*; Birsen Yayınevi: Istanbul, Turkey, 2010. (In Turkish)
38. Işık, Ç. *Mikro ve Nano Ölçekli Mekanik Sistemlerin Modellenmesinde Yerel Olmayan Sonlu Eleman Formülasyonu*; Akdeniz Üniversitesi: Antalya, Turkey, 2018. (In Turkish)



© 2019 by the authors. Licensee MDPI, Basel, Switzerland. This article is an open access article distributed under the terms and conditions of the Creative Commons Attribution (CC BY) license (<http://creativecommons.org/licenses/by/4.0/>).

Article

Trustworthiness in Modeling Unreinforced and Reinforced T-Joints with Finite Elements

Slimane Ouakka and Nicholas Fantuzzi *

DICAM Department, University of Bologna, Viale del Risorgimento 2, 40136 Bologna, Italy; souakka@gmail.com

* Correspondence: nicholas.fantuzzi@unibo.it; Tel.: +39-051-2093494

Received: 26 November 2018; Accepted: 16 February 2019; Published: 20 February 2019

Abstract: As required by regulations, Finite Element Analyses (FEA) can be used to investigate the behavior of joints which might be complex to design due to the presence of geometrical and material discontinuities. The static behavior of such problems is mesh dependent, thus these results must be calibrated by using laboratory tests or reference data. Once the Finite Element (FE) model is correctly setup, the same settings can be used to study joints for which no reference is available. The present work analyzes the static strength of reinforced T-joints and sheds light on the following aspects: shell elements are a valid alternative to solid modeling; the best combination of element type and mesh density for several configurations is shown; the ultimate static strength of joints can be predicted, as well as when mechanical properties are roughly introduced for some FE topologies. The increase in strength of 12 unreinforced and reinforced (with collar or doubler plate) T-joints subjected to axial brace loading is studied. The present studies are compared with the literature and practical remarks are given in the conclusion section.

Keywords: numerical modeling; joint static strength; finite element method; parametric investigation; reinforced joint (collar and doubler plate)

1. Introduction

Joints in offshore engineering are crucial because they are key components in the design of jacket structures. The study of joints is generally performed after a pre-dimensioning of the complete jacket has been carried out. Jacket structures are investigated using simple lattice models made of beams which simulate the tubular elements of the whole structures. Such simple model is extremely convenient for global structural analysis but does not give enough detail regarding local structural failure such as fatigue cracking at joints. For this reason, several authors in the past and recent years investigated the problem of static and dynamic strength of offshore extensively [1–17]. Among these, Moffat et al. [1] investigated the effect of the chord length and the applied boundary conditions on the static strength of tubular T-joints. Ring stiffened DT-joints (cross shaped) have been studied by Marcus et al. [3]; the dynamic performance of collar plate reinforced joints was studied by Qu et al. [10]. Numerical and experimental studies on the ultimate strength of KT-joints (K shaped) were presented by Li et al. [15].

On the other hand, in the recent studies some researchers have investigated in detail the concentration of the stress and its distribution in critical areas [18–23], where Løstberg [18], Osawa et al. [19] and Lotfollahi-Yagin et al. [20] have focused on the stress hot spots in tubular joints, whereas, Cheng et al. [21] investigated how the concentration of the stress affect the fatigue.

In addition to the aforementioned researches, other studies that involved joints should be mentioned [24–46], such as the work by Xia et al. [24] regarding the hysteretic behavior of stiffened T-joints. Furthermore, Dong et al. [28] presented long-term fatigue analysis of multi-planar tubular joints. Finally, experimental tests were performed on joints using white light speckle method by

Liu [32]. Numerical implementation and coupling of finite elements of different topology in the study of joints were proposed by Pey et al. [33], and a good review on finite and boundary element methods was given by Mackerle [34,35]. Regarding the topic of composite structures, the work by Chowdhury et al. [41] and Shen et al. [42] should be cited for their application to practical engineering practices for the static and fatigue strength of joints. Finally, the parametric study on composite joints by Liu et al. [46] is mentioned for their thorough description of this particular problem.

The present work investigates tubular joints made of steel Circular Hollow Sections (CHSs) that are the main structural components of steel off-shore structures such as jackets, compliant towers, jack-ups, etc. In these kinds of structures, the CHSs members are joined in a point, forming a tubular simple joint by welding the profiled ends of the secondary members, the braces, onto the circumference of the main member, the chord.

Due to their crucial rule, some guidelines and methods have been introduced, to guarantee the needed serviceability and to understand the strength behavior of these type of element, the most used are: American Petroleum Institute (API) [47], International Organization for Standardization (ISO) [48], American Bureau of Shipping (ABS) [49], and Eurocode3 (EC3) [50].

Several types of reinforcement are available nowadays in order to enhance the strength of tubular joints. One typology that can be found often in off-shore is schematically shown in the sections depicted in Figure 1, where the collar plate (a) consists in flat surface around the brace-chord intersection, whereas the doubler plate (b) is a surface in between the two elements. These two methods are widely used since they can be an important improvement either for rehabilitation purposes in old structures or for new structures.

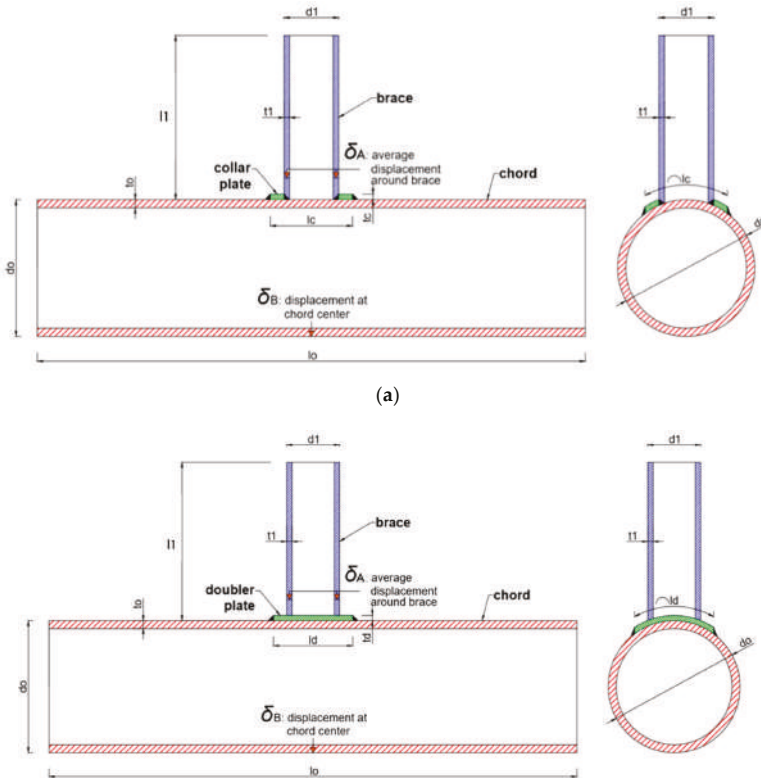


Figure 1. Scheme of specimens: (a) collar plate reinforcement and (b) doubler plate reinforcement.

Thus, for a better understanding of the static strength of joints with the introduction of the two types of reinforcement, 12 T-Joint specimens subjected to axial brace load (6 in compression and 6 in tension) have been studied, with different geometric and material parameters. T-joints have been selected in this investigation even though several types of joints can be formed in lattice structures such as Y, K, and X joints or their combinations. Based on this study, conclusions can be obtained in assessing the reinforcing efficiency.

The aforementioned guidelines [47–50] suggest using FE models whenever new configuration of joint are treated, but the sharp geometric discontinuities (wherein stress concentrations occur) in the tubular joints lead to a mesh dependence for the results and so such FE models need to be calibrated by considering reference data such as laboratory tests. In the present paper, the works [4,5] have been considered as a reference.

The reference paper [5] considers a 3-D solid FE model, on the contrary the present research simplifies the problem by modeling the joints with less degrees of freedom and a much simpler geometric description. Shell elements are used in this research because of their simplicity and the lower cost in terms of computational time with respect to solid elements. Moreover, the geometry of FE models made of solid elements is more difficult to generate and assemble with respect to 2-D shell elements. In the reference 3-D simulations [5] the authors decided to deploy solid elements instead of 2-D elements, mainly because: the contact algorithm will only identify contact between two members if the shell elements (which represent the mid-surfaces of each member) touch each other, thereby incorrectly allowing penetration of one member into the other, in addition to preventing the uncertainty in modeling the welded area of the brace-chord intersection. Therefore, succeeding in solving the aforementioned limits, as will be showed in the following sections, shell elements can be used instead of solid elements as in the present research.

The present work considers the commercial finite element ABAQUS package, since it offers an attractive alternative to generate reliable data, provided that the accuracy of the FE model is firstly verified against test evidence. In particular, ABAQUS 6.14 will be used for all the simulations.

2. Previous Researches

The aim of the work, as has been already aforementioned, is to improve the understanding of the static behavior of plate reinforced joints, by building an FE model with shell elements. This is generally required from the regulations when new joint configurations are studied, but since stress concentrations computed by FE are mesh dependent, they need to be calibrated with the help of laboratory tests [4].

The reference papers present an experimental investigation and a numerical simulation. The numerical simulation has been considered here to have the possibility of discussing the improvement that have been obtained by the use of a different element topology. In this section, relevant information will be summarized. However, for an exhaustive description of the tests, the reader is invited to the articles [4,5].

2.1. Experimental Investigations

Laboratory tests are one useful way to calibrate numerical simulations. The basic configuration and the T-joint geometries are illustrated in Figure 1. The experimental program consists of 12 tests, of unreinforced and reinforced with collar or doubler plates, as depicted in Figure 1. Joints have been tested under both compression and tension loading. The geometric data indicated in Figure 1 are listed in Table 1, except for the joint lengths that are constant for all twelve specimens, respectively: $l_0 = 2840$ mm, $l_1 = 1100$ mm, and $l_d = l_c = 305$ mm.

Table 1. Geometrical details of the twelve T-joint specimens.

	Type	d_0	d_1	t_0	t_1	t_d	Brace Loading
EX – 01	Unreinforced	409.5	221.9	8.1	6.8	-	Compression
EX – 02	Unreinforced	409.5	221.9	8.1	6.8	-	Tension
EX – 03	Collar	409.5	221.9	8.1	6.8	6.4	Compression
EX – 04	Collar	409.5	221.9	8.5	6.8	6.4	Tension
EX – 05	Collar	409.5	221.9	12.8	8.4	8.3	Compression
EX – 06	Collar	409.5	221.9	12.8	8.4	8.3	Tension
EX – 07	Doubler	409.5	221.9	8.5	6.8	6.6	Compression
EX – 08	Doubler	409.5	221.9	8.2	6.5	6.4	Tension
EX – 09	Unreinforced	409.5	114.7	8.5	5.9	-	Compression
EX – 10	Unreinforced	409.5	114.7	8.5	5.9	-	Tension
EX – 11	Doubler	409.5	114.7	8.5	5.9	6.6	Compression
EX – 12	Doubler	409.5	114.7	8.5	5.9	6.6	Tension

The materials used in each test are fabricated from carbon steel pipe, using the guidelines given from the API 5L Gr. B/ASTM A106-94A; while the welding procedure follows AWS D1.1. Table 2 indicates the measured yield stress for each steel component of the chord $f_{y,0}$, brace $f_{y,1}$, and reinforcement $f_{y,d}$.

Table 2. Material properties and yield stresses of the twelve T-joint specimens.

	$f_{y,0}$ [N/mm ²]	$f_{y,1}$ [N/mm ²]	$f_{y,d}$ [N/mm ²]
EX – 01	285	300	-
EX – 02	285	300	-
EX – 03	285	300	461
EX – 04	276	300	461
EX – 05	276	275	464
EX – 06	276	275	464
EX – 07	276	300	461
EX – 08	312	284	461
EX – 09	276	312	-
EX – 10	276	312	-
EX – 11	276	312	461
EX – 12	276	312	461

Each specimen is pin-supported at the chord ends to minimize the possibility of axial load, and the brace is bolted at the top. The load is applied through a displacement-controlled actuator that has a rated compression capacity of 2000 kN, a tension capacity of 1200 kN, and range of displacement of ± 200 mm. In all tests, the load is applied at initial stage at rate of 0.3 mm/min for the linear part and increased up to 1.2 mm/min through the Instron 8800 controller [4].

2.2. Numerical Simulations

The present section illustrates the details of the numerical simulations performed with 3-D solid elements in the reference [5]. Strength and weaknesses of all the modeling details provided are listed below.

The analysis considers the dimensions of the tubular members reported in Table 1, whereas for the materials properties Table 2 has been considered. Major aspects of the reference FE strategy adopted for the T-joints test, such as element type, mesh density, and contact interaction, are described below.

The T-joint specimen is simply supported with symmetric brace axial load [5], therefore the model has been simplified by considering a quarter of the whole model; and solid elements were selected to model the tubular joints, obviously these elements account for the joint dimensions in all three directions. Alternatively, mesh size is composed in such a way to be relatively smaller where the

stress gradient is more critical, therefore the density of the mesh decreases from the vicinity of the intersection to the end of the brace or chord.

In the reference [5], the authors stated that: “Weld geometry was modeled using a ring of shell elements along the brace-chord” and that: “the penetration weld between the brace and the doubler plate is modeled in accordance with the measured dimensions obtained from the T-joint specimens”. However, the graphical representation, presented in the papers [4,5], shows solid elements also for the welded area, instead of the mentioned shell elements. Therefore, a detailed size of the weld is not given in [4] or [5].

Since in this case the plate reinforced joints are loaded by an axial force/displacement, contact shall occur between bottom surface of the reinforcement and the external surface of the chord. Thus, contact plays a main rule as transferring mechanism from the secondary element (brace) to the primary one (chord), and this is a source of nonlinearity in the FE analysis. Due to the fact that both reinforcement and chord walls are deformable bodies, a deformable-deformable contact interaction is defined using a “master-slave” algorithm in the numerical analysis, with no friction between the members is assumed.

According to the experimental investigations, the axial load is applied using the displacement control method by prescribing the vertical displacement of the nodes at the brace tip.

The true stress-strain relationship enforced in these simulations is related to the yielding point of each material, as given in Table 2, and can be represented by a bilinear relationship. No further hardening in the true stress-true strain behavior is assumed after the peak load in the engineering stress-strain curve, i.e., the true stress-true strain curve is assumed to remain horizontal beyond this point as for elastic-perfectly plastic model, as shown in Figure 2a. Contrastingly, the welds are assumed to have the same material properties as the base metal.

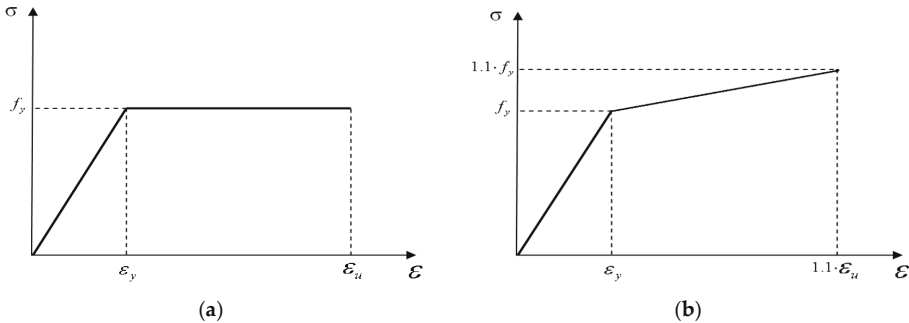


Figure 2. True stress-strain relationships: (a) without hardening and (b) with 10% hardening.

The use of this simplification in the true stress-strain relationship is commonly used in the design of structures because allows the designer to stay in the safety size due to the fact that no hardening is considered. This approximation, though, can lead to a result slightly different from the real behavior. For this, in Section 6, in addition to the elastic-perfectly plastic model, a model where the hardening is taken into account, as in Figure 2b, will also be considered.

2.3. Comparison Setup

More detailed information about the results of the two investigations will be given in the next section while showing the results of the work made during this research. However, in this section the main point of data collecting and how the results have been shown by the authors of [4,5] will be given. In general, the results of the two papers can be summarized in just one, since they are two parts of the same study. The results given by the references are given in terms of load-ovalization curves and deformed shapes.

The load-ovalization curves are presented, where the ovalization indicates the deformation of the chord cross section at the center of the T-joint, which is calculated by subtracting the height of point fixed simultaneously at the bottom of the chord and at the center of the joint, δ_B , from the average value of four fixed points (in the one quarter FE model of course will be only two) on the brace near the intersection with the chord, δ_A . These points are obtained by the transducer reading in case of experimental investigation, whereas for the FE model by using RP (Reference Point) as shown in Figure 1. The ultimate load for each test is identified simply by selecting the peak of each curve, and these values are listed in Table 3, where $F_{u,test}$ is for the experimental investigations [4] while $F_{u,num}$ for the numerical simulations [5]. At the same time, the two phases of the joint behavior, such as the linear phase and the plastic one, can be deducted.

Table 3. Ultimate load obtained in the numerical simulation [5].

	$F_{u,test}$ [kN]	$F_{u,num}$ [kN]	$F_{u,num}/F_{u,test}$
EX – 01	305.1	310.9	1.02
EX – 02	543.2	557.8	1.03
EX – 03	425.6	431.4	1.01
EX – 04	609.2	648.9	1.07
EX – 05	780.0	798.5	1.02
EX – 06	1065.3	1069.3	1.00
EX – 07	415.8	446.4	1.07
EX – 08	708.0	712.2	1.01
EX – 09	200.1	193.0	0.96
EX – 10	407.8	393.7	0.97
EX – 11	305.0	309.3	1.01
EX – 12	520.0	506.2	0.97

The experimental [4] and numerical [5] results are not only evaluated in terms of load-ovalization curves but also by comparison of deformed sliced “rings”, taken at the center of the T-joints after the tests and numerical analyses were completed. Then at the end of the tests, for some of the specimens, sections or “rings” were obtained for the joint elements, chord and brace.

In conclusion, all the results obtained from these two papers will be used in the fundamental step of calibration of the FE model of the present work. In the following section the results of the present FE simulations will be compared to the ones of the previous studies and comments and highlights will be provided.

3. Present Modeling

Commercial finite element packages offer an attractive and cheaper alternative to the laboratory experiments, but at the same time they require the use of sophisticated hardware, and also need the help of other software to post-processing the results. Hence, different software have been used, such as Abaqus/CAE 6.14-1 [51], Matlab R2017a, and AutoCAD 2017. The hardware used is the Intel(R) Core(TM) i7-4700MQ CPU @ 2.40GHz 2.40 GHz with 12GB of RAM.

This section addresses various aspects of all the steps that have been performed to study and simulate the state of T-joints subjected to the axial force. The cheaper shell elements have been used in this work, whereas the numerical simulation made in [5] considered solid elements.

The dimensions of the tubular members and reinforcement plates assumed in this research are in accordance with the measured dimensions of the test specimen of the papers as sketched in Figure 1, for which the values are reported in Table 1. In contrast, Table 2 summarizes the measured yield stress for each chord $f_{y,0}$, brace $f_{y,1}$, and reinforcement $f_{y,d}$.

Although the type of element material is specified in the reference papers [4,5] as carbon steel, the characteristics of this typology of material are not unique, especially concerning Young’s Modulus (E) and Poisson ratio (ν), where E ranges from 203 to 210 GPa whereas ν ranges from 0.25 to 0.3.

With the help of preliminary simulations, the more fitting values of these have been demonstrated to be $E = 210$ GPa and $\nu = 0.3$. These values were obtained by comparing the normalized load R , defined as $R = F_{u, test} / f_{y,0} \cdot t_0^2$ of the EX-01, where t_0 is the chord thickness, with the one given by the experimental investigations, as reported in Table 4.

Table 4. Values of E and ν of preliminary simulations [17].

Specimen	Experimental Investigation	Preliminary Simulation 1 $E = 203 \nu = 0.25$	Preliminary Simulation 2 $E = 210 \nu = 0.25$	Preliminary Simulation 3 $E = 210 \nu = 0.30$
$f_{y,0}$ [N/mm ²]	285	285	285	285
t_0 [mm]	8.1	8.1	8.1	8.1
$R = F_{u, test} / f_{y,0} \cdot t_0^2$	16.32	13.95	14.09	14.11

AutoCAD 3D was selected to draw the T-joint tubular elements. Although ABAQUS gives the possibility to directly represents different geometries, AutoCAD is a more suitable software for this kind of parametric research since it gives the possibility to easily modify and change elements on it. Afterwards, only a quarter of the joint has been imported in the FE packages, this idealization does not make any differences in the results and reduces the total computational effort.

Starting from the first adjustments of the simulations, the three cases are discussed below: unreinforced, collar plate reinforcement, and doubler plate reinforcement.

Three native parts have been created for the reinforced cases (chord, brace, and reinforcement plate), and only two for the unreinforced case because no reinforcement is present. Some internal parts have been introduced in the part module, with their respective edges. In other words, due to the fact that the joint is made of several parts and contact must be implemented in order to connect the different parts together, construction edges (from CAD) are kept in the FE model also in order to simplify the following step.

Once all the parts are created (in their own coordinate system), they should be assembled in the Abaqus Assembly module [51] that is used to create instances of the parts and to position the instances relative to each other in a global coordinate system. The instances made for all the three cases are one for each part. Then for the unreinforced case, two instances have been generated, one for the chord and the other for the brace; whereas for the reinforced cases a third instance that represents the reinforcement is present.

The displacement induced by the controlled actuator in the experimental investigation [4] is at an initial stroke rate of 0.3 mm/min, and then progressively increased up to 1.2 mm/min through the Instron 8800 controller. During the simulations in the present study, two types of step sequences are analyzed: the first automatic step sequence, and the second fixed step sequence, i.e., varying the load range during the simulations.

The automatic step sequence has the same step range for the whole simulation. While the fixed ones in order to reproduce the experimental investigation have two different ranges, in particular the second step starts at the starting point of the material plasticization which has been identified during the automatic step sequence.

The restraints that have been adopted for the FE model are in accordance with the experimental investigation; where the specimen is pin-supported at the chord ends and the brace end is bolted to the Instron actuator mounted on top of the brace, where the load is obtained as reaction force from the boundary condition at the brace tip. Since one-quarter of the whole specimen has been modeled, along with symmetry planes, peculiar boundary conditions have been considered as XSYMM (along the x -axis) and ZSYMM (along the z -axis) [51].

Material properties of the elements are modeled in accordance to the experimental investigation as listed in Table 2, whereas the Young’s modulus and Poisson ratio are taken from the preliminary simulations already described Table 4. The true stress-strain curve that has been assumed by var

der Vegte et al. [5] in his numerical simulations is represented by a multilinear relationship and subsequently converted into a true stress-true strain relationship, and no further hardening in the true stress-true strain behavior is assumed after the peak load, i.e., the curve is assumed horizontal beyond this point.

Since no more detailed information is given about the true strain-stress curve, in this study, the elastic-perfectly plastic model is assumed to fit these characteristics as shown in Figure 2a. Due to the lack in the reference paper [5] for what concerns the latter relationship, in this research some hardening will be considered during the simulations, by introducing a hardening of 10% for all the materials, as depicted in Figure 2b, to verify the reliability of the elastic-perfectly plastic model.

Currently, the following types of constraints have been used in the simulations, the multi-point constraints (MPC) [51], which allows the restriction imposed by the boundary conditions (BCs) along the whole circumference, and the TIE [51], which instead has been used to connect the edges of the elements to simulate the welded connections. However, since the brace is directly welded to the chord in the unreinforced cases, no separation will occur between the two elements and the two parts have been merged (i.e., combine two elements in one instance [51]) into a single one.

During the development of the contact between the chord and the reinforcement made for the reinforced T-joints, contact mechanical properties are imposed by fixing the relevant points, such as tangential and normal behavior in the contact interaction propriety. The tangential behavior was imposed as “Frictionless”, while the normal behavior as “Hard” contact. The contact properties are also imposed to “Allow separation after contact” since, in the case of the reinforced plate, separation between the plate and the chord that are linked, by the “tie” constraints, might occur. After the contact property is defined, surface-to-surface contact interaction is set up. Here the sliding is finite, and no adjustments are required since the two surfaces lie in the same plane. A further important feature is “Contact controls” option, which helps the convergence of the simulation without considering the penetration of one member into the other, as after solved using the Top/Bottom surface function [51].

The final results will be given in terms of load-ovalization curves; the ovalization was detected by the use of the transducers, so four reference points around the brace near the brace-chord intersection precisely at 20 mm distance, and one placed under the chord at the center of the T-joint have been introduced. The load detection is done by inserting an additional point at the tip of the brace, the reaction force at that point is indeed the opposite of the load applied. For the sake of further comparison, the deformed shape at the center of the joint will be considered

The FE mesh is a key point in modeling, since it has a huge influence on the results of the simulations in these kinds of elements, as will be seen when analyzing the results. The mesh module [51] allows generating meshes of parts and assemblies. For each FE model, four mesh densities are generated, and for each of them four types of elements are considered.

The four mesh densities analyzed are:

- Coarse mesh (average size 50 mm)
- Medium mesh (average size 20 mm)
- Fine mesh (almost the same number of elements as the medium ones but the size decreases from the ends to the intersection)
- Article mesh (same number of nodes on the edges shown in [5])

The four element types are:

- S4R (4 nodes with reduced integration)
- S4 (4 nodes without reduced integration)
- S8R (8 nodes with reduced integration and six degrees of freedom (DOF))
- S8R5 (8 nodes with reduced integration and five DOF)

In the “Mesh controls”, the “Structured” technique with element shape as “Quad-dominated” [51] was used for all the simulations. These two selections are able to carry out a regular mesh made (mostly) by quadrilaterals.

The four aforementioned meshes are used in this work to better understand the fitting of the results depending on the element size. In three of the four densities cases, the medium, fine, and article one, shown in Figure 3b–d, the doubling of the lines in the reinforcement area can be noticed. This is because the contact interaction algorithm needs two different meshes in order to have a reliable result of the contact [51]. In particular, the “slave surface” should have a finer mesh with respect to the “master surface”.

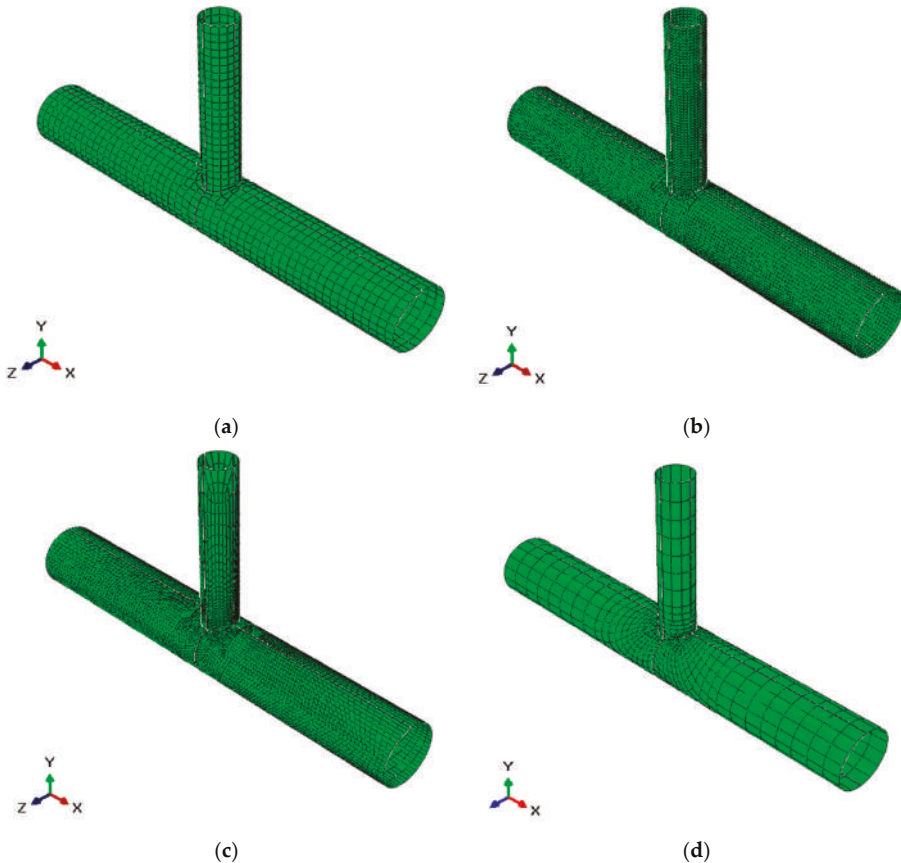


Figure 3. Meshes used in the simulations and their nomenclature: (a) coarse mesh, (b) medium mesh, (c) fine mesh, and (d) article mesh.

The coarse and medium mesh densities are obtained by imposing a unique size on the instance of the T-joint. The larger mesh has a size of 50, whereas the medium has a global size of 20, as depicted respectively in Figure 3a,b. The total number of elements is equal to 466 in coarse mesh, while 2745 elements are generated for the medium mesh. In the remaining cases, i.e., the fine and the article meshes depicted respectively in Figure 3c,d, the element sizes are varied in such a way that relatively smaller elements are used where the stress gradient is more critical. Therefore, the mesh density decreases from the vicinity of the intersection to the end of the brace or chord, and therefore smaller sizes in the vicinity of the brace-chord intersection. This strategy, to decrease the size while

getting close to the critical area, is frequently used in FE analysis, because it allows to have an accurate study of the area most influential thanks to the small sizes, and at the same time to reduce the computational effort, due to increase of the sizes far from the critical point. Fine mesh has almost the same number of elements of the medium mesh, but their sizes, as aforementioned, are decreasing while going close to the intersection. For the article mesh, as in the fine one, the sizes are smaller near the intersection, this mesh is obtained from the mesh used by var der Vegte et al. [5]. Precisely, an equal number of nodes at each edge with almost the same factor of variation (decrease in size) is considered, so a total of 341 elements is obtained. In particular, by using the proportion between the geometries of the specimens in Table 1 and the graphic dimensions displayed by var der Vegte et al. [5], it was possible to discretize the FE model as depicted in Figure 4, in order to have the same nodes of the paper [5] at edges as previously stated.

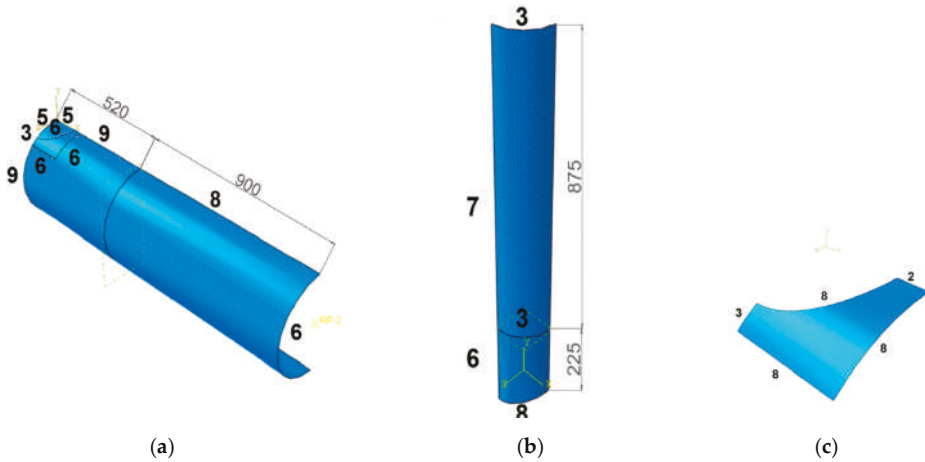


Figure 4. True article mesh density subdivision: (a) chord, (b) brace, and (c) reinforcement. [3]

From Figure 4a–c, it can be seen that the reinforcement and its respective area in the chord have different repartition, in particular three of the edges of the chord are increased by two units, i.e., from six to eight spaces. This is done to help the contact interaction as aforementioned. As a result, a total of 341 elements is obtained. For the final view of the specimen in the case of the article mesh please consider Figure 3d.

4. Results

The results of the research will be shown in this section, comparing them with the results of the two researches [4,5] discussed in Section 2. Therefore, in order to overlap the outcomes, the numerical results of this research are shown in terms of load-ovalization curves and deformed shapes. The numerical values of both solutions are considered at the end of the loading process (e.g., end of the curves provided by the references).

Due to mesh size and the element type, sixteen different simulations have been performed. The load-ovalization curves obtained from the simulations are presented for all the element types and density sizes of the meshes. These will be compared to the literature research by overlapping the graphs, afterwards the results will be discussed and evaluated. The graphs from the literature are made of black lines and they follow these criteria:

- ▲ Experimental Investigations, Compression Load, EX-odd number
- Numerical Simulations, Compression Load, EX-odd number
- △ Experimental Investigations, Tension Load, EX-even number

☒ Numerical Simulations, Tension Load, EX-even number

When the results of this work will be presented no specification will be made in between the compression and tension specimens, since each specimen has the same trend to the respective reference case, i.e., the compression case of this research will overlap the reference cases, and so for the tension cases.

The graphs have as X-axis the ovalization that refers to the deformation of the chord cross-section at the center of the T-joint, which is calculated by subtracting a reference point at the chord bottom from average of the points in the brace; whereas the Y-axis, instead, represents the load applied at the brace tip, obtained by the opposite of the reaction force at the same point. Each of the following graphs will be shown with the curves of all the four types of density mesh that have been analyzed.

4.1. Curves With Automatic Step Sequence

In this section, the curves are represented in terms of the automatic step sequence. So far, a single step size is applied to the model through the constant step range, and all the four types of elements will be considered (S4R, S4, S8R, and S8R5). For what concerns the figures that will be described, these will represent respectively the Mises stress and PEEQ (Equivalent Plastic Strains) [51] of the specimens.

4.1.1. S4R Element Type

The graphs reported in Figure 5 represent the simulations done for meshes using the S4R element type (that are those given by default from the program), with an automatic step range. It is remarked that the lower curve for each graph refers to the compression specimens (i.e., EX-01 to EX-11 with odd numbers), whereas the higher one represents the tension specimens (i.e., EX-02 to EX-12 with even numbers).

Generally, for all the graphs it is easy to see a good fitting between the reference curves and the present work, especially for the unreinforced cases and for the coarse mesh of collar plate EX-03 and EX-04. The coarse mesh of EX-01, EX-02, EX-03, and EX-04 are depicted in Figure 6a–d.

Unreinforced cases show an inferior maximum stress but are distributed in almost all the chord, whereas the case of collar reinforced plate is characterized by higher maximum value but concentrated in the reinforcement. It is obvious that unreinforced cases have higher values in terms of plastic deformations with respect to the reinforced ones.

The above good fitting is not relatively the case of EX-06, where the present curves are slightly below the reference curves, the marked difference is also influenced by the fact that this is the thicker case, which causes higher values. However, this difference is repeated for all the element types with improvements in S8R, so further discussions are left when the results for these elements will be discussed.

From the curves can be seen two irregular trends, one is the temporary variation in the force values such as for the EX-10, EX-12 with the coarse mesh and slightly in EX-07 and EX-08 with the article mesh; and the second trend is the change in direction of the ovalization (where can be seen a turning back of the curves) such as for fine mesh of EX-01, EX-02, EX-04, EX-06, and EX-08. The first trend is not a model problem but is a consequence of the plasticity of the elements, so it is more related to the FE implementation than the actual modeling, in any case this happens after the maximum ovalization of the reference papers is reached. In addition, this behavior does not affect the specimens in compression. Contrastingly, the second trend is due to the fact that a small part of a corner of a quarter's brace rises in an unexpected way, as shown in Figure 7b for the fine mesh of the specimen EX-08. It is remarked that this behavior occurs just in the fine mesh, and this might be caused by the fragility of the mesh type (in fact, that does not occur in the S8R, which is the stronger).

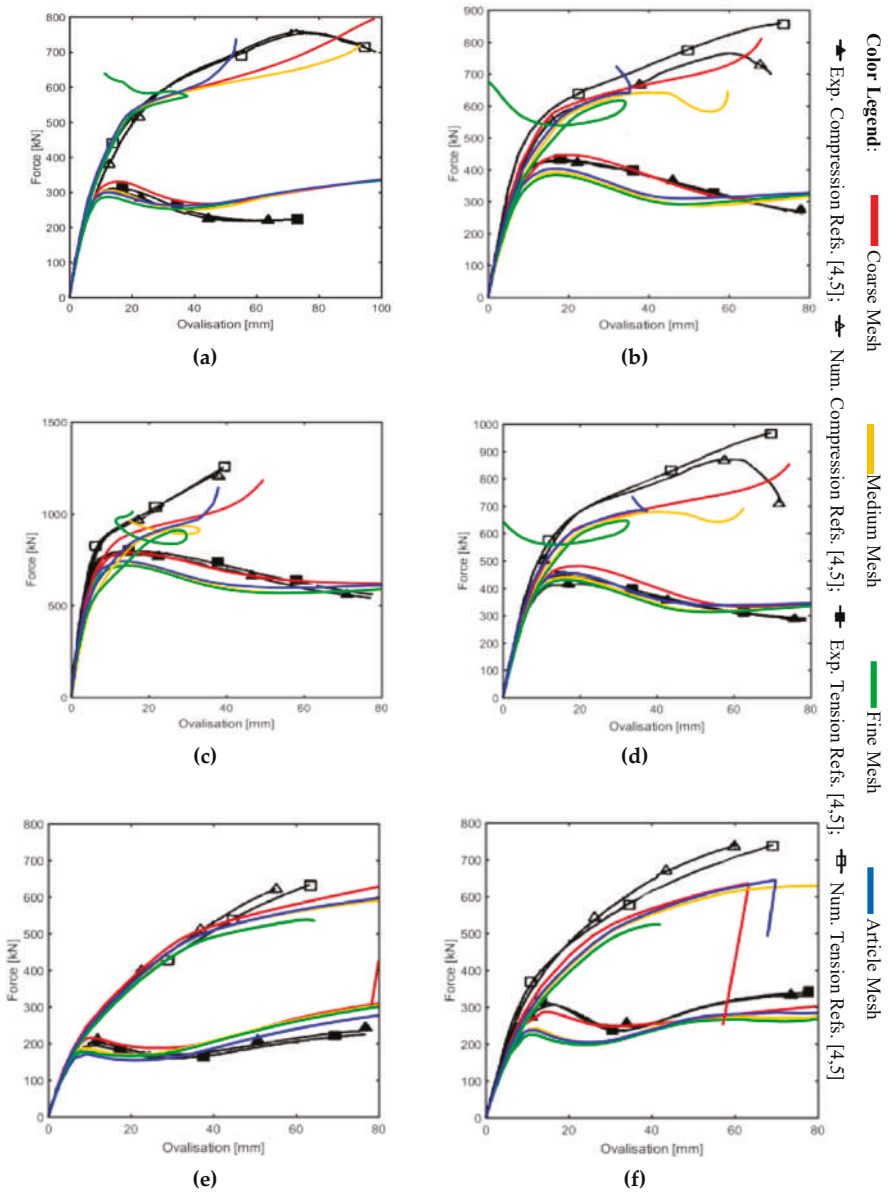


Figure 5. Load-Ovalization curves with S4R element type: (a) Unreinforced Ex-01-02, (b) Collar Plate Ex-03-04, (c) Collar Plate Ex-05-06, (d) Doubler Plate Ex-07-08, (e) Unreinforced Ex-09-10, and (f) Doubler Plate Ex-11-12.

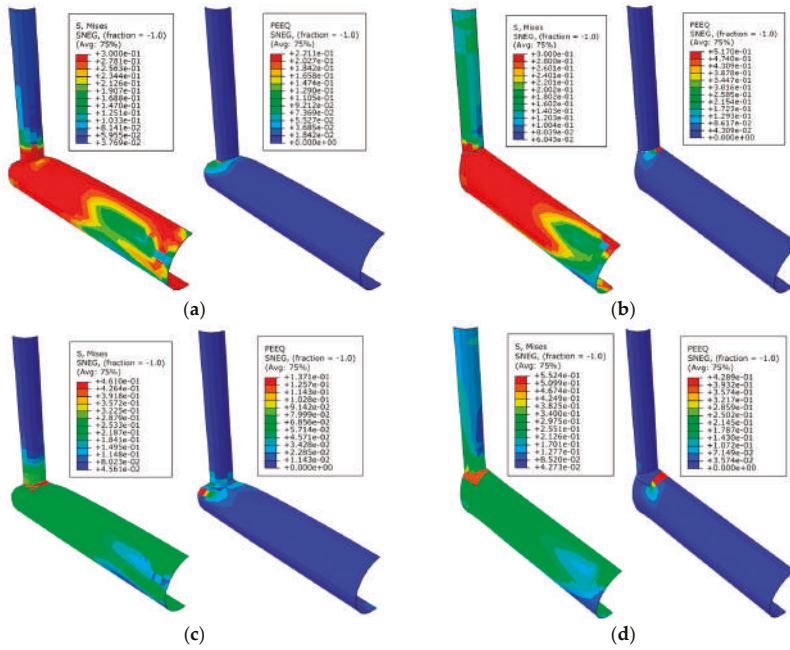


Figure 6. Mises stress and PEEQ representations: (a) Unreinforced Ex-01, (b) Unreinforced Ex-02, (c) Collar Plate Ex-03, and (d) Collar Plate Ex-04.

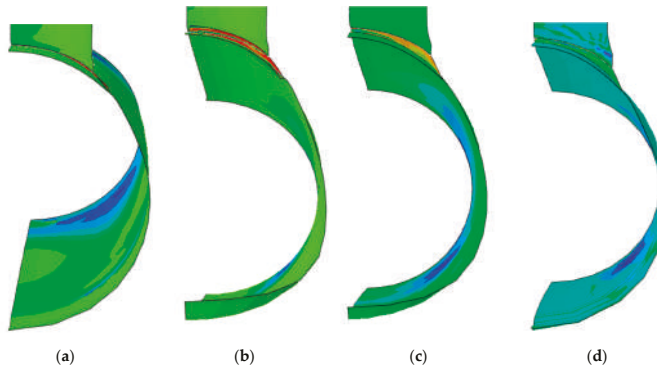


Figure 7. Ovalization change in fine mesh of Ex-08: (a) before the corner rise, (b) corner rise with S4R, (c) corner rise with S4, and (d) no corner rise SSR.

4.1.2. S4 Element Type

The major difference between the S4 element type and the previous, the S4R, is that in S4 elements no reduced integration is excepted. This similarity between the S4 and S4R is directly reflected by the results of the load-ovalization curves depicted in Figure 8, from which can be seen there are no big changes from the load-ovalization curves in Figure 5.

Relevant differences can be observed for fine meshes. In the tension cases EX-04 and EX-08 shown in Figure 8b,d, the “hook” is no longer present at the tail of each curve. Moreover, another improvement can be seen in EX-06 in Figure 8c where the reverse curve trend in terms of ovalization is

avoided for the medium mesh. While this remains in the fine mesh, such behavior as aforementioned is due to the rise of a part of the chord and this effect is depicted in Figure 7c.

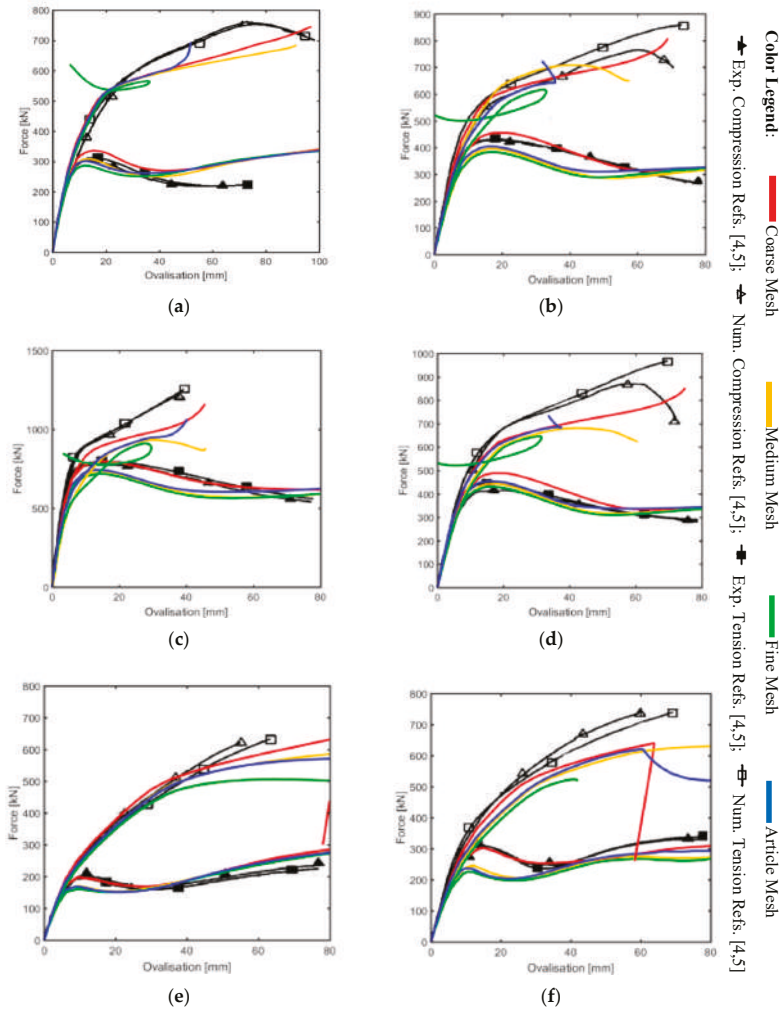


Figure 8. Load-Ovalization curves with S4 element type: (a) Unreinforced Ex-01-02, (b) Collar Plate Ex-03-04, (c) Collar Plate Ex-05-06, (d) Doubler Plate Ex-07-08, (e) Unreinforced Ex-09-10, and (f) Doubler Plate Ex-11-12.

4.1.3. S8R Element Type

In Figure 9 the S8R element is considered. With this type of element, the problem of the drop-in force (due to model exceeding plasticization at the end of the process) of the two previous cases is avoided. But several simulations end before the maximum ovalization (around 80 mm in the references) is reached, especially in the unreinforced case such as the article and coarse mesh of the specimen EX-01, the article mesh of specimen EX-03, and medium and fine mesh of the specimen EX-10.

In the case of the EX-06, that is the one that defers more from the references, but with the S8R element type the differences are reduced. The article mesh solution in Figure 9c has still a different shape with respect to the references but the curves coincide at their ends.

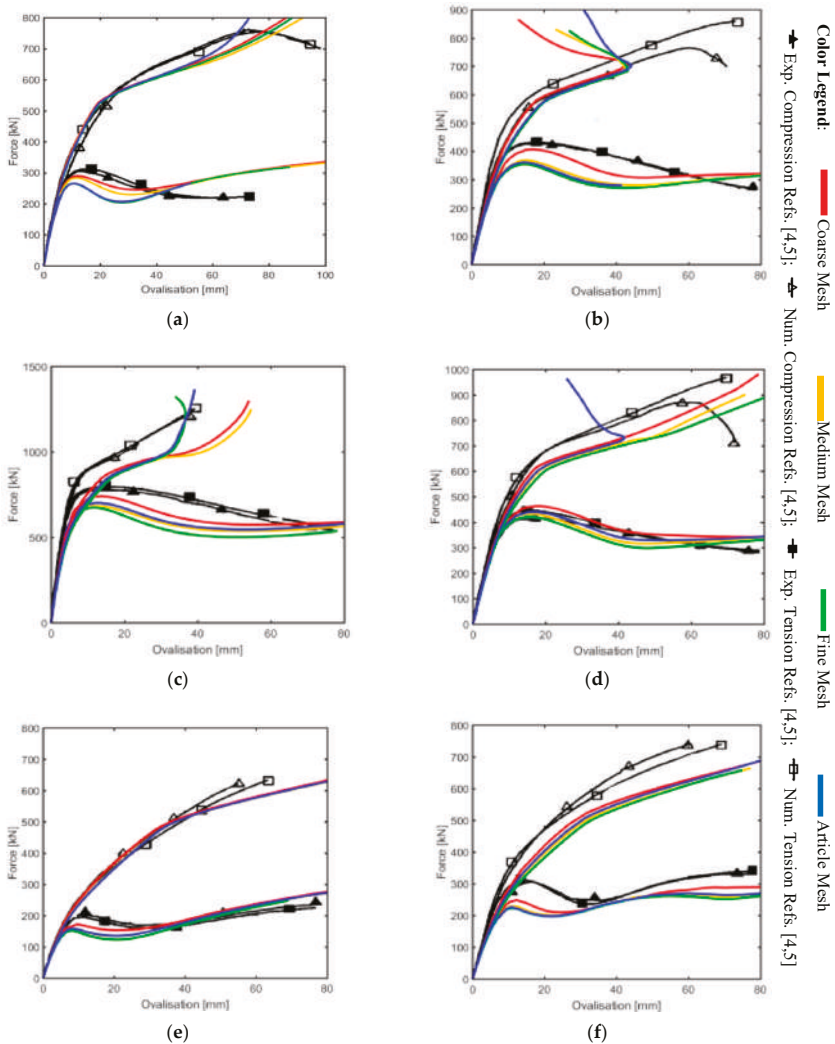


Figure 9. Load-Ovalization curves with S8R element type: (a) Unreinforced Ex-01-02, (b) Collar Plate Ex-03-04, (c) Collar Plate Ex-05-06, (d) Doubler Plate Ex-07-08, (e) Unreinforced Ex-09-10, and (f) Doubler Plate Ex-11-12.

As results in the EX-06 and EX-07 the smaller stress and plasticization can be seen, this is due to the increase in thickness of all the elements, which almost doubled with respect to the other cases. In addition, to this first improvement, for the specimen EX-08 using the S8R element, in the fine mesh the change in direction of the ovalization is also avoided. See Figure 7d where at the end of the simulation no rise of the corner part is present.

4.1.4. S8R5 Element Type

The last element type considered in this research is the S8R5 element type. The S8R5 has just five DOF, this means that there is a simplification respect to the S8R, and this simplification results in the inability to submit all the simulations. The load-ovalization curves of S8R element type depicted in Figure 9 are very close in shape to those of S8R5 reported in Figure 10, but an important issue is solved definitely and no reverse in ovalization is present for all the cases. To notice that was not possible to complete all the simulations because of the complexity of the S8R5 elements type, which does not always allow finding the convergence.

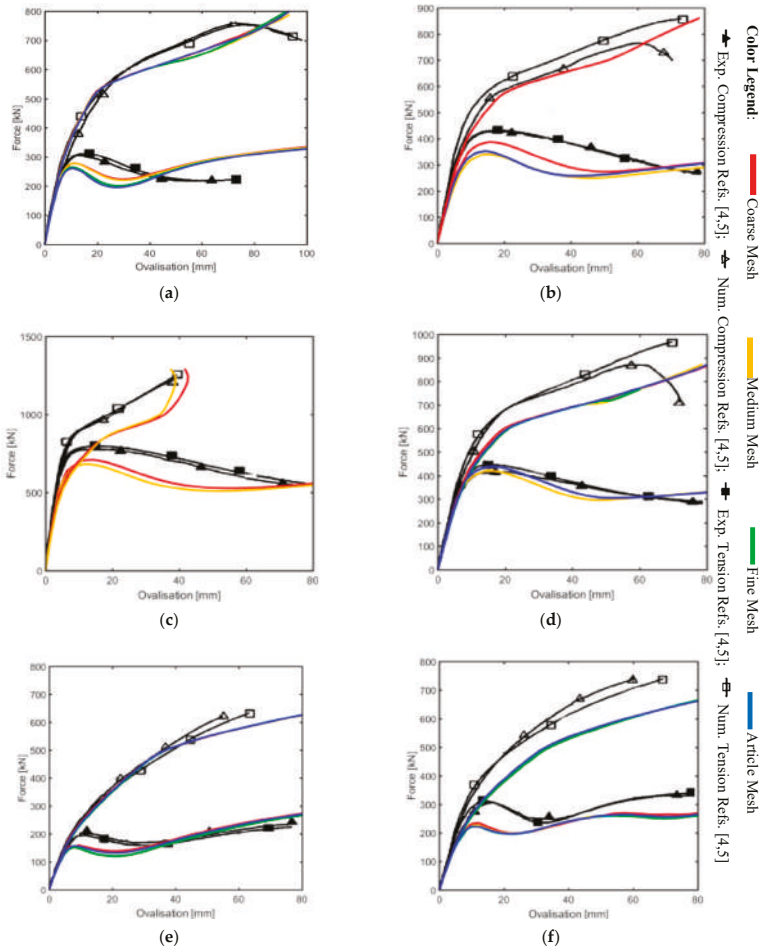


Figure 10. Load-Ovalization curves with S8R5 element type: (a) Unreinforced Ex-01-02, (b) Collar Plate Ex-03-04, (c) Collar Plate Ex-05-06, (d) Doubler Plate Ex-07-08, (e) Unreinforced Ex-09-10, and (f) Doubler Plate Ex-11-1.

4.2. Curves With Fixed Step Sequence

The plasticization of the T-joint is a key point for the fixed step sequence, since the starting point of the plasticization defines the application of the second step range. From the results of the simulations of EX-01 and EX-02 of the automatic step sequence, the starting period of the plastic behavior of the

material of the T-joint is identified. The set of all these values for the two specimens EX-01 and EX-02 are reported in Table 5, which shows that the plasticization starts at the very early stage of the simulations.

So fixed step sequence introduces one more step respect to the automatic one, as in the experimental investigation. For this reason, the simulations have been done for the first two specimens EX-01 and EX-02 as reported for all the four-element type in Figure 11, and once it emerged that no relevant changes in the results are present, it was understood that for this type of model the range application of the load/displacement makes no differences.

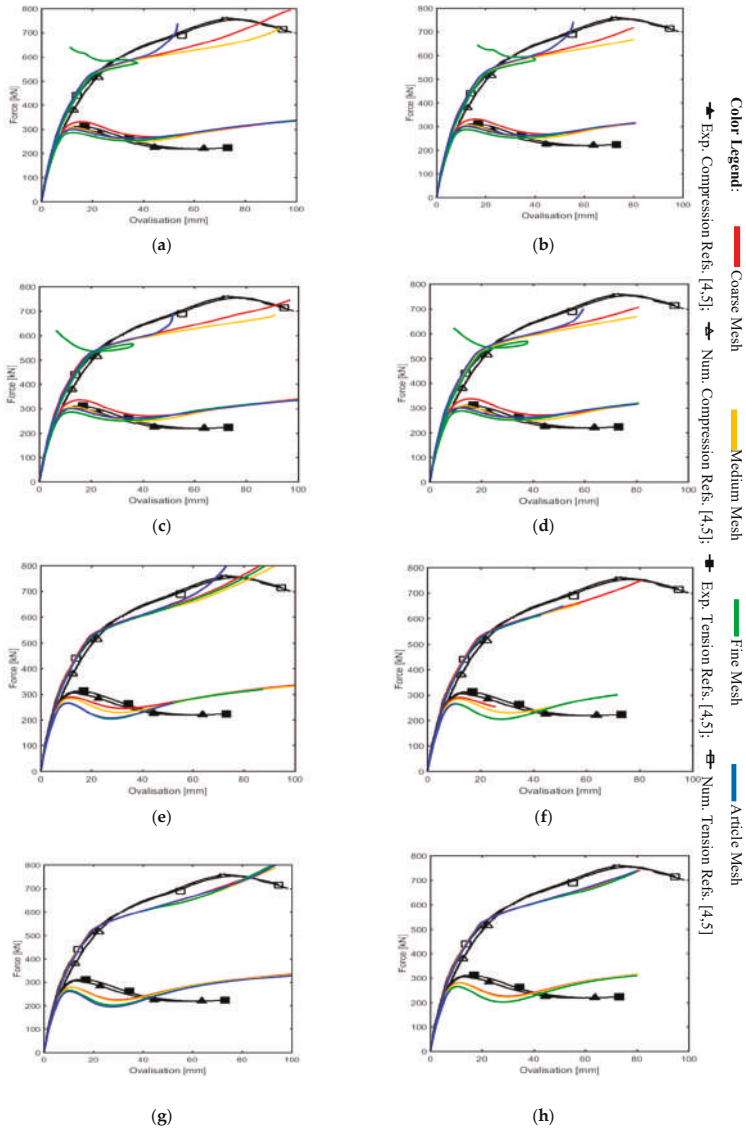


Figure 11. Load-Ovalization curves unreinforced Ex-01 and Ex-02: (a) automatic step S4R, (b) fixed step S4R, (c) automatic step S4, (d) fixed step S4, (e) automatic step S8R, (f) fixed step S8R, (g) automatic step S8R5, and (h) fixed step S8R5.

Table 5. Starting point of the plasticization for Ex-01 and Ex-02 [17].

Element Type	Mesh EX-01 and Ex-02	Density Mesh	Starting Point of Plastic Behavior
S4R		Coarse	0.009
		Medium	0.009
		Fine	0.009
		Article	0.009
S4		Coarse	0.009
		Medium	0.009
		Fine	0.009
		Article	0.009
S8R		Coarse	0.009
		Medium	0.006
		Fine	0.006
		Article	0.006
S8R5		Coarse	0.009
		Medium	0.006
		Fine	0.006
		Article	0.006

4.3. Deformed Shapes

Other comparisons between the present research and the references [4,5] are discussed in this section. Through considering sections or rings of the tubular elements, from which it is possible to observe the ovalization and associated yield hinges, as well as the separation between the chord and doubler/collar plate.

In the experimental investigation and the numerical simulation [4,5], after the tests were completed, for some of the specimens, sections or “rings” were obtained from the chord and brace. The results have been presented firstly for the specimens with diameter ratio (where $\beta = d_1/d_0$), i.e., from the EX-01 to EX-08, and then for the specimens with $\beta = 0.28$, i.e., from the EX-09 to EX-12. Alternatively, in the numerical simulation of van der Vegte et al. [5] the deformed rings, which have been showed, are just some that have the diameter ratio $\beta = 0.54$. Therefore, some gaps can be seen in the representation of the rings for what concern to the reference [4,5].

In the following the ovalization shapes will be shown, compared with the papers’ results, where these are present. The same experimental subdivision will be considered. The research simulations exceed the length of this paper’s simulation in most cases, whereby in the section will be taken from the same ovalization as literature cases. In addition, in this paper for further investigations of the shapes will be selected the ones that have the best fit in the load-ovalization curves.

4.3.1. Failure of the Specimens with $\beta = 0.54$ under Compression

Specimens under compression in the brace element with diameter ratio equal to 0.54 are EX-01, EX-03, EX-05, and EX-07. These are all represented in the experimental investigation, whereas in the numerical simulation reference to EX-05 is missing.

Specimen EX-01

Figure 12a,b shows the overall view of the unreinforced specimens of the Experimental Case (EC) (reference figures from [4,5]) and the Research Case (RC) (the present simulations). The present contour plots represent the MISES stresses.

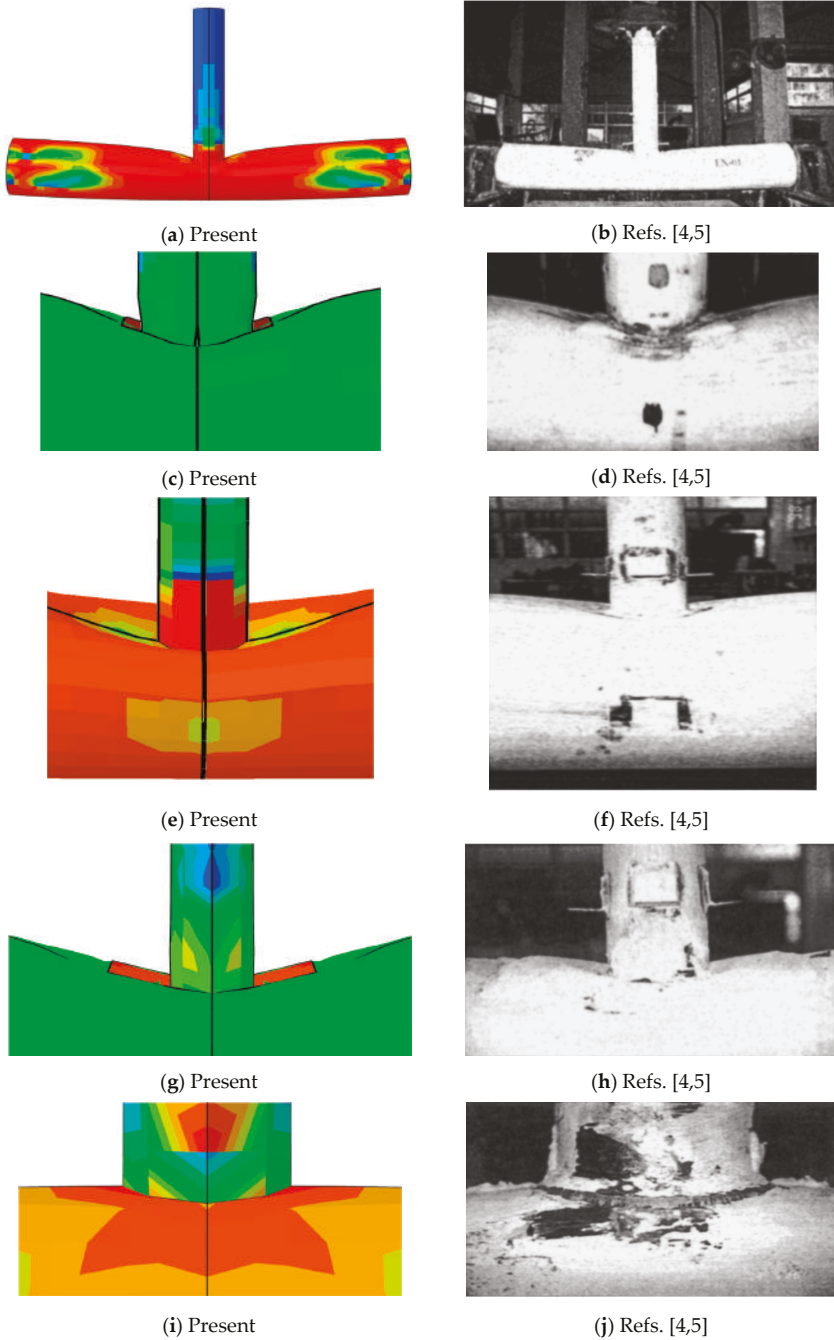


Figure 12. Overall and detail views: (a) Overall view Ex-01 RC, (b) Overall view Ex-01 EC, (c) Detail view Ex-05 RC, (d) Detail view Ex-05 EC, (e) Detail view Ex-09 RC, (f) Detail view Ex-09 EC, (g) Detail view Ex-11 RC, (h) Detail view Ex-11 EC, (i) Detail view Ex-10 RC, and (j) Detail view Ex-10 EC. (With permission from ASCE)

Figure 13a–c shows the sliced ring (chord and short portion of brace) from specimen EX-01, and here, different from the overall view, the case of Numerical Case (NC) (FE simulation from the references [4,5]) is also present. From the paper’s results can be seen the two yield hinges adjacent to brace-chord intersection become clear, while in the research case, however, this cannot be seen and the shape does not follow the same trend. As aforementioned the step taken is at ovalization 100 mm, which corresponds to the period 0.672 of 1 Abaqus simulation time period.

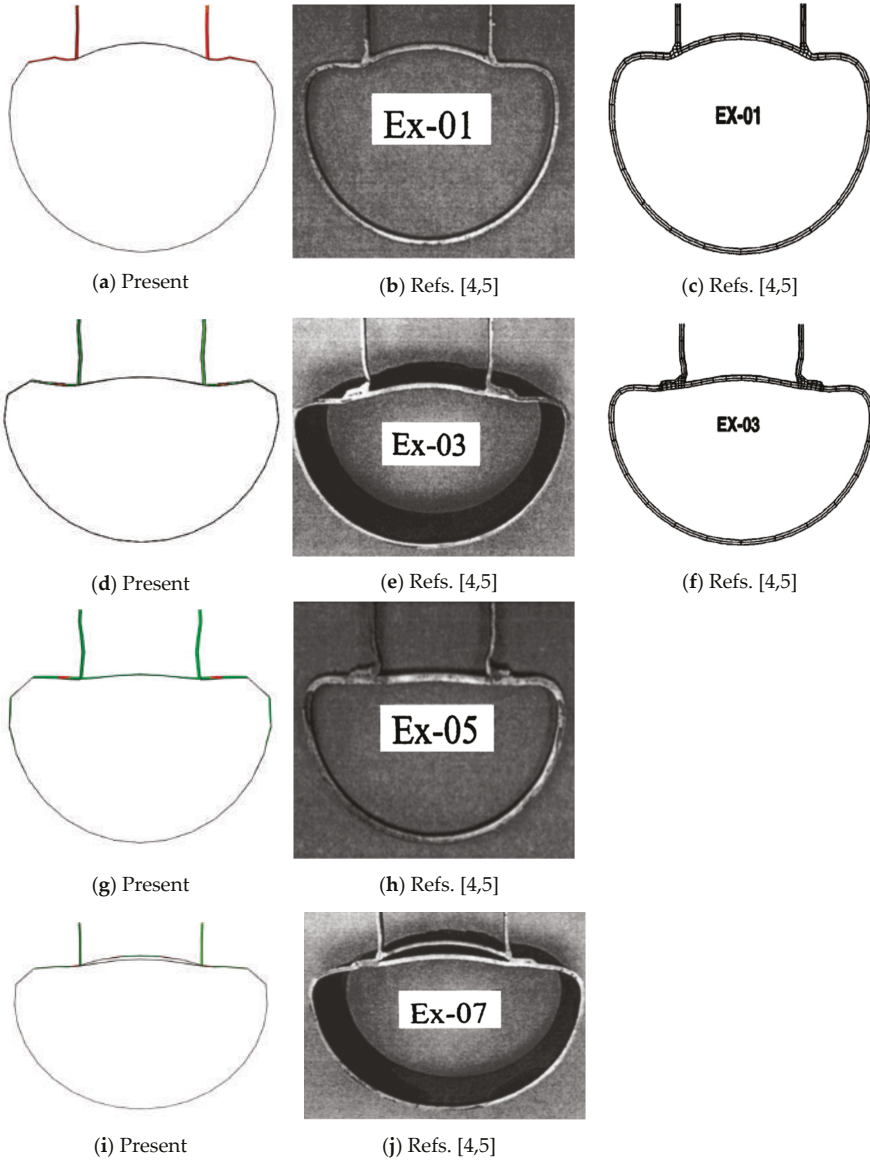


Figure 13. Cont.



Figure 13. Sliced rings of specimens subjected to compression with $\beta = 0.54$: (a) Ex-01 RC, (b) Ex-01 EC, (c) Ex-01 NC, (d) Ex-03 RC, (e) Ex-03 EC, (f) Ex-03 NC, (g) Ex-05 RC, (h) Ex-05 EC, (i) Ex-07 RC, (j) Ex-07EC, (k) particular Ex-07 RC, and (l) particular Ex-07 EC. (With permission from ASCE)

Specimen EX-03

For the specimen EX-03 the papers presented only the sliced result. Figure 13d–f shows the sliced ring of specimen EX-03. Between this specimen and the previous one it can be immediately noticed the significant strength enhancement offered by the collar reinforcement to the chord section for EX-03. The step taken here is at ovalization 80 mm, which corresponds to the period 0.476 of 1 Abaqus simulation time period.

Specimen EX-05

Figure 12c,d shows the detail of the chord indentation side view of the reinforced specimen EX-05; also, here the work case is showed in form of MISES stress, where plastic deformation is near the intersection chord-brace, whereas the chord bottom part remained relatively straight with no deformation and no stress concentration. Figure 13g,h shows the sliced ring from specimen EX-05, here the NC was not available in the results. The bending in this case is more severe than that of specimen EX-03, some results of the relatively higher strength of the chord, as can be seen in load-ovalization curves. Ovalization 80 mm corresponds to the period 0.614 of 1 Abaqus simulation time period.

Specimen EX-07

As far as EX-07 is concerned, the papers presented only the sliced result, as depicted in Figure 13i,j. The separation from the chord outer surface of the doubler plate (which at the original shape fits the chord perfectly) can be observed. As can be seen in Figure 13k,l, RC **also** has this effect but with no such emphasis as in the papers’ cases. This behavior is due to the fact while the brace compresses the chord, the wall of the latter has a different rotation with respect to the reinforcement; in the FE model the modeling of the contact and ties have played a fundamental role. In this the ovalization 80 mm corresponds to the period 0.531 of 1 Abaqus simulation time period.

4.3.2. Failure of the Specimens with $\beta = 0.54$ under Tension

In the following, the specimens under tension in the brace element with diameter ratio equal to 0.54 will be considered. These specimens are EX-02, EX-04, EX-06, and EX-08. Here the experimental investigation results are given for EX-04, EX-06, and EX-08, while in the numerical simulation just the EX-08 is given.

During the experimental test, some specimens buckle such as EX-02 and EX-04; while for the numerical simulations the buckling was not taken into account. Also, in the present research, the buckling is not covered, but is left as future development.

Specimens with Buckling EX-02, EX-04, and EX-08

Even if in this research the buckling is not taken into account, due to the initial purpose which is that of building a reliable model made of shell elements, a good match has been found in the load-ovalization curves as can be seen also here in the deformed shapes of the specimen where the

buckling occurred in the physical experiment [4]. However, the buckling was also not considered in the previous numerical simulation [5], and the results in terms of deformed shape from the numerical simulation were not provided.

EX-02, EX-04, and 08 are the three cases where the specimens buckle. The doubler plate specimen EX-08 subjected to brace tension has a similar pattern to the EX-04, with pronounced chord plasticization. In Figure 14a–c the separation of the doubler plate from the chord at the brace-doubler intersection is illustrated. This separation can be seen both in the reinforced and unreinforced case, also without considering the buckling effect.

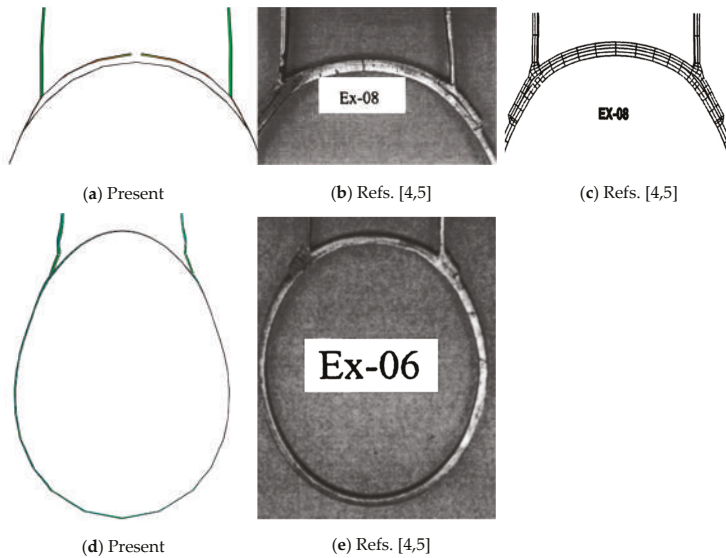


Figure 14. Sliced rings of specimens subjected to tension with $\beta = 0.54$: (a) Ex-08 RC, (b) Ex-08 EC, (c) Ex-08 NC, (d) Ex-06 RC, and (e) Ex-06 EC. (With permission from ASCE)

Specimen EX-06

EX-06 is the thicker specimen with collar reinforcement subjected to brace tension. Its deformed shape is shown in Figure 14d,e. For this specimen the experimental test was terminated after the tensile capacity of the actuator was reached at 1200 kN, in RC the simulation also stops earlier, and at the end of time period 1 the ovalization is equal to 38 mm instead of 80 mm in the references [4,5].

4.3.3. Failure of the Specimens with $\beta = 0.28$ under Compression

In the following specimens under compression with $\beta = 0.28$ are shown, and this is the case of EX-09 and EX-11. For both cases the NC does not show any result, so they will be compared only for the EC with the present research.

Specimen EX-09

Figure 12e,f shows the localized indentation of the chord of unreinforced specimen EX-09 subjected to compression, which has a similar behavior of the respective specimen with higher diameter ratio EX-01. For the sake of comparison, Figure 15a,b presents its sliced ring. The step taken here is at ovalization 80 mm, which corresponds to the period 0.450 of 1 Abaqus simulation time period.

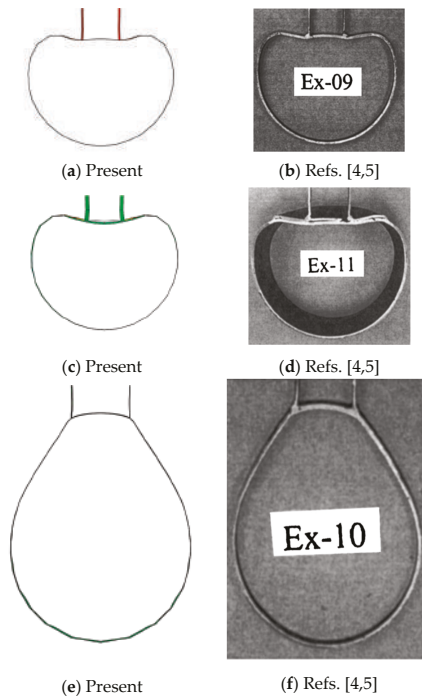


Figure 15. Sliced rings of specimens subjected to compression/tension with $\beta = 0.28$: (a) Ex-09 RC, (b) Ex-09 EC, (c) Ex-11 RC and (d) Ex-11 EC, (e) Ex-10 RC, and (f) Ex-10 EC. (With permission from ASCE)

Specimen EX-11

Figure 12g,h shows the localized indentation of the chord of the reinforced specimen EX-11 subjected to compression; besides the appreciable indentation at the intersection area, the doubler plate is observed to bulge out of its plane. Contrastingly, Figure 15c,d presents its sliced ring. The step taken here is at ovalization 80 mm, which corresponds to the period 0.537 of 1 Abaqus simulation time period.

4.3.4. Failure of the Specimens with $\beta = 0.28$ under Tension

In the following the last two specimens examined are EX-10 and EX-12, with small ratio but subjected to tension. Only EX-10 will be showed here, since EX-12 in the experimental investigation was stopped due to brittle failure that occurred through punching shear fracture of the brace out of the doubler plate.

Specimen EX-10

Figure 12i,j shows a detailed view of the brace-chord intersection of the unreinforced specimen EX-10 subjected to brace tension; also, after severe plasticization, the joint exhibited brittle shear failure of the chord wall at one side of the intersection. In the EC the focus is at the weld zone that is not present in the RC. Alternatively, Figure 15e,f presents its sliced rings, which shows very similar shapes. The time step taken here is at ovalization 80 mm, for a period 0.443 of 1 Abaqus simulation time period.

5. Summary and Conclusions

The FE analyses with the use of shell elements in this research have been directed to simulate the static behavior of a set of 12 unreinforced and reinforced test cases, on uniplanar T-joints under axial brace load carried out by Choo et al. [4]. In addition to the investigation conducted by Choo et al. [4], the numerical simulation of van der Vegte et al. [5] has been taken into account. Even though a FE study is already present, there the authors have decided to use the more computationally expensive 3-D model made by solid elements. The present research tries to solve the issues faced in [5] and sheds light on the importance of the mechanical data in FE modeling. Some peculiar data that are missing in the reference papers were discussed.

The results are presented in terms of restraining force versus ovalization of the chord under the applied force and also in terms of deformed shapes, by considering sections or rings of the tubular elements. Based on the results presented in the previous sections, where several parametric settings have been considered, the following conclusions and considerations can be made.

- The difference in terms of load application does not affect the results in relevant way, since the results obtained by the automatic step sequence (i.e., unique stroke range) and those obtained by the fixed step sequence (i.e., two stroke ranges as in the experimental investigation) for the first two specimens are almost the same, except in some cases of the fixed step where it was not possible to find the convergence for all, due to the complexity caused by the double step. Therefore, the automatic step sequence was considered for the remaining samples that besides being simpler also allows an easier convergence.
- Automatic step sequence and the true stress-strain relationship without hardening after the peak load were considered. For these settings, four different mesh densities (coarse, medium, fine, and article) each one analyzed with four-element types (S4R, S4, S8R, and S8R5) were analyzed, respectively. Generally, it was possible to see that all load-ovalization curves fit quite well in the initial (linear) part with the reference investigation, and then go slightly below in the post-peak, and finally to converge almost in final value. In the first group of element types, i.e., S4R and S4, it can be seen that there is an abnormal shape of the curves, with the reverse of the ovalization, when the elements size of the mesh used are relatively small such as in the medium and fine mesh. This is valid when $\beta = 0.54$, i.e., the diameter of the brace is more than half of the chord one. While if this ratio is decreased to $\beta = 0.28$ this does not occur. In contrast, the second group of element types with a higher number of nodes solves the issue of the change in direction of the ovalization for all the cases, even though a higher number of nodes leads to no convergence for some specimens.
- Due to the fact that the automatic step sequences, with no hardening simulations, have the relevant and complete data, these were compared to the references by cutting rings from the center of the chord of each specimen. The ring of the research shows a perfect matching to the experimental case under compression. In the research study, as in the numerical reference, the buckling that occurs in some of the tension cases of the experimental research was not considered. However, the shapes obtained by this research kept good accordance, even in the specimens where buckling occurred.
- Although the reliability of shell elements is the object of this research, a 3-D model with the same setting used by van der Vegte et al. [5] was built to verify the reliability of the preliminary parameters considered in the model with those of the numerical simulation [5], since assumptions were done in the first stage due to lack in the data in the reference papers. From the results of the 3-D model of this study, as depicted in Figure 16a, the load-ovalization curves in Figure 16b have been obtained where almost similar shapes and characteristics of the main model made by shells with S4 element type can be seen. Thus, it is possible to deduce that some relevant data are missing in the paper.
- The model considered in this research is able to show comparable strength characteristics as in [4,5]. In fact, the T-joints considered in this study show a great improvement in terms of strength of the specimen reinforced by doubler plate or a collar plate as compared to the strength

of the unreinforced joints. An enhancement of almost 40% was reached for $\beta = 0.54$ as in the experimental case, but a smaller value was found for $\beta = 0.28$ where the research value is five per cent smaller than the experimental one of sixteen percent. Therefore, it can be said that the two types of reinforcement have the capacity to distribute the brace axial load to a larger region of the chord, with consequent improvement in terms of strength enhancement.

- Through the use of shell elements instead of the more expensive (in terms of computational cost) solid elements, the contact problem and the introduction of the element thickness have been solved. It turned out that shell elements with 8 nodes and reduced integration are suitable for this type of structures; this type of elements gives a reliable solution already starting from coarse meshes. Whereas the S4R elements type given by default from the software gives less precise results.
- The missing data in the reference papers have inevitably lead to some differences in the results, partially solved by the use of a different true stress-strain relationship. However, due to the good agreement between the research and the experimental results, the former can be developed through parametric studies to extend the above considerations to different types of joints. Moreover, the present research can be considered for studies involving composite materials as reinforcing phase for damaged or weak joints.

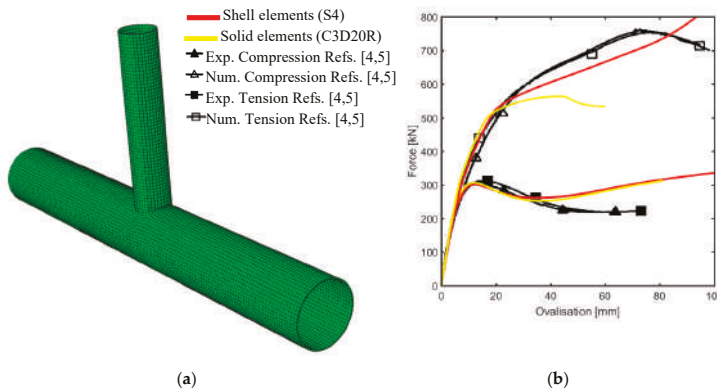


Figure 16. Three-Dimensional model C3D20R: (a) medium mesh global view and (b) Load-Ovalization curves, shell, and solid elements comparison using for both medium meshes (size 20).

6. Future Developments

The authors analyzed, in the first instance, T-joints with shell elements. Since small deviations have been noticed, solid elements models have been generated to test the same joints as in [5]. However, the following conclusions are drawn to a future development of the present paper, which will consider a deep analysis of the mechanical properties used in the experimental testing. As a matter of fact, as a preliminary study the solid models are comparable to the shell ones by considering the same input data.

The differences between the reference studies [4,5] and the present ones are in the “large deformation” part of the curves. The linear elastic branch is so small that it cannot be seen in the plots, but it is very clear that the curves have two segments, and both are nonlinear.

Due to this change, which seemed to be a consequence of the previous assumption done for the material properties, where the true stress-true strain relationship was taken as elastic-perfectly plastic model reported in Figure 2a. Hence, it has been decided to introduce a hardening of 10% in the true stress-strain relationship for the first two specimens as reported in Figure 2b, differently to what was written in the reference paper [5].

The outcome of this setting, as depicted in Figure 17, gives for the tension cases a very close match of the curves for almost 90% of each simulation, while in compression some differences can still be noted. True strain-stress relationship closer to the real behavior of the steel material (left to future studies) can solve this last deference.

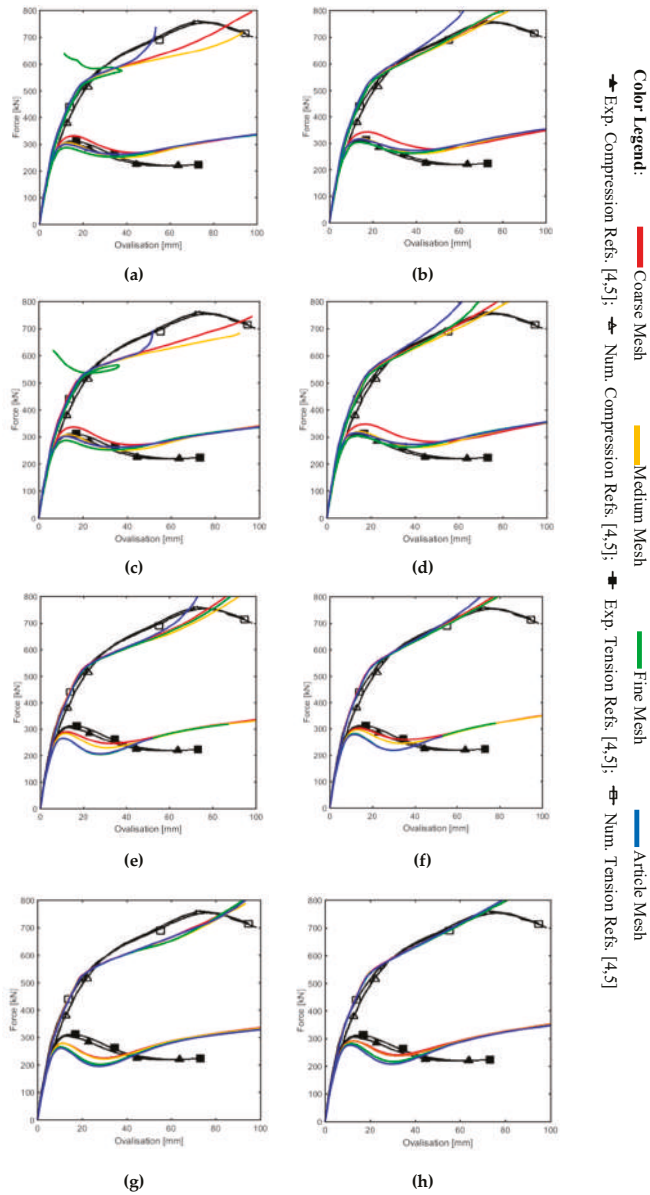


Figure 17. Load-Ovalization curves unreinforced Ex-01 and Ex-02 with 10% hardening: (a) S4R without hardening, (b) S4R with hardening, (c) S4 without hardening, (d) S4 with hardening, (e) S8R without hardening, (f) S8R with hardening, (g) S8R5 without hardening, and (h) S8R5 with hardening.

Author Contributions: S.O. and N.F. conceived and designed the experiments; S.O. performed the experiments; S.O. and N.F. analyzed the data; S.O. and N.F. contributed reagents/materials/analysis tools; S.O. and N.F. wrote and review the paper.

Acknowledgments: The authors acknowledge “Fondazione Flaminia” (Ravenna, Italy) for supporting the present research.

Conflicts of Interest: The authors declare no conflict of interest.

References

1. Moffat, D.G.; Kruzelecki, J.; Blachut, J. The effects of chord length and boundary conditions on the static strength of a tubular T-joint under brace compression loading. *Mar. Struct.* **1996**, *9*, 935–947. [[CrossRef](#)]
2. Choo, Y.S.; Qian, X.D.; Foo, K.S. Static strength variation of thick-walled CHS X-joints with different included angles and chord stress levels. *Mar. Struct.* **2004**, *17*, 311–324. [[CrossRef](#)]
3. Lee, M.M.K.; Llewelyn-Parry, A. Strength prediction for ring-stiffened DT-joints in offshore jacket structures. *Eng. Struct.* **2005**, *27*, 421–430. [[CrossRef](#)]
4. Choo, Y.S.; van der Vegte, G.J.; Zettlemoyer, N.; Li, B.H.; Liew, J.Y.R. Static strength of T-joints reinforced with doubler or collar plates. I: Experimental investigations. *J. Struct. Eng.* **2005**, *131*, 119–128. [[CrossRef](#)]
5. van der Vegte, G.J.; Choo, Y.S.; Liang, J.X.; Zettlemoyer, N.; Liew, J.Y.R. Static Strength of T-joints reinforced with doubler or collar plates. II: Numerical investigations. *J. Struct. Eng.* **2005**, *131*, 129–138. [[CrossRef](#)]
6. Yang, J.; Shao, Y.; Chen, C. Static strength of chord reinforced tubular Y-joints under axial loading. *Mar. Struct.* **2012**, *29*, 226–245. [[CrossRef](#)]
7. Ozyurt, E.; Wang, Y.C.; Tan, K.H. Elevated temperature resistance of welded tubular joints under axial load in the brace member. *Eng. Struct.* **2014**, *59*, 574–586. [[CrossRef](#)]
8. Chen, Y.; Feng, R.; Wang, C. Tests of steel and composite CHS X-joints with curved chord under axial compression. *Eng. Struct.* **2015**, *99*, 423–438. [[CrossRef](#)]
9. Lie, S.T.; Li, T.; Shao, Y.B.; Vipin, S.P. Plastic collapse load prediction of cracked circular hollow section gap K-joints under in-plane bending. *Mar. Struct.* **2016**, *50*, 20–34. [[CrossRef](#)]
10. Qu, H.; Li, A.; Huo, J.; Liu, Y. Dynamic performance of collar plate reinforced tubular T-joint with precompression chord. *Eng. Struct.* **2017**, *141*, 555–570. [[CrossRef](#)]
11. Zhu, L.; Yang, K.; Bai, Y.; Sun, H.; Wang, M. Capacity of steel CHS X-joints strengthened with external stiffening rings in compression. *Thin-Walled Struct.* **2017**, *115*, 110–118. [[CrossRef](#)]
12. Đuričić, D.; Aleksić, S.; Šćepanović, B.; Lučić, D. Experimental, theoretical and numerical analysis of K-joint made of CHS aluminium profiles. *Thin-Walled Struct.* **2017**, *119*, 58–71. [[CrossRef](#)]
13. Lan, X.; Huang, Y.; Chan, T.-M.; Young, B. Static strength of stainless steel K- and N-joints at elevated temperatures. *Thin-Walled Struct.* **2018**, *122*, 501–509. [[CrossRef](#)]
14. Qu, S.; Wu, X.; Sun, Q. Experimental study and theoretical analysis on the ultimate strength of high-strength-steel tubular K-joints. *Thin-Walled Struct.* **2018**, *123*, 244–254. [[CrossRef](#)]
15. Li, X.; Zhang, L.; Xue, X.; Wang, X.; Wang, H. Prediction on ultimate strength of tube-gusset KT-joints stiffened by 1/4 ring plates through experimental and numerical study. *Thin-Walled Struct.* **2018**, *123*, 409–419. [[CrossRef](#)]
16. Feng, R.; Chen, Y.; Wei, J.; He, K.; Fu, L. Behaviour of grouted stainless-steel tubular X-joints with CHS chord under axial compression. *Thin-Walled Struct.* **2018**, *124*, 323–342. [[CrossRef](#)]
17. Ouakka, S. On the Static Strength of Reinforce Joints. Master’s Thesis, University of Bologna, Bologna, Italy, 2017.
18. Lotsberg, I. On stress concentration factors for tubular Y- and T-Joints in frame structures. *Mar. Struct.* **2011**, *24*, 60–69. [[CrossRef](#)]
19. Osawa, N.; Yamamoto, N.; Fukuoka, T.; Sawamura, J.; Nagai, H.; Maeda, S. Study on the preciseness of hot spot stress of web-stiffened cruciform welded joints derived from shell finite element analyses. *Mar. Struct.* **2011**, *24*, 207–238. [[CrossRef](#)]
20. Lotfollahi-Yaghin, M.A.; Ahmadi, H. Geometric stress distribution along the weld toe of the outer brace in two-planar tubular DKT-joints: Parametric study and deriving the SCF design equations. *Mar. Struct.* **2011**, *24*, 239–260. [[CrossRef](#)]
21. Cheng, B.; Qian, Q.; Zhao, X.-L. Stress concentration factors and fatigue behavior of square bird-beak SHS T-joints under out-of-plane bending. *Eng. Struct.* **2015**, *99*, 677–684. [[CrossRef](#)]

22. Pradana, M.R.; Qian, X.; Swaddiwudhipong, S. Simplified Effective Notch Stress calculation for non-overlapping circular hollow section K-joints. *Mar. Struct.* **2017**, *55*, 1–16. [CrossRef]
23. Cheng, B.; Li, C.; Lou, Y.; Zhao, X.-L. SCF of bird-beak SHS X-joints under asymmetrical brace axial forces. *Thin-Walled Struct.* **2018**, *123*, 57–69. [CrossRef]
24. Xia, J.; Chang, H.; Goldsworthy, H.; Bu, Y.; Lu, Y. Axial hysteretic behavior of doubler-plate reinforced square hollow section tubular T-joints. *Mar. Struct.* **2017**, *55*, 162–181. [CrossRef]
25. Gao, F.; Guo, X.-Z.; Long, X.-H.; Guan, X.-Q.; Zhu, H.-P. Hysteretic behaviour of SHS brace-H-shaped chord T-joints with transverse stiffeners. *Thin-Walled Struct.* **2018**, *122*, 387–402. [CrossRef]
26. Ahmadi, H.; Nejad, A.Z. Geometrical effects on the local joint flexibility of two-planar tubular DK-joints in jacket substructure of offshore wind turbines under OPB loading. *Thin-Walled Struct.* **2017**, *114*, 122–133. [CrossRef]
27. Tong, L.W.; Xu, G.W.; Yang, D.L.; Mashiri, F.R.; Zhao, X.L. Fatigue behavior and design of welded tubular T-joints with CHS brace and concrete-filled chord. *Thin-Walled Struct.* **2017**, *120*, 180–190. [CrossRef]
28. Dong, W.; Moan, T.; Gao, Z. Long-term fatigue analysis of multi-planar tubular joints for jacket-type offshore wind turbine in time domain. *Eng. Struct.* **2011**, *33*, 2002–2014. [CrossRef]
29. Jiang, W.Q.; Wang, Z.Q.; McClure, G.; Wang, G.L.; Geng, J.D. Accurate modeling of joint effects in lattice transmission towers. *Eng. Struct.* **2011**, *33*, 1817–1827. [CrossRef]
30. Cheng, S.; Becque, J. A design methodology for side wall failure of RHS truss X-joints accounting for compressive chord pre-load. *Eng. Struct.* **2016**, *126*, 689–702. [CrossRef]
31. Ahmed, A.; Qian, X. A toughness-based deformation limit for fatigue-cracked X-joints under in-plane bending. *Mar. Struct.* **2015**, *42*, 33–52. [CrossRef]
32. Liu, B.C. Experimental analysis of tubular joints using white light speckle method. *Mar. Struct.* **1995**, *8*, 81–91. [CrossRef]
33. Pey, L.P.; Soh, A.K.; Soh, C.K. Partial implementation of compatibility conditions in modeling tubular joints using brick and shell elements. *Finite Elem. Anal. Des.* **1995**, *20*, 127–138. [CrossRef]
34. Mackerle, J. Fastening and joining: Finite element and boundary element analyses—A bibliography (1992–1994). *Finite Elem. Anal. Des.* **1995**, *20*, 205–215. [CrossRef]
35. Mackerle, J. Fatigue analysis with finite and boundary element methods a bibliography (1993–1995). *Finite Elem. Anal. Des.* **1997**, *24*, 187–196. [CrossRef]
36. Wang, T.; Hopperstad, O.S.; Lademo, O.-G.; Larsen, P.K. Finite element analysis of welded beam-to-column joints in aluminium alloy EN AW 6082 T6. *Finite Elem. Anal. Des.* **2007**, *44*, 1–16. [CrossRef]
37. Lee, C.K.; Chiew, S.P.; Lie, S.T.; Nguyen, T.B.N. Adaptive mesh generation procedures for thin-walled tubular structures. *Finite Elem. Anal. Des.* **2010**, *46*, 114–131. [CrossRef]
38. Nicol, D.A.C. Creep behaviour of butt-welded joints. *Int. J. Eng. Sci.* **1985**, *23*, 541–553. [CrossRef]
39. Kolpakov, A.G. Influence of non-degenerated joint on the global and local behavior of joined plates. *Int. J. Eng. Sci.* **2011**, *49*, 1216–1231. [CrossRef]
40. Wu, X.-F.; Jenson, R.A. Stress-function variational method for stress analysis of bonded joints under mechanical and thermal loads. *Int. J. Eng. Sci.* **2011**, *49*, 279–294. [CrossRef]
41. Chowdhury, N.M.; Wang, J.; Chiu, W.K.; Chang, P. Static and fatigue testing bolted, bonded and hybrid step lap joints of thick carbon fibre/epoxy laminates used on aircraft structures. *Compos. Struct.* **2016**, *142*, 96–106. [CrossRef]
42. Shen, W.; Yan, R.; Luo, B.; Zhu, Y.; Zeng, H. Ultimate strength analysis of composite typical joints for ship structures. *Compos. Struct.* **2017**, *171*, 32–42. [CrossRef]
43. Pearce, G.M.; Tao, C.; Quek, Y.H.E.; Chowdhury, N.T. A modified Arcan test for mixed-mode loading of bolted joints in composite structures. *Compos. Struct.* **2018**, *187*, 203–211. [CrossRef]
44. Bigaud, J.; Aboura, Z.; Martins, A.T.; Verger, S. Analysis of the mechanical behavior of composite T-joints reinforced by one side stitching. *Compos. Struct.* **2018**, *184*, 249–255. [CrossRef]
45. Liu, F.; Lu, X.; Zhao, L.; Zhang, J.; Xu, J.; Hu, N. Investigation of bolt load redistribution and its effect on failure prediction in double-lap, multi-bolt composite joints. *Compos. Struct.* **2018**, *202*, 397–405. [CrossRef]
46. Liu, Y.; Lemanski, S.; Zhang, X. Parametric study of size, curvature and free edge effects on the predicted strength of bonded composite joints. *Compos. Struct.* **2018**, *202*, 364–373. [CrossRef]
47. API—American Petroleum Institute. Available online: <http://www.api.org/> (accessed on 17 February 2019).

48. ISO—International Organization for Standardization. Available online: <https://www.iso.org/> (accessed on 17 February 2019).
49. ABS—American Bureau of Shipping ABS. Available online: <https://ww2.eagle.org/en.html> (accessed on 17 February 2019).
50. Gardner, L.; Nethercot, D.A. *Guida all'Eurocodice 3. Progettazione di Edifici in Acciaio: EN 1993-1-1, -1-3 e -1-8*; EPC Editore: Roma, Italy, 2012. (In Italian)
51. Abaqus 6.14 Documentation: Abaqus/CAE User's Guide. Available online: <http://ivt-abaqusdoc.ivt.ntnu.no:2080/v6.14/books/usi/default.htm> (accessed on 17 February 2019).



© 2019 by the authors. Licensee MDPI, Basel, Switzerland. This article is an open access article distributed under the terms and conditions of the Creative Commons Attribution (CC BY) license (<http://creativecommons.org/licenses/by/4.0/>).

Article

A Complex Variable Solution for Lining Stress and Deformation in a Non-Circular Deep Tunnel II Practical Application and Verification

Yansong Li and Shougen Chen *

MOE Key Laboratory of Transportation Tunnel Engineering, Southwest Jiaotong University, Chengdu 610031, Sichuan, China; liyansong@my.swjtu.edu.cn

* Correspondence: shougenChen@163.com

Received: 1 July 2018; Accepted: 28 August 2018; Published: 30 August 2018

Abstract: A new complex variable method is presented for stress and displacement problems in a non-circular deep tunnel with certain given boundary conditions at infinity. In order to overcome the complex problems caused by non-circular geometric configurations and the multiply-connected region, a complex variable method and continuity boundary conditions are used to determine stress and displacement within the tunnel lining and within the surrounding rock. The coefficients in the conformal mapping function and stress functions are determined by the optimal design and complex variable method, respectively. The new method is validated by FLAC3D finite difference software through an example. Both the new method and the numerical simulation obtained similar results for the stress concentration and the minimum radial displacement occurred at a similar place in the tunnel. It is demonstrated that the new complex variable method is reliable and reasonable. The new method also provides another way to solve non-circular tunnel excavation problems in a faster and more accurate way.

Keywords: non-circular deep tunnel; complex variables; conformal mapping; elasticity; numerical simulation

1. Introduction

With the rapid economic development in China, which has caused the expansion of road and railway networks from east to west and to areas in the northeast that are surrounded by mountains, the construction of tunnels is broadly used to improve existing transportation networks. Lining is the primary support adopted to ensure rock pressure. It has been of high interest in determining stress fields within lining using analytical methods. Analytical solutions for stress distribution within circular lining and around circular and elliptical holes have been proposed by many authors (Bobet [1,2]; Lee and Nam [3]; Timoshenko and Goodier [4]).

Many studies have been carried out to determine the stress and deformation of tunnels by applying numerical methods, which have been generally used to provide an understanding of how the stress and deformation of lining are influenced by different parameters. Numerical methods are largely employed to find the stress and deformation stages of lining in the preliminary stages of design.

Muskhelishvili's [5] complex variable method is one of the useful analytical approaches that fully expounded a basic theory of complex potential functions in order to address some issues of plane elasticity mechanics. Based on this method, Exadaktyol and Stavtopoulou [6,7] proposed a closed-form plane strain solution for stress and displacement around semicircular holes. Verruijt [8,9] calculated the stress and displacement components around a circular tunnel in an elastic half-plane. Zhao and Yang [10] obtained a general solution for deep square tunnels with different pressure coefficients. Kargar et al. [11] made an attempt to study lining stress and deformation in a non-circular deep tunnel

using the Cauchy integral formula of complex variable methods. Li and Chen [12] obtained analytical solutions for a non-circular tunnel lining in power series forms. However, the analytical solutions for stress and displacement found in the above-mentioned literature have seldom come to an available expression for non-circular deep tunnels, especially non-circular deep tunnels with a lining, except for Kargar et al. [11] and Li [12].

When considering the problem with circular support, the solution is much easier. When a non-circular lining is included, the problem considers a multiply-connected region and conformal mapping, which increases the complexity of the problem. Kargar’s [11] method can calculate the stress of a non-circular deep tunnel with a lining, although the method needs to integrate. The integral is too complex and difficult to calculate. Li’s [12] method only considered the non-circular tunnel lining without thinking about the surrounding rock around the lining. In order to simplify the calculation, Li [12] assumed that the surrounding rock has a certain given surface traction applied to the lining. In this study it will be shown that these difficulties can be surmounted at last for the case of a non-circular deep tunnel with certain boundary conditions at infinity, by a new complex variable method in power series forms.

Based on the research findings proposed, an attempt was made in this paper to find the stress distribution and radial displacement of the lining in a non-circular deep tunnel, considering the boundary conditions of the surrounding rocks by applying a complex variable power series method, which is more efficient, simple and accurate. Finally, the new method was validated by the FLAC finite difference software through an example.

2. Problem Statement and General Consideration

The problem refers to a non-circular tunnel with lining in an elastic geomaterial. The tunnel is located at great depth compared with the tunnel dimension; the problem is considered a single hole with support in an infinite plane. The infinite plate on the complex plane is divided into the two isotropic homogenous regions of S_1 and S_2 bounded by contours L_1 and L_2 . The regions S_1 and S_2 refer to the lining and the surrounding rock, respectively. The boundary of the tunnel lining inside (L_1) is free of stress, and the rock-lining interface (L_2) satisfies the continuity boundary conditions. It is assumed that the region S_1 in the z -plane can be mapped conformally onto a ring (O_1) in the ζ -plane. The surrounding rock, region S_2 in the z -plane, can be mapped conformally onto the region O_2 , which is the area outside the L_2 outline in the ζ -plane, see Figure 1. The general formula of the conformal mapping function is determined based on the Laurent series as follows:

$$w(\zeta) = R(\zeta + \sum_{k=0}^{\infty} J_k \zeta^{-k}) \tag{1}$$

where R is positive real number reflecting the hole’s size, and the J_k are generally complex numbers, which are determined by the shape of the tunnel. In most situations it is accurate enough to only take the first few of J_k of the series. θ and ρ are assumed to be two polar coordinates of point ζ in the ζ -plane.

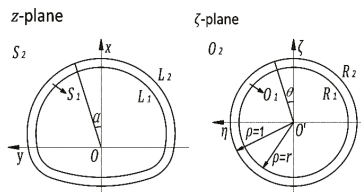


Figure 1. Conformal mapping of the tunnel in the z -plane into two concentric circles in the ζ -plane.

In the complex variable method [5,13,14], the solution is expressed in terms of two functions φ and ψ , which must be analyzed in the region S_1 occupied by the elastic material. The stresses are determined based on the stress functions in the equations:

$$\sigma_\theta + \sigma_\rho = 4\text{Re} \left[\frac{\varphi'(\zeta)}{w'(\zeta)} \right] \tag{2}$$

$$\sigma_\theta - \sigma_\rho + \tau_{\rho\theta} = \frac{2\zeta^2}{\rho^2} \frac{1}{w'(\zeta)} \left[\overline{w(\zeta)} \frac{\varphi''(\zeta)w'(\zeta) - \varphi'(\zeta)w''(\zeta)}{w'(\zeta)w'(\zeta)} + \psi'(\zeta) \right] \tag{3}$$

where σ_ρ , σ_θ and $\tau_{\rho\theta}$ are the radial, circumferential and tangential stress components, respectively. The displacements are given by

$$2G(u_\rho + iu_\theta) = \frac{\bar{\zeta}}{\rho} \frac{\overline{w'(\zeta)}}{|w(\zeta)|} \left[\kappa\varphi(\zeta) - \frac{w(\zeta)}{w'(\zeta)} \overline{\varphi'(\zeta)} - \overline{\psi(\zeta)} \right] \tag{4}$$

where G is the shear modulus of the elastic material, and κ is determined by Poisson’s ratio ν , $\kappa = 3 - 4\nu$ and $\kappa = \frac{3-\nu}{1+\nu}$ are plane strain and plane stress, respectively. In this paper, plane strain conditions are assumed. Based on the Kargar’s [11] method and Chen [15], the stress functions φ_1 and ψ_1 in the region O_2 have the following expansions:

$$\varphi_1(\zeta) = \Gamma w(\zeta) + \varphi_0(\zeta) \tag{5}$$

$$\psi_1(\zeta) = \Gamma' w(\zeta) + \psi_0(\zeta) \tag{6}$$

where

$$\varphi_0(\zeta) = \sum_{k=0}^{\infty} h_k \zeta^{-k} \tag{7}$$

$$\psi_0(\zeta) = \sum_{k=0}^{\infty} m_k \zeta^{-k} \tag{8}$$

where h_k, m_k are generally complex numbers, which must be determined from boundary conditions.

$\varphi_0(\zeta)$ and $\psi_0(\zeta)$ are holomorphic functions with $\varphi_0(\infty) = 0$ and $\psi_0(\infty) = 0$, Γ and Γ' are real and complex constants with regard to the stress state at infinity, which are determined as follows:

$$\Gamma = \frac{1}{4}(\sigma_1 + \sigma_2) = \frac{1+K}{4}\gamma H \tag{9}$$

$$\Gamma' = -\frac{1}{4}(\sigma_1 - \sigma_2)e^{-2i\alpha} = -\frac{1-K}{4}\gamma H \tag{10}$$

where σ_1 and σ_2 are the principal stress components at infinity; α is the angle made between the σ_1 direction and the x axis; K is the lateral pressure coefficient; γ and H are the unit weight of the surrounding rock and the depth of tunnel, respectively.

The stress functions $\varphi_2(\zeta)$ and $\psi_2(\zeta)$, which are represent region O_1 , have the following Laurent series expansions:

$$\varphi_2(\zeta) = \sum_{k=0}^{\infty} a_k \zeta^k + \sum_{k=1}^{\infty} b_k \zeta^{-k} \tag{11}$$

$$\psi_2(\zeta) = \sum_{k=0}^{\infty} c_k \zeta^k + \sum_{k=1}^{\infty} d_k \zeta^{-k} \tag{12}$$

where a_k, b_k, c_k, d_k are generally complex numbers that must be determined from boundary conditions.

Stress functions $\varphi_1(\zeta)$, $\psi_1(\zeta)$, $\varphi_2(\zeta)$ and $\psi_2(\zeta)$ should satisfy the continuity boundary conditions on R_2 circles and satisfy the boundary conditions on R_1 circles. The displacement at lining and rock should be equal on the boundary R_2 . It can be concluded as:

$$u_{\rho 1}^{R2} + iu_{\theta 1}^{R2} = u_{\rho 2}^{R2} + iu_{\theta 2}^{R2} \tag{13}$$

where $u_{\rho 1}^{R2}$ and $u_{\theta 1}^{R2}$ are the lining displacement components of boundary R_2 in the ρ and θ directions, and $u_{\rho 2}^{R2}$ and $u_{\theta 2}^{R2}$ are the rock displacement components of boundary R_2 in the ρ and θ directions, respectively.

The stress at lining and rock should be equal on boundary R_2 . It can be concluded as:

$$f_1^{R2} = f_2^{R2} \tag{14}$$

where f_1^{R2} and f_2^{R2} are displacement components of boundary R_2 in the lining and rock, respectively.

The stress at the lining on the boundary R_1 should be 0. It can be concluded as:

$$f_1^{R1} = 0 \tag{15}$$

Based on Chen [15], the boundary conditions (13)–(15) can be rewritten. Equation (13) is expressed as:

$$\frac{\kappa_1}{G_1} \varphi_0(t_2) - \frac{1}{G_1} \left(\frac{w(t_2)}{w'(t_2)} \overline{\varphi_0'(t_2)} + \overline{\psi_0(t_2)} \right) = \frac{\kappa_2}{G_2} \varphi_2(t_2) - \frac{1}{G_2} \left(\frac{w(t_2)}{w'(t_2)} \overline{\varphi_2'(t_2)} + \overline{\psi_2(t_2)} \right) \tag{16}$$

The stress boundary condition of Equation (14) is expressed as:

$$\varphi_1(t_2) + \frac{w(t_2)}{w'(t_2)} \overline{\varphi_1'(t_2)} + \overline{\psi_1(t_2)} = \varphi_2(t_2) + \frac{w(t_2)}{w'(t_2)} \overline{\varphi_2'(t_2)} + \overline{\psi_2(t_2)} \tag{17}$$

The stress boundary condition of Equation (15) is expressed as:

$$\varphi_2(t_1) + \frac{w(t_1)}{w'(t_1)} \overline{\varphi_2'(t_1)} + \overline{\psi_2(t_1)} = 0 \tag{18}$$

where t_1 and t_2 are the point of the boundary R_1 and R_2 in the ζ -plane, respectively. $u_{\rho 1}$ and $u_{\theta 1}$ are the displacement components of the lining–rock interface in the ρ and θ directions.

The expressions $\Gamma w(\zeta)$ and $\Gamma' w(\zeta)$ should not be incorporated into continuity Equation (16) since they define initial ground stress and deformation in the surrounding rock when tunnels are excavated. Equations (16) and (17) are concerned with the continuity of deformation and the stress field across the lining–rock interface due to the no-slip condition. Equation (18) is concerned that the tunnel lining inside (L_1) is entirely free of stress.

3. Solution

In order to eliminate the difficulties caused by the power series, Equations (16)–(18) are rewritten in the form:

$$\begin{aligned} \frac{\kappa_1}{G_1} \varphi_0(t_2) \overline{w'(t_2)} - \frac{1}{G_1} w(t_2) \overline{\varphi_0'(t_2)} - \frac{1}{G_1} \overline{\psi_0(t_2)} w'(t_2) \\ = \frac{\kappa_2}{G_2} \varphi_2(t_2) \overline{w'(t_2)} - \frac{1}{G_2} w(t_2) \overline{\varphi_2'(t_2)} - \frac{1}{G_2} \overline{\psi_2(t_2)} w'(t_2) \end{aligned} \tag{19}$$

$$\begin{aligned} \varphi_1(t_2) \overline{w'(t_2)} + w(t_2) \overline{\varphi_1'(t_2)} + \overline{\psi_1(t_2)} w'(t_2) \\ = \varphi_2(t_2) \overline{w'(t_2)} + w(t_2) \overline{\varphi_2'(t_2)} + \overline{\psi_2(t_2)} w'(t_2) \end{aligned} \tag{20}$$

$$\varphi_2(t_1) \overline{w'(t_1)} + w(t_1) \overline{\varphi_2'(t_1)} + \overline{\psi_2(t_1)} w'(t_1) = 0 \tag{21}$$

The form of an infinite polynomial times another infinite polynomial, such as $\varphi_0(t_2)\overline{w'(t_2)}$ of Equation (19), is hard to calculate and merge so that the equation cannot be calculated. To acquire a solution for Equations (19)–(21), Li’s method needs to be introduced, which converts the form of the multiplication of two infinite polynomials to an infinite matrix, which can be easily calculated and merged for a computer.

From the power series theory of the complex variable method written by Chen [15], the first factor of Equation (19) on the left can be rewritten as follows:

$$\begin{aligned} \frac{\kappa_1}{G_1} \varphi_0(t_2)\overline{w'(t_2)} &= \frac{\kappa_1}{G_1} \sum_{k=0}^{\infty} h_k \rho^{-k} \sigma^{-k} + \sum_{v=-\infty}^{+\infty} v L_v \rho^{v-1} \sigma^{1-v} \\ &= \frac{\kappa_1}{G_1} \left(\sum_{k=0}^{\infty} h_k \rho^{-k} \sigma^{-k} + \sum_{v=-\infty}^0 v L_v \rho^{v-1} \sigma^{1-v} \right. \\ &\quad \left. + \sum_{k=0}^{\infty} h_k \rho^{-k} \sigma^{-k} + \sum_{v=0}^{+\infty} v L_v \rho^{v-1} \sigma^{1-v} \right) \end{aligned} \tag{22}$$

where k is substituted by v to facilitate the calculation. σ is the angle of the point of the boundary; ρ is the radius of the boundary circle in the ζ -plane, which equals 1 at the lining–rock interface. σ and ρ can be related by $\zeta = \rho\sigma$, where $\sigma = \exp(i\theta)$. L_v can be calculated by R and J_k , and Equation (1) is rewritten in the form:

$$w(\zeta) = \sum_{v=-\infty}^{+\infty} L_v \zeta^{-v} \tag{23}$$

The first item on the right of the Equation (22) must be expanded as follows:

$$\begin{aligned} \frac{\kappa_1}{G_1} \sum_{v=-\infty}^0 v L_v \rho^{v-1} \sigma^{1-v} \sum_{v=0}^{\infty} a_v \rho^v \sigma^v &= \\ &= -\frac{\kappa_1}{G_1} (L_{-1} \rho^{-2} \sigma^2 + 2L_{-2} \rho^{-3} \sigma^3 + 3L_{-3} \rho^{-4} \sigma^4 + \dots)(h_0 + h_1 \rho^{-1} \sigma^{-1} \\ &\quad + h_2 \rho^{-2} \sigma^{-2} + h_3 \rho^{-3} \sigma^{-3} + \dots) \end{aligned} \tag{24}$$

where the positive power of σ in Equation (24) is obtained as:

$$\begin{aligned} \sigma^1 &= -\frac{\kappa_1}{G_1} (h_1 L_{-1} \rho^{-3} \sigma + 2h_2 L_{-2} \rho^{-5} \sigma + 3h_3 L_{-3} \rho^{-7} \sigma + \dots) \\ \sigma^2 &= -\frac{\kappa_1}{G_1} (h_0 L_{-1} \rho^{-2} \sigma^2 + 2h_1 L_{-2} \rho^{-4} \sigma^2 + 3h_2 L_{-3} \rho^{-6} \sigma^2 + \dots) \\ \sigma^3 &= -\frac{\kappa_1}{G_1} (2h_0 L_{-2} \rho^{-3} \sigma^3 + 3h_1 L_{-3} \rho^{-5} \sigma^3 + 4h_2 L_{-4} \rho^{-7} \sigma^3 + \dots) \\ \dots &\dots \end{aligned} \tag{25}$$

The zero and negative powers of σ in Equation (24) can be derived:

$$\begin{aligned} \sigma^0 &= -\frac{\kappa_1}{G_1} (h_2 L_{-1} \rho^{-4} + 2h_3 L_{-2} \rho^{-6} + 3h_4 L_{-3} \rho^{-8} + \dots) \\ \sigma^{-1} &= -\frac{\kappa_1}{G_1} (h_3 L_{-1} \rho^{-5} \sigma^{-1} + 2h_4 L_{-2} \rho^{-7} \sigma^{-1} + 3h_5 L_{-3} \rho^{-9} \sigma^{-1} + \dots) \\ \sigma^{-2} &= -\frac{\kappa_1}{G_1} (h_4 L_{-1} \rho^{-6} \sigma^{-2} + 2h_5 L_{-2} \rho^{-8} \sigma^{-2} + 3h_6 L_{-3} \rho^{-10} \sigma^{-2} + \dots) \\ \dots &\dots \end{aligned} \tag{26}$$

The second item on the right of Equation (22) can be expanded as follows:

$$\begin{aligned} \frac{\kappa_1}{G_1} \sum_{v=1}^{+\infty} v L_v \rho^{v-1} \sigma^{1-v} \sum_{v=0}^{\infty} h_v \rho^{-v} \sigma^{-v} &= \\ &= \frac{\kappa_1}{G_1} (\dots + 3L_3 \rho^2 \sigma^{-2} + 2L_2 \rho^1 \sigma^{-1} + L_1)(h_0 + h_1 \rho^{-1} \sigma^{-1} + h_2 \rho^{-2} \sigma^{-2} \\ &\quad + h_3 \rho^{-3} \sigma^{-3} + \dots) \end{aligned} \tag{27}$$

There are only zero and negative powers of σ in the above Equation (23), which can be derived as follows:

$$\begin{aligned} & \sigma^0 \quad \frac{\kappa_1}{G_1} h_0 L_1 \\ & \sigma^{-1} \quad \frac{\kappa_1}{G_1} (h_1 L_1 \rho^{-1} \sigma^{-1} + 2h_0 L_2 \rho \sigma^{-1}) \\ & \sigma^{-2} \quad \frac{\kappa_1}{G_1} (h_2 L_1 \rho^{-2} \sigma^{-2} + 2h_1 L_2 \sigma^{-2} + 3h_0 L_3 \rho^2 \sigma^{-2}) \\ & \dots \quad \dots \end{aligned} \tag{28}$$

The general formula of Equation (29) are determined based on the expanded functions of Equation (25) as follows:

$$\frac{\kappa_1}{G_1} \sum_{k=0}^{\infty} h_k \rho^{-2k-v} (k+v-1) L_{-k-v+1} \sigma^v \tag{29}$$

The general formula of Equation (30) is determined based on the expanded functions of Equations (26) and (28) as follows:

$$-\frac{\kappa_1}{G_1} \sum_{k=0}^{\infty} h_k \rho^{-2k+v} (k-v-1) L_{-k+v+1} \sigma^{-v} \quad v = 0, 1, 2, 3 \dots \tag{30}$$

Based on the power series of the complex variable method written by Chen [15], which have been presented in Equations (22)–(30), the other items of Equation (19) can be determined and separate the positive and negative exponents of Equation (19); the positive power system of Equation (19) can be expanded as follows:

$$\begin{aligned} & \frac{\kappa_2}{G_2} \sum_{k=0}^{\infty} a_k \rho^{2k-v} (k-v+1) L_{k-v+1} \sigma^v - \frac{\kappa_2}{G_2} \sum_{k=1}^{\infty} b_k \rho^{-2k-v} (k+v-1) L_{-k-v+1} \sigma^v \\ & - \frac{1}{G_2} \sum_{k=1}^{\infty} \bar{a}_k \rho^{2k+v-2k} L_{k+v-1} \sigma^v + \frac{1}{G_2} \sum_{k=1}^{\infty} \bar{b}_k \rho^{-2k+v-2k} L_{-k+v-1} \sigma^v \\ & + \frac{1}{G_2} \sum_{k=0}^{\infty} \bar{c}_k \rho^{-v} (k+v-1) L_{-k-v+1} \sigma^v \\ & - \frac{1}{G_2} \sum_{k=1}^{\infty} \bar{d}_k \rho^{-v} (k-v+1) L_{k-v+1} \sigma^v \\ & + \frac{\kappa_1}{G_1} \sum_{k=0}^{\infty} h_k \rho^{-2k-v} (k+v-1) L_{-k-v+1} \sigma^v \\ & - \frac{1}{G_1} \sum_{k=0}^{\infty} \bar{h}_k \rho^{-2k+v-2k} L_{-k+v-1} \sigma^v + \frac{1}{G_1} \sum_{k=0}^{\infty} m_k \rho^{-v} (k-v+1) L_{k-v+1} \sigma^v \\ & = 0 \end{aligned} \tag{31}$$

$v = 1, 2, 3 \dots$

The negative power system of Equation (19) can be expanded as follows:

$$\begin{aligned} & \frac{\kappa_2}{G_2} \sum_{k=0}^{\infty} a_k \rho^{2k+v} (k+v+1) L_{k+v+1} \sigma^{-v} - \frac{\kappa_2}{G_2} \sum_{k=1}^{\infty} b_k \rho^{-2k+v} (k-v-1) L_{-k+v+1} \sigma^{-v} \\ & - \frac{1}{G_2} \sum_{k=1}^{\infty} \bar{a}_k \rho^{2k-v-2k} L_{k-v-1} \sigma^{-v} + \frac{1}{G_2} \sum_{k=1}^{\infty} \bar{b}_k \rho^{-2k-v-2k} L_{-k-v-1} \sigma^{-v} \\ & + \frac{1}{G_2} \sum_{k=0}^{\infty} \bar{c}_k \rho^v (k-v-1) L_{-k+v+1} \sigma^{-v} \\ & - \frac{1}{G_2} \sum_{k=1}^{\infty} \bar{d}_k \rho^v (k+v+1) L_{k+v+1} \sigma^{-v} \\ & + \frac{\kappa_1}{G_1} \sum_{k=0}^{\infty} h_k \rho^{-2k+v} (k-v-1) L_{-k+v+1} \sigma^{-v} \\ & - \frac{1}{G_1} \sum_{k=0}^{\infty} \bar{h}_k \rho^{-2k-v-2k} L_{-k-v-1} \sigma^{-v} \\ & + \frac{1}{G_1} \sum_{k=0}^{\infty} m_k \rho^v (k+v+1) L_{k+v+1} \sigma^{-v} \\ & = 0 \end{aligned} \tag{32}$$

$v = 1, 2, 3 \dots$

The positive power system of Equation (20) is determined as follows:

$$\begin{aligned}
 & \sum_{k=0}^{\infty} a_k \rho^{2k-v} (k-v+1) L_{k-v+1} \sigma^v - \sum_{k=1}^{\infty} b_k \rho^{-2k-v} (k+v-1) L_{-k-v+1} \sigma^v \\
 & + \sum_{k=1}^{\infty} \bar{a}_k \rho^{2k+v-2} k L_{k+v-1} \sigma^v - \sum_{k=1}^{\infty} \bar{b}_k \rho^{-2k+v-2} k L_{-k+v-1} \sigma^v \\
 & - \sum_{k=0}^{\infty} \bar{c}_k \rho^{-v} (k+v-1) L_{-k-v+1} \sigma^v + \sum_{k=1}^{\infty} \bar{d}_k \rho^{-v} (k-v+1) L_{k-v+1} \sigma^v \\
 & + \sum_{k=0}^{\infty} h_k \rho^{-2k-v} (k+v-1) L_{-k-v+1} \sigma^v + \sum_{k=0}^{\infty} \bar{h}_k \rho^{-2k+v-2} k L_{-k+v-1} \sigma^v \\
 & - \sum_{k=0}^{\infty} m_k \rho^{-v} (k-v+1) L_{k-v+1} \sigma^v \\
 & = 2\Gamma \sum_{k=0}^{\infty} L_k \rho^{2k-v} (k-v+1) L_{k-v+1} \sigma^v \\
 & - 2\Gamma \sum_{k=1}^{\infty} L_{-k} \rho^{-2k-v} (k+v-1) L_{-k-v+1} \sigma^v \\
 & - \Gamma' \sum_{k=0}^{\infty} L_k \rho^{-v} (k+v-1) L_{-k-v+1} \sigma^v \\
 & + \Gamma' \sum_{k=1}^{\infty} L_{-k} \rho^{-v} (k-v+1) L_{k-v+1} \sigma^v \\
 & \quad v = 1, 2, 3 \dots
 \end{aligned} \tag{33}$$

The negative power system of Equation (20) can be expanded as follows:

$$\begin{aligned}
 & \sum_{k=0}^{\infty} a_k \rho^{2k+v} (k+v+1) L_{k+v+1} \sigma^{-v} - \sum_{k=1}^{\infty} b_k \rho^{-2k+v} (k-v-1) L_{-k+v+1} \sigma^{-v} \\
 & + \sum_{k=1}^{\infty} \bar{a}_k \rho^{2k-v-2} k L_{k-v-1} \sigma^{-v} - \sum_{k=1}^{\infty} \bar{b}_k \rho^{-2k-v-2} k L_{-k-v-1} \sigma^{-v} \\
 & - \sum_{k=0}^{\infty} \bar{c}_k \rho^v (k-v-1) L_{-k+v+1} \sigma^{-v} + \sum_{k=1}^{\infty} \bar{d}_k \rho^v (k+v+1) L_{k+v+1} \sigma^{-v} \\
 & + \sum_{k=0}^{\infty} h_k \rho^{-2k+v} (k-v-1) L_{-k+v+1} \sigma^{-v} + \sum_{k=0}^{\infty} \bar{h}_k \rho^{-2k-v-2} k L_{-k-v-1} \sigma^{-v} \\
 & - \sum_{k=0}^{\infty} m_k \rho^v (k+v+1) L_{k+v+1} \sigma^{-v} \\
 & = 2\Gamma \sum_{k=0}^{\infty} L_k \rho^{2k+v} (k+v+1) L_{k+v+1} \sigma^{-v} \\
 & - 2\Gamma \sum_{k=1}^{\infty} L_{-k} \rho^{-2k+v} (k-v-1) L_{-k+v+1} \sigma^{-v} - \Gamma' \sum_{k=0}^{\infty} L_k \rho^v (k-v-1) L_{-k+v+1} \sigma^{-v} \\
 & + \Gamma' \sum_{k=1}^{\infty} L_{-k} \rho^v (k+v+1) L_{k+v+1} \sigma^{-v} \\
 & \quad v = 1, 2, 3 \dots
 \end{aligned} \tag{34}$$

where ρ is the radius of the circle, which equals 1 at the lining–rock interface.

The positive power system of Equation (21) is determined as follows:

$$\begin{aligned}
 & \sum_{k=0}^{\infty} a_k \rho^{2k-v} (k-v+1) L_{k-v+1} \sigma^v - \sum_{k=1}^{\infty} b_k \rho^{-2k-v} (k+v-1) L_{-k-v+1} \sigma^v \\
 & + \sum_{k=1}^{\infty} \bar{a}_k \rho^{2k+v-2} k L_{k+v-1} \sigma^v - \sum_{k=1}^{\infty} \bar{b}_k \rho^{-2k+v-2} k L_{-k+v-1} \sigma^v \\
 & - \sum_{k=0}^{\infty} \bar{c}_k \rho^{-v} (k+v-1) L_{-k-v+1} \sigma^v + \sum_{k=1}^{\infty} \bar{d}_k \rho^{-v} (k-v+1) L_{k-v+1} \sigma^v \\
 & = 0 \\
 & \quad v = 1, 2, 3 \dots
 \end{aligned} \tag{35}$$

The negative power system of Equation (20) can be expanded as follows:

$$\begin{aligned}
 & \sum_{k=0}^{\infty} a_k \rho^{2k+v} (k+v+1) L_{k+v+1} \sigma^{-v} - \sum_{k=1}^{\infty} b_k \rho^{-2k+v} (k-v-1) L_{-k+v+1} \sigma^{-v} \\
 & + \sum_{k=1}^{\infty} \bar{a}_k \rho^{2k-v-2} k L_{k-v-1} \sigma^{-v} - \sum_{k=1}^{\infty} \bar{b}_k \rho^{-2k-v-2} k L_{-k-v-1} \sigma^{-v} \\
 & - \sum_{k=0}^{\infty} \bar{c}_k \rho^v (k-v-1) L_{-k+v+1} \sigma^{-v} + \sum_{k=1}^{\infty} \bar{d}_k \rho^v (k+v+1) L_{k+v+1} \sigma^{-v} \\
 & = 0
 \end{aligned} \tag{36}$$

$v = 1, 2, 3 \dots$

where ρ is the radius of the circle, which equals 0.8633 at the lining–atmosphere interface.

Equations (31)–(36) can be written as a set of linear equations:

$$\begin{bmatrix} [A] & [B] & [C] & [D] & [H] & [M] \end{bmatrix}_{(6v+3) \times (6k+4)} = [F]_{(6k+3) \times 1} \tag{37}$$

where $[A]$, $[B]$, $[C]$, $[D]$, $[H]$, $[M]$ represent the coefficients of the a_k , b_k , c_k , d_k , h_k and m_k terms in the equations, respectively. $[F]$ represents the coefficient of the right side of each equation; $[a]$, $[b]$, $[c]$, $[d]$, $[h]$, and $[m]$ represent the unknowns, respectively. The coefficients a_k , b_k , c_k , d_k , h_k and m_k required in the final stress function are obtained by Equation (37).

As Equation (26) has $6k + 4$ unknowns and $6v + 3$ conditions, where $v \rightarrow \infty$ and $k \rightarrow \infty$, there cannot be a unique solution. It can be easily seen that Equation (37) is linearly related when $k \rightarrow \infty$ and $\rho = 1$. The number of conditions in the equation set is reduced from $(6v + 3)$ to $(6v + 2)$. Considering that $\varphi_0(\infty) = 0$ and $\psi_0(\infty) = 0$, the coefficients h_k and m_k can take any value if $k \rightarrow \infty$. It is indicated that h_∞ and m_∞ can take zero. Since the coefficients h_∞ and m_∞ are known, the number of unknown coefficients in the equation set is reduced from $(6k + 4)$ to $(6k + 2)$. The number of unknown coefficients equals the boundary conditions, in which all the coefficients have been determined uniquely. Equations (5), (6), (11) and (12) are obtained by the calculated coefficients, and the stress and deformation of the non-circular deep tunnel are obtained through Equations (2)–(4).

4. Implementation

In this section, the new complex variable method is applied to an example and a comparison is provided with FLAC finite difference software in order to verify the formula.

4.1. Fundamental Assumption

(a) The tunnel is assumed to have an infinite length; the surrounding rock mass is homogeneous, isotropic and linear elastic and without creep or viscous behaviors. (b) The tunnel’s length and depth are assumed to far outweigh its diameter; the surrounding rock mass conforms to the plane strain condition ($\kappa = 3 - 4\nu$).

4.2. Comparison of the New Analytical Solution with That of the Numerical Simulation Results

The tunnel distribution diagram is presented and a 3916 zones and 13887 grid-points finite mesh calculation model was used to simulate stress and displacement distribution in Figure 2. The horizontal displacement of the finite mesh calculation model is constrained by the left and right boundary, the vertical displacement is constrained by the bottom boundary, and the top boundary is free and unconstrained. The numerical model is concerned with continuity of deformation and the stress field

across the lining–rock interface due to the no-slip condition. The tunnel lining inside should be entirely free of stress.

The calculation parameters are shown in Table 1.

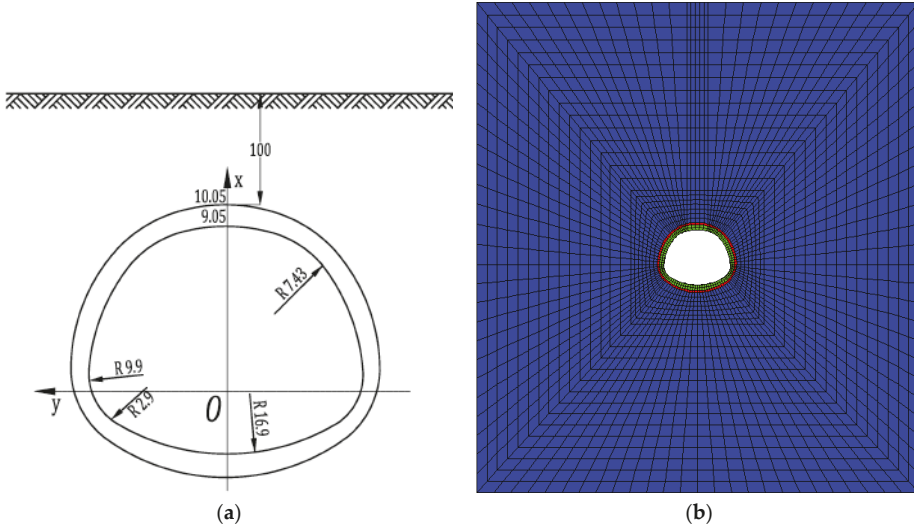


Figure 2. (a) Tunnel distribution diagram (Unit: m) and (b) Finite mesh calculation model.

Table 1. Main physical parameter for tunnel calculation.

Material Type	Elasticity Modulus E (MPa)	Poisson’s Ratio ν	Density ($\text{kN}\cdot\text{m}^{-3}$)	Lateral Pressure Coefficient K
Shale	25,000	0.3	26	0.5
Lining	30,000	0.2	25	0.5

According to Lv’s [16,17] method and the geometry of the tunnel (in Figure 2), the conformal mapping function (Equation (1)) was determined and provided by a self-programming optimal design software as follows:

$$w(\zeta) = 8.0339(\zeta + 0.3121 - 0.0697\zeta^{-1} + 0.0338\zeta^{-2} - 0.0087\zeta^{-3} - 0.0068\zeta^{-4}) \quad (38)$$

where coefficient $k = 4$ is close enough to Equation (1). The radius $\rho = 0.8633$ is related to ζ by $\zeta = \rho\sigma$, where $\sigma = \exp(i\theta)$. It is assumed that the tunnel lining inside (L_1) can be mapped conformally onto a circle (R_1). When the radius $\rho = 1$ the L_2 can be mapped conformally onto R_2 .

As an example, the boundary condition across the lining–rock interface and tunnel lining inside can be determined by Equations (13)–(15). The boundary conditions at infinity can be expressed through Equations (9) and (10).

Based on Equation (37), a simple computer program written by MATLAB was applied to solve the problem.

As the coordinates of the analytical solution and numerical simulation are different, it is necessary to rewrite the results. The comparison of the rewritten results between the analytical solution and numerical simulation are shown below.

Figure 3 shows the circumferential stress along the rock–lining interface predicted by the new analytical solution and the FLAC finite difference software. It can be observed that the maximum

circumferential stress happens at a position of an 85-degree angle (i.e., the widest part of the tunnel) and, moreover, the circumferential stress of the new analytical solution has not declined rapidly, but creates a stress concentration at $\alpha = 115^\circ$. The circumferential stress along the inner lining periphery is presented in Figure 4a, demonstrating good agreement between the new analytical solution and the numerical simulation apart from an 85-degree angle. Normal stress and shear stress along the inner lining periphery is illustrated in Figure 4b,c; the maximum value of the analytical solution for normal stress and shear stress are about 200 KPa and 100 KPa, respectively, and the maximum value of the numerical simulation of normal stress and shear stress are about 350 KPa and 600 KPa. The analytical solution is smaller than the numerical simulation. The analytical solution is more accurate than the numerical simulation.

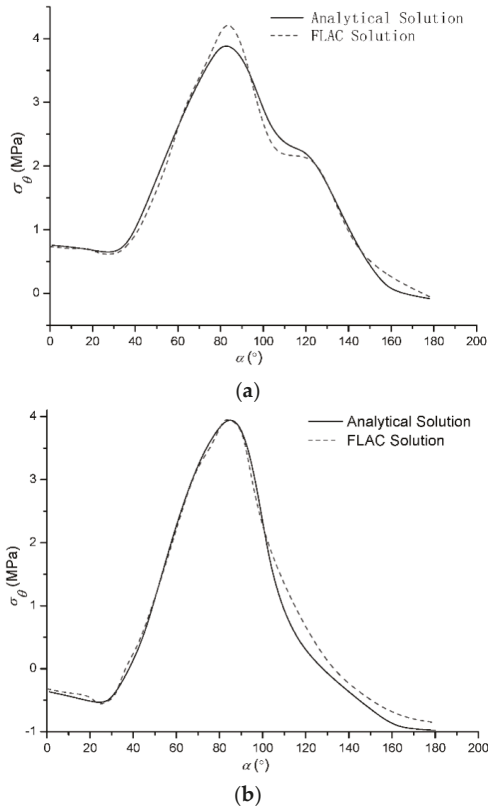


Figure 3. Circumferential stress along the rock–lining interface (a) from the lining side (b) from the rock side.

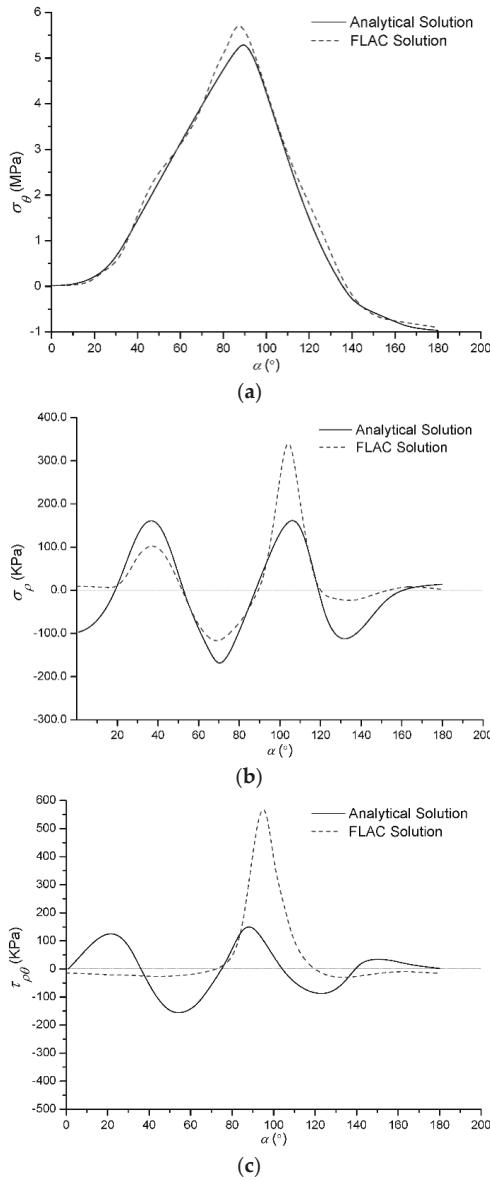


Figure 4. Stress along the inner lining periphery (a) circumferential stress (b) normal stress (c) shear stress.

Figure 5 shows the radial displacement of the tunnel along the rock–lining interface predicted by the analytical solution. It could be demonstrated that the radial displacement along the rock–lining interface was in good agreement with the displacement boundary condition, which proves its high accuracy.

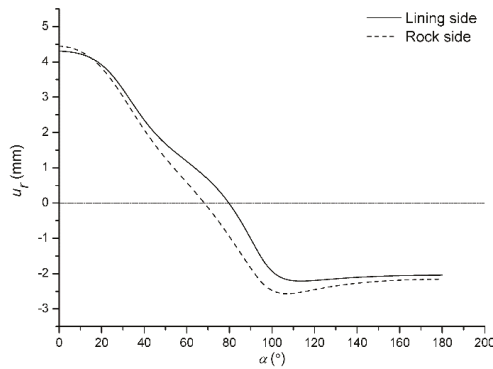


Figure 5. Radial displacement along the rock–lining interface predicted by the analytical solution.

The radial displacement of the tunnel along the inner lining periphery is illustrated in Figure 6, which shows that the radial displacement of the analytical solution and numerical simulation are all zero at $\alpha = 75^\circ$. It was demonstrated that the numerical solution agrees well with the analytical solution. Considering the results of Figure 5, the analytical solution had good agreement with the displacement boundary condition, thus the analytical solution results were reasonable.

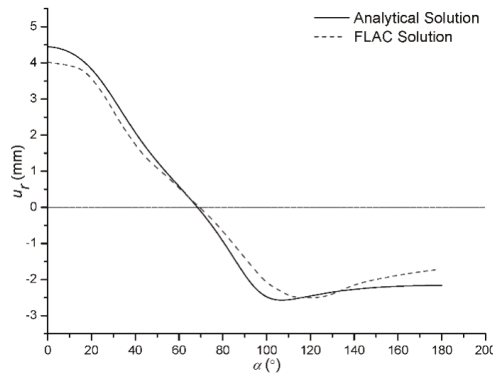


Figure 6. Radial displacement along the inner lining periphery.

The discrepancies between the new analytical solution and the numerical simulation described above, especially Figure 4, may be due to the fact that the grid size in the numerical modeling is not small enough to produce accurate results. The stress information of the numerical simulation is stored in zones not in grid points, and the stress cannot be accurately expressed along a specified boundary.

5. Conclusions

In this paper, the stress and displacement of a non-circular deep tunnel and within their lining supports were studied using a new analytical solution, which is based on the basic theory of complex variables and plane elasticity [17], and the following conclusions can be made.

The analytic functions were exactly established to predict the stress and displacement distribution of the non-circular deep tunnel within their lining supports, but it is obviously not entirely true that the stress and displacement value is only determined by the in-situ stress boundary conditions and coefficient of the elasticity modulus, Poisson’s ratio, lateral pressure and material density.

The analytical solution for radial displacement was smaller than the numerical simulation results, however, and further study will be needed to develop these functions.

Due to the fact that the grid size in modeling was not small enough to produce accurate results and stress information was stored in zones, not in grid points in the numerical simulation, the stress cannot be accurately expressed along a specified boundary. But the analytical solution results were not affected by grid size and zones in the numerical modeling.

The curves of the stress value showed that the new analytical solution and numerical simulation were in reasonable agreement. Both solutions predicted a normal stress concentration at the lower and upper corners of the tunnel, and both maximum circumferential stress results occurred in the widest part of the tunnels. The normal and shear stress values of the tunnel along the inner lining periphery were almost zero, which proved its high accuracy.

Although numerical simulation is the main tool for solving tunnel excavation problems, especially non-circular tunnels, the complex variable method can provide another way to solve non-circular tunnel excavation problems in a faster and more accurate way.

Author Contributions: Y.L. and S.C. conceived and theoretical research; Y.L. performed the formula derivation; Y.L. and S.C. verified results by numerical simulation; Y.L. wrote the paper; S.C. checked and proofread the paper.

Acknowledgments: We thank the Fundamental Research Funds for the Central Universities (SWJTU11ZT33) and the Innovative Research Team in University (IRT0955) for their sponsorship of this project, and thanks to Professor Chen, who guided and revised the paper.

Conflicts of Interest: The authors declare no conflict of interest.

References

1. Bobet, A. Analytical solutions for shallow tunnels in saturated ground. *J. Eng. Mech.* **2001**, *127*, 1258–1266. [[CrossRef](#)]
2. Bobet, A. Effect of pore water pressure on tunnel support during static and seismic loading. *Tunn. Undergr. Space Technol.* **2003**, *18*, 377–393. [[CrossRef](#)]
3. Lee, I.M.; Nam, S.W. The study of seepage forces acting on the tunnel lining and tunnel face in shallow tunnels. *Tunn. Undergr. Space Technol.* **2001**, *16*, 31–40. [[CrossRef](#)]
4. Timoshenko, S.P.; Goodier, J. *Theory of Elasticity*, 2nd ed.; McGraw-Hill: New York, NY, USA, 1951.
5. Muskhelishvili, N.I.; Radok, J.R.M. *Some Basic Problems of the Mathematical Theory of Elasticity*; Cambridge University Press: Cambridge, UK, 1953.
6. Exadaktylos, G.; Stavropoulou, M. A closed-form elastic solution for stresses and displacements around tunnels. *Int. J. Rock Mech. Min. Sci.* **2002**, *39*, 905–916. [[CrossRef](#)]
7. Exadaktylos, G.E.; Liolios, P.A.; Stavropoulou, M.C. A semi-analytical elastic stress displacement solution for notched circular openings in rocks. *Int. J. Solids Struct.* **2003**, *40*, 1165–1187. [[CrossRef](#)]
8. Verruijt, A. A complex variable solution for a deforming circular tunnel in an elastic half-plane. *Int. J. Numer. Anal. Methods Geomech.* **1997**, *21*, 77–89. [[CrossRef](#)]
9. Verruijt, A. Deformations of an elastic half plane with a circular cavity. *Int. J. Solids Struct.* **1998**, *35*, 2795–2804. [[CrossRef](#)]
10. Zhao, G.P.; Yang, S.L. Analytical solutions for rock stress around square tunnels using complex variable theory. *Int. J. Rock Mech. Min. Sci.* **2015**, *80*, 302–307. [[CrossRef](#)]
11. Kargar, A.R.; Rahmangebadi, R.; Hajabasi, M.A. A semi-analytical elastic solution for stress field of lined non-circular tunnels at great depth using complex variable method. *Int. J. Solids Struct.* **2014**, *51*, 1475–1482. [[CrossRef](#)]
12. Li, Y.S.; Chen, S.G. A Complex Variable Solution for Stress and Deformation of Lining in a Non-Circular Tunnel. Scientific Research Report. Southwest Jiaotong University: Chengdu, China, 2018. (In Chinese)
13. Liu, F.S. Seepage Studies of Tunnel Water-Enriched Region Based on Fluid-Solid Coupling Theory and Complex Analysis. Ph.D. Thesis, South China University, Guangzhou, China, 2012. (In Chinese)
14. Wang, G.Q. *Elastic Mechanics*; China Railway Publishing House: Beijing, China, 2008. (In Chinese)
15. Chen, Z.Y. *Analytical Method in Mechanical Analysis of Surrounding Rock*, 1st ed.; China Coal Industry Publishing House: Beijing, China, 1994. (In Chinese)

16. Lv, Z.A.; Zhang, L.Q. *Complex Function Method for Mechanical Analysis of Underground Tunnel*, 1st ed.; Science Press: Beijing, China, 2007. (In Chinese)
17. Brown, J.W.; Churchill, R.V. *Complex Variables and Applications*, 9th ed.; China Machine Press: Beijing, China, 2015. (In Chinese)



© 2018 by the authors. Licensee MDPI, Basel, Switzerland. This article is an open access article distributed under the terms and conditions of the Creative Commons Attribution (CC BY) license (<http://creativecommons.org/licenses/by/4.0/>).

Article

4D Remeshing Using a Space-Time Finite Element Method for Elastodynamics Problems

Serge Dumont ¹, Franck Jourdan ^{2,*} and Tarik Madani ²

¹ Institut Montpellierain Alexander Grothendieck, University Montpellier, CNRS, 34090 Montpellier, France; serge.dumont@umontpellier.fr

² Laboratory of Mechanics and Civil Engineering, University Montpellier, CNRS, 34090 Montpellier, France; tarik.madani@umontpellier.fr

* Correspondence: franck.jourdan@umontpellier.fr; Tel.: +33-467-149-633

Received: 10 March 2018; Accepted: 22 May 2018; Published: 25 May 2018

Abstract: In this article, a Space-Time Finite Element Method (STFEM) is proposed for the resolution of mechanical problems involving three dimensions in space and one in time. Special attention will be paid to the non-separation of the space and time variables because this kind of interpolation is well suited to mesh adaptation. For that purpose, we have developed a technique of 4D mesh generation adapted to space-time remeshing. A difficulty arose in the representation of 4D finite elements and meshes. This original technique does not require coarse-to-fine and fine-to-coarse mesh-to-mesh transfer operators and does not increase the size of the linear systems to be solved, compared to traditional finite element methods. Space-time meshes are composed of simplex finite elements. Computations are carried out in the context of the continuous Galerkin method. We have tested the method on a linearized elastodynamics problem. Our technique of mesh adaptation was validated on elementary examples and applied to a problem of mobile loading. The convergence and stability of the method are studied and compared with existing methods. This work is a first implementation of 4D space-time remeshing. A stability criterion for the method is established, as well as a convergence rate of about two. Using simplex elements, it is possible to develop a technique of mesh adaptation able to follow a mobile loading zone.

Keywords: finite elements; space-time; elastodynamics; mesh adaptation

1. Introduction

The STFEM (Space-Time Finite Element Method) can be regarded as an extension of the classical finite element method, applied to a boundary problem resulting from a non-stationary problem. Currently, several approaches exist. One can quote for example the Large Time INcrement method (LATIN [1]), the discontinuous Galerkin method [2–4] and our method, which is a continuous Galerkin method [5,6]. In most publications on the discontinuous Galerkin method, like in [7], the interpolation functions are assumed to be a product of functions of space variables and functions of time variables. We will see in this paper that special attention will be paid to the non-separation of the space and time variables. The reason for this choice is not motivated by the accuracy of the numerical results, but rather by what constitutes the aim of our study: remeshing. We will see that this kind of interpolation is well suited to mesh adaptation. The space-time mesh adaptation we developed is based on a method of mesh generation not structured in space and time. The construction of 4D meshes collides with the limits of representation. To overcome this difficulty, we propose an automatic method of construction inspired by what can be achieved in 2D and 3D. Our technique of mesh adaptation was applied to a problem of mobile load like contact forces. Our approach makes possible the building of an evolutionary mesh able to follow the clamping zone.

Moreover, this technique does not require a mesh-to-mesh transfer operator and allows the preservation of the exact sizes of the linear systems on each space-time slab.

Let us note that one of the drawbacks of the STFEM such as defined in the works of [8,9] is the size of the linear systems to be solved, since it is necessary to solve the full 4D problem at once. The use of a laminated mesh allows us to avoid the assembling of the total matrix of the problem and permits us to consider only submatrices. This drastically reduces the size of the systems to be solved. The size of these linear systems is exactly the same as that obtained in the case of approaches coupling an incremental method of finite differences type to solve time integration, with the “classical” finite element method being used to solve the space problem.

Another large group of methods is based on semi-discretisation, whereby finite elements are used in space and finite differences are used in time. Even if this well-known technique is simpler to use in a classical framework, the remeshing required is expensive due to the necessity of the construction of interpolation/restriction operators between the grids.

The paper is organized as follows. In Section 2, the elastodynamics problem is formulated, and the space-time finite element method is developed. The 4D mesh generation is presented in Section 3, and a paragraph is specially devoted to adaptive mesh refinement. Numerical results are presented and discussed in Section 4.

2. Principle of the Method

We consider the motion of an elastic body within the small perturbations hypothesis. Let Ω be the set taken up by the body and $[0, T]$ a time interval. The body is submitted to volume force density f_d , boundary force density F_d on its boundary part $\partial_1\Omega$ and imposed displacements u_d on its boundary part $\partial_0\Omega$ ($\partial\Omega = \partial_0\Omega \cup \partial_1\Omega$, $\partial_0\Omega \cap \partial_1\Omega = \emptyset$). The dynamic problem is: seek the displacement u and the Cauchy stress tensor σ such that:

$$\begin{cases} \operatorname{div}(\sigma(x,t)) + f_d(x,t) = \rho \ddot{u}(x,t) & \forall (x,t) \in \Omega \times]0, T[\\ \sigma(x,t)n(x,t) = F_d(x,t) & \forall (x,t) \in \partial_1\Omega \times [0, T] \\ u(x,t) = u_d(x,t) & \forall (x,t) \in \partial_0\Omega \times [0, T] \\ u(x,t) = u_0(x) & \forall (x,t) \in \Omega \times \{0\} \\ \dot{u}(x,t) = \dot{u}_0(x) & \forall (x,t) \in \Omega \times \{0\} \\ \sigma(x,t) = a\varepsilon(x,t) & \forall (x,t) \in \Omega \times [0, T] \end{cases} \quad (1)$$

where ρ is the specific mass, \ddot{u} is the second derivative of the displacement with respect to time, u_0 is the initial displacement, \dot{u}_0 is the initial velocity, a is the Hooke tensor and ε is the infinitesimal linear strain tensor. The aim of this study is to use a finite element method. Then, the previous dynamic problem has to be considered as a boundary problem on the time interval $[0, T]$. For that purpose, as in the cases of the discontinuous Galerkin method [2,10,11] and the LARge Time INcrement (LATIN) method [1,12], the variational formulation is written on the whole space-time domain $\Omega \times [0, T]$. The variational formulation of the previous boundary problem can be written as follows:

Find $u \in U_{ad}$ such that:

$$\int_0^T \int_{\Omega} (\rho \ddot{u}v + a\varepsilon(u) : \varepsilon(v) - f_d v) dxdt = \int_0^T \int_{\partial_1\Omega} F_d v dsdt, \quad (2)$$

$$\forall v \in U_{ad}^0$$

where U_{ad} is the set of displacements, regular enough, which verifies the boundary kinematic conditions and the initial conditions, v is the virtual displacement and U_{ad}^0 is the set of virtual displacements, regular enough, which verify boundary kinematic conditions only.

The first term on the left-hand side of Equation (2) is integrated by parts in time in order to determine the first derivative of u and the initial velocity. It gives:

$$\int_0^T \int_{\Omega} \rho \ddot{u} v dx dt = - \int_0^T \int_{\Omega} \rho \dot{u} \dot{v} dx dt + \int_{\Omega} [\rho \dot{u}_T(x) v(x, T) - \rho \dot{u}_0(x) v(x, 0)] dx \tag{3}$$

where $\dot{u}_T(x)$ is the velocity at time $t = T$.

The space-time finite element method (STFEM) was firstly proposed in [5,6]. Their discretisation used structured space-time meshes obtained as the Cartesian product of spatial elements and a time interval, which is not generally suitable for space-time mesh adaptations. Since then, numerous papers on STFEM have been published. Most of them, like [11,13], deal with the discontinuous Galerkin method in time, but the discretisation also uses structured meshes obtained as the Cartesian product of spatial elements and a time interval. However, the STFEM proposed in [2] has been developed on unstructured meshes. It also employs the discontinuous Galerkin method in time and incorporates stabilizing terms of the least squares type. The space and time discontinuities of all variables are taken into account. In our study, we use a continuous Galerkin method. Classical Lagrange polynomials are used. The finite elements are isoparametric. On a space-time finite element E_e (Figure 1), the displacement verifies:

$$u(x, t) = \sum_{i=1}^{n_e} \varphi_i^e(x, t) u_i^e \tag{4}$$

where n_e is the total number of nodes of the element E_e , φ_i^e are the interpolation functions and u_i^e the nodal displacements. Using matrix notation, one has:

$$u(x, t) = N_e(x, t) U_e \text{ where } U_e = (u_1^e, \dots, u_{n_e}^e)^T \text{ and } N_e(x, t) = (\varphi_1^e(x, t), \dots, \varphi_{n_e}^e(x, t)) \tag{5}$$

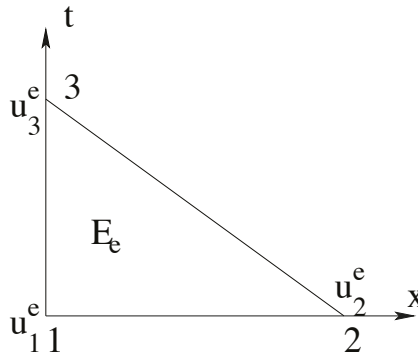


Figure 1. 2D space-time finite element.

The same interpolation is used for the virtual displacement v . Then:

$$v(x, t) = N_e(x, t) V_e \text{ where } V_e = (v_1^e, \dots, v_{n_e}^e)^T \tag{6}$$

Let p be the total number of space-time elements; the previous discretization gives:

$$\int_0^T \int_{\Omega} \rho \ddot{u} \dot{v} dx dt = \sum_{e=1}^p V_e^T M_e U_e \tag{7}$$

where:

$$M_e = \int_0^T \int_{E_e} \rho \frac{\partial N_e^T}{\partial t} \frac{\partial N_e}{\partial t} dx dt \tag{8}$$

is the elementary matrix relative to the inertia forces. One can notice that M_e is symmetric. Concerning the discretization of the initial and final impulses' contributions, one has:

$$\int_{\Omega} [\rho \dot{u}_T(x)v(x, T) - \rho \dot{u}_0(x)v(x, 0)] dx = \sum_{e=1}^p V_e^T \Lambda_e \tag{9}$$

where Λ_e is the elementary vector relative to the initial and final impulses. It is defined by:

$$\Lambda_e = [\int_{E_e \cap \Omega_T} \rho N_e^T \dot{u}_T dx - \int_{E_e \cap \Omega_0} \rho \dot{u}_0 dx] \tag{10}$$

where Ω_0 is the domain at time $t = 0$ and Ω_T is the domain at time $t = T$.

Similarly, let B_e be the matrix such that:

$$\varepsilon(u(x, t)) = B_e(x, t)U_e, \tag{11}$$

the virtual works of internal and external forces are respectively discretized by:

$$\int_0^T \int_{\Omega} a \varepsilon(u) : \varepsilon(v) dx dt = \sum_{e=1}^p V_e^T K_e U_e \tag{12}$$

and:

$$\int_0^T \int_{\Omega} f_d v dx dt + \int_0^T \int_{\partial_1 \Omega} F_d v ds dt = \sum_{e=1}^p V_e^T F_e \tag{13}$$

where the elementary matrix K_e relative to internal forces is:

$$K_e = \int_0^T \int_{E_e} B_e^T a B_e dx dt \tag{14}$$

and the elementary vector F_e relative to external forces is:

$$F_e = \int_0^T \int_{E_e} N_e^T f_d dx dt + \int_0^T \int_{E_e \cap \partial_1 \Omega} N_e^T F_d ds dt. \tag{15}$$

This space-time discretization leads to the following linear system:

$$([\widetilde{M}_u] + [\widetilde{K}_u])\{U\} = \{F_u\} + \{\Lambda\} \tag{16}$$

where $[\widetilde{M}_u]$ is the assembled matrix relative to the inertia forces, $[\widetilde{K}_u]$ is the assembled matrix relative to the internal forces, $\{F_u\}$ is the nodal vector of external forces, Λ is the nodal vector of impulses and $\{U\}$ is the nodal vector of displacements. One can note that the matrices $[\widetilde{M}_u]$ and $[\widetilde{K}_u]$ are symmetric. In order to have band matrices, and because we have in mind making computations incrementally in time, the meshes are built to be stratified in time, as in Figure 2. Moreover, the node numbering is conducted in such a way that all nodes in a same stratum have close numbers, then the left-hand side of the system (16) verifies.

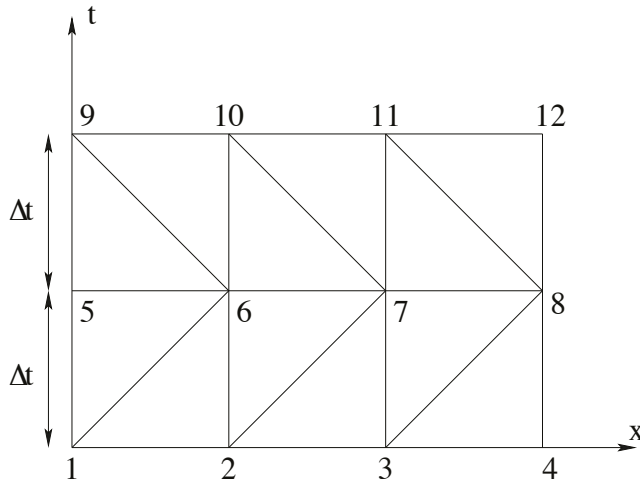


Figure 2. 2D regular space-time mesh.

$$([\widetilde{M}_u] + [\widetilde{K}_u])\{U\} = [T]\{U\} =$$

$$\begin{pmatrix} [T_{11}] & [T_{12}] & 0 & 0 & 0 & 0 \\ [T_{21}] & [T_{22}] & [T_{23}] & 0 & 0 & 0 \\ 0 & [T_{32}] & [T_{33}] & [T_{34}] & 0 & 0 \\ \cdot & \cdot & \cdot & \cdot & \cdot & \cdot \\ 0 & 0 & 0 & [T_{n/n-1}] & [T_{n/n}] & [T_{n/n+1}] \\ 0 & 0 & 0 & 0 & [T_{n+1/n}] & [T_{n+1/n+1}] \end{pmatrix} \begin{pmatrix} \{U_0\} \\ \{U_1\} \\ \cdot \\ \cdot \\ \cdot \\ \{U_n\} \end{pmatrix}.$$

Using the space-time mesh described in Figure 2, one has:

$$\{U_j\} = \begin{pmatrix} u_{j+1} \\ u_{j+2} \\ u_{j+3} \\ u_{j+4} \end{pmatrix} \text{ for } j = 0, \dots, n.$$

With this numbering, the total matrix $[T]$ and the sub-matrices $[T_{ij}]$ are band matrices.

Comments:

- Choosing a Lagrange interpolation for displacements implies that displacements are continuous, but the velocities are discontinuous. As a consequence, integration by parts as in (3) is not totally rigorous, and it could be necessary to use the discontinuous Galerkin formulation, which amounts to writing the derivative of velocity within the theory of distributions. We will preserve the formulation in (3), knowing that the error here is of the same order as in the case of traditional finite elements in space. Indeed, with a Lagrange interpolation local displacements are continuous, whereas the global deformation is discontinuous.
- Even if it is not absolutely necessary, the advantage of using a laminated mesh such as defined here is that it becomes possible, rather than assembling the total matrix $[T]$, to only assemble the sub-matrices $[T_{ij}]$. This considerably reduces the size of the systems to be solved. More precisely, the size of these linear systems is exactly the same as that obtained in the case of approaches based on the coupling of finite incremental differences in time with finite elements in space. Moreover, the method is not limited to simplex elements, and the spatial position of each set of nodes can vary from one time plane to the other. It is one of the main advantages of the method.

- We specify that the nodal vector relating the boundary conditions with velocity $\{\Lambda\}$ is written as:

$$\{\Lambda\} = (\{\Lambda_0\}, 0, \dots, 0, \{\Lambda_n\})^T$$

where $\{\Lambda_0\}$ is given starting from conditions of initial velocity while $\{\Lambda_n\}$ is unknown. Consequently, the resolution of System (16) is the following:

The first system of equations,

$$[T_{11}]\{U_0\} + [T_{12}]\{U_1\} = \{F_0\} + \{\Lambda_0\} \tag{17}$$

provides $\{U_1\}$; the system of equations:

$$[T_{i/i-1}]\{U_{i-2}\} + [T_{i/i}]\{U_{i-1}\} + [T_{i/i+1}]\{U_i\} = \{F_{i-1}\} \quad 2 \leq i \leq n, \tag{18}$$

provides the displacements $\{U_i\}$; and the last system of equations,

$$[T_{n+1/n}]\{U_{n-1}\} + [T_{n+1/n+1}]\{U_n\} = \{F_n\} + \{\Lambda_n\}, \tag{19}$$

gives $\{\Lambda_n\}$.

- Finally, the matrices of resolution $[T_{i/i+1}]$ are generally non-symmetric, even if the total matrix $[T]$ is symmetric. Thus, for the algorithm presented above, a non-symmetrical solver should be used. This can appear penalizing in terms of computing time. However, since the final objective is to use this approach to deal with problems of contact with friction and since the nonlinear resolution we developed in [14] is of the Gauss–Seidel nonlinear type, asymmetries do not affect computing time.

3. 4D Mesh and Remeshing

In order to propose a remeshing technique, it is firstly necessary to be able to build 4D meshes. Obtaining only one 4D finite element does not pose real problems, even if some difficulties in graphic representation arise (see Figure 3). On the contrary, building a 4D mesh, even the most elementary is far from being commonplace, except in the case of regular meshes formed by finite elements of multiplexing type (functions of interpolation obtained as the products of functions of space by functions of time). However, in the general case and in particular with the problem of remeshing, which is what is of interest here, the meshing remains an issue.

3.1. 4D Mesh Generation

Figure 3 identifies parts of elementary 2D, 3D and 4D meshes with their node numbering. One denotes by n_0 the total number of nodes at time $t = 0$ of the entire space mesh, and we assume this total number is the same at time $t = h$.

For the 2D mesh, the connectivities are

$$\begin{aligned} & i, j, n_0 + i \\ & j, n_0 + i, n_0 + j. \end{aligned}$$

For the 3D mesh, the connectivities are

$$\begin{aligned} & i, j, k, n_0 + i \\ & j, k, n_0 + i, n_0 + j \\ & k, n_0 + i, n_0 + j, n_0 + k. \end{aligned}$$

Using the previous building of connectivities, obtained by circular permutations, we propose the following generalization of connectivities for the 4D mesh.

$$\begin{aligned} & i, j, k, l, n_0 + i \\ & j, k, l, n_0 + i, n_0 + j \end{aligned}$$

$$k, l, n_0 + i, n_0 + j, n_0 + k$$

$$l, n_0 + i, n_0 + j, n_0 + k, n_0 + l.$$

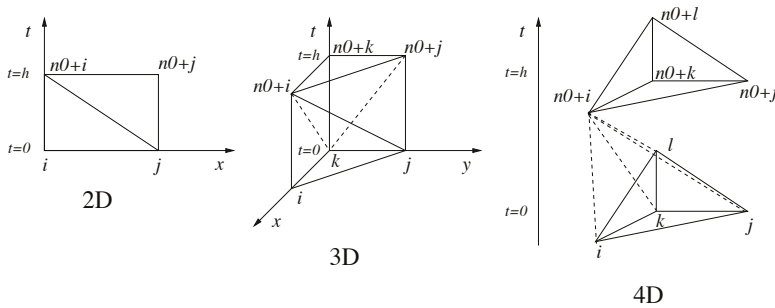


Figure 3. 2D, 3D and 4D space-time mesh.

This 4D mesh is constituted by four hypertetrahedrons (The hypertetrahedron is the four-dimensional tetrahedron. Other names of this element type are simplex or pentatope). We propose to build 4D space-time meshes, resulting from unspecified 3D space meshes, by applying the building technique developed above, for each 3D finite element of the 3D space mesh. However, in this case, it must be checked that the total space-time volume is covered by the 4D mesh. For this purpose, we computed the sum of the volumes of the hypertetrahedrons of the 4D mesh and compared it with the total volume generated by the 3D object multiplied by the time interval.

For a 3D mesh made up of tetrahedrons, the interfaces between the elements are triangles. In 4D, these interfaces are tetrahedrons (see the diagram at the bottom of Figure 4). Therefore, we must thus check that for our technique of mesh generation, all couples of adjoining 4D finite elements have a common tetrahedron. As we use a building technique containing circular permutations, it is necessary to respect a particular order in the numbering of the nodes of each 3D finite element. A way of doing this is to arrange the nodes of each 3D element in ascending order. Table 1 gives an example of a table of connectivities for an elementary 4D mesh, resulting from the 3D space mesh represented by the left-hand diagram of Figure 4. Let us note that this 4D mesh contains eight finite elements, against two for the 3D mesh source, and that $n_0 = 5$. It is observed that the connectivities are arranged in ascending order. In this case, it is checked that the tetrahedra filling the space-time interface (diagram at the right-hand of Figure 4) are common to the adjoining elements. Indeed, Elements 1 and 5 contain the tetrahedron (1; 2; 4; 6), and Elements 2 and 6 contain the tetrahedron (2; 4; 6; 7). Lastly, Elements 4 and 7 contain the tetrahedron (4; 6; 7; 9). Let us notice that the tetrahedron (1; 2; 3; 4; 5) at time t and the related tetrahedron (6; 7; 8; 9; 10) (not represented) at time $t + \Delta t$ could also have different shapes and could be localized at different places (see for example Figure 5). In this case, the triangles (1; 2; 4) and (6; 7; 9) in the right part of Figure 4 can be different.

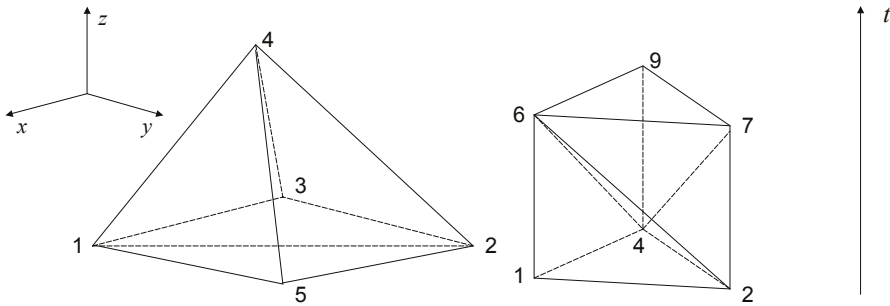


Figure 4. 3D initial mesh (scheme at the left); part of the 4D mesh generated by the triangle (1; 2; 4) common to the two finite elements of the 3D initial mesh (scheme at the right).

Table 1. Table of connectivities of the 4D space-time mesh resulting from the elementary 3D space mesh of Figure 4.

Element Number	Node 1	Node 2	Node 3	Node 4	Node 5
1	1	2	3	4	6
2	2	3	4	6	7
3	3	4	6	7	8
4	4	6	7	8	9
5	1	2	4	5	6
6	2	4	5	6	7
7	4	5	6	7	9
8	5	6	7	9	10

3.2. Remeshing Technique

In this section, we present our technique of space-time mesh adaptations. In the literature, many articles on mesh adaptations [2,3,15–21] can be found. Among these papers, a large number deals with space-time mesh adaptations. They use the discontinuous Galerkin method. In most of them, the approach is incremental, i.e., remeshing is carried out at given steps of time. Generally, the values of the unknown of the new mesh are obtained by approximation or interpolation from those of the old mesh, which we will call “mesh-to-mesh transfer”. Moreover, the interpolation used is of a multiplexing type; the function of interpolation is defined by the product of a function of space by a function of time.

In [22], we proposed an incremental technique for mesh adaptation, which does not require mesh-to-mesh transfer. It was coupled with problems of rubbing contact (see [14]). In addition, we developed a non-incremental technique of mesh adaptation, based on non-structured space-time meshes.

Some teams have already worked on this problem. One can quote the works of Hugues and Hulbert [2,3], Tezduyar et al. [20,21] and Idesman et al. [9,23]. They use the continuous or discontinuous Galerkin method. In these approaches, calculations are carried out on the whole space-time domain $\Omega \times [0, T]$. Thus, for a field Ω of dimension d and a total number N of nodes of the space-time mesh, the dimension of the linear problem to be solved is $d \times N$, which quickly becomes large when $d = 2$ or $d = 3$. A solution to decrease the computational time is to use parallel computations. This is the option chosen in [8,9].

In the context of the continuous Galerkin method, we suggested, in [22,24], a non-incremental solution, which substitutes the concept of a step of time by that of a “space-time front”. Erickson et al. [16] have also proposed an advancing-front mesh generation, in the context of the discontinuous Galerkin method. This technique was successfully used by Miller et al. [25] in their multi-field space-time discontinuous Galerkin method, for $d = 1$ and 2 in linearized elastodynamics

applications. The advantage of this frontal resolution is that it decreases the size of the linear systems to be solved. Due to technical difficulties, the frontal resolution in the case of $d = 3$ has not yet been implemented. Nevertheless, we propose a particular incremental remeshing technique based on the construction of 4D space-time meshes that are able to follow an evolutionary loaded zone. This technique of mesh generation uses simplex finite elements. Figure 5 gives an illustration of the technique. The principle is to maintain the same number of nodes during the simulation, but to locate a sufficiently large number of them under the loaded area. In this particular case, it is possible to preserve the matrices $T_{i/i-1}, T_{i/i}, T_{i/i+1}$ identical for all i , which involves a reduction of the computational time. An example of mechanical application is provided in the following section. This technique is aimed at applications in simulating problems of wear between two bodies in contact.

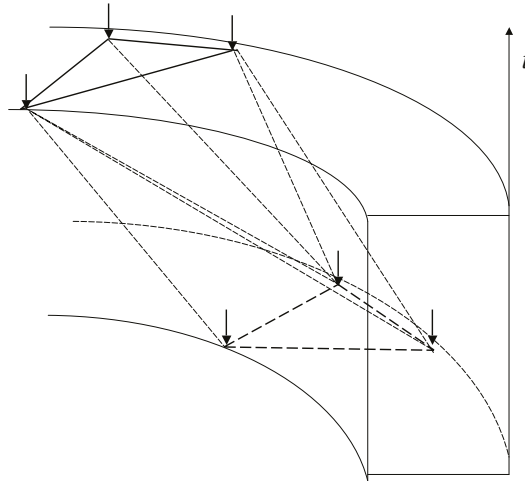


Figure 5. Space-time mesh generation by rotation of the loaded area. The loaded area is represented by arrows.

4. Numerical Analysis

Our space-time finite elements method was programmed using MATLAB software and was validated on elementary examples.

4.1. Stability

Preliminary results on the stability of the method have been established in [22] and compared with the Newmark integration scheme. Here, we summarize the main results. Let δ and θ be two real parameters; the Newmark integration scheme reads:

$$\begin{cases} \{\dot{U}_{i+1}\} = \{\dot{U}_i\} + \Delta t [(1 - \delta) \{\ddot{U}_i\} + \delta \{\ddot{U}_{i+1}\}] \\ \{U_{i+1}\} = \{U_i\} + \Delta t \{\dot{U}_i\} + \Delta t^2 \left[\left(\frac{1}{2} - \theta\right) \{\ddot{U}_i\} + \theta \{\ddot{U}_{i+1}\} \right] \end{cases}$$

where Δt is the time step of integration, $\{\dot{U}_{i+1}\}$ and $\{\ddot{U}_{i+1}\}$ are respectively the assembled vector of nodal velocities and accelerations at time $(i + 1)\Delta t$. We showed in [22] that:

- For 1D space-time elastodynamic applications, the use of the STFEM method with linear simplex elements is similar to the use of the implicit Newmark integration scheme with $\delta = 1/2$ and $\theta = 1/3$. The method is then unconditionally stable.
- For 2D space-time elastodynamic applications, the use of the STFEM method with linear simplex elements is similar to the use of the explicit Newmark integration scheme with $\delta = 1/2$ and $\theta = 0$.

The method is then conditionally stable. Classically, the time step has to verify the CFLcondition: $\Delta t \leq \min_j \frac{2}{\omega_j}$, where each ω_j is the frequency of a normal mode of vibration.

- For higher dimensions (3D and 4D), no direct relationship between the STFEM and the Newmark method has been established. Nevertheless, we noted that our method required sufficiently small space-time slabs, of the same order of the discretization time step necessary with explicit methods of integration.
- Furthermore, the use of the STFEM method with multiplex elements is similar to the use of the implicit Newmark integration scheme with $\delta = 1/2$ and $\theta = 1/3$, for 1D, 2D, 3D and 4D space-time applications. In this case, the method is unconditionally stable.

In the present study, a specific numerical investigation has been carried out to estimate the stability conditions for the STFEM method with linear simplex elements for 4D space-time elastodynamic applications. The stability was tested on a beam of length $L = 0.1$ m and a square section of 0.01×0.01 m² (see Figure 6). The Young modulus E was equal to 1000 Pa; the Poisson's ratio ν was equal to 0.3; and the density ρ was equal to 680 kg/m³.

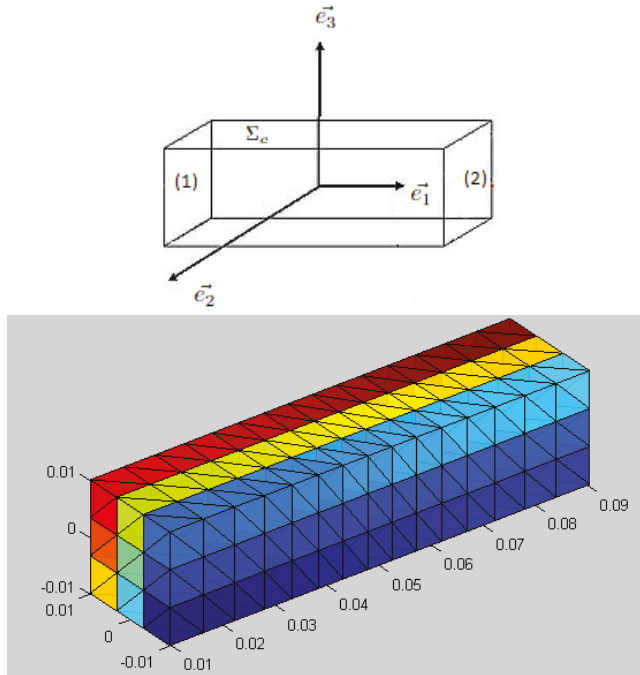


Figure 6. Geometry and 3D mesh of a beam with $h = 6.6 \times 10^{-3}$ m.

We built boundary conditions in order to obtain the following analytic solution:

$$u(x, t) = \cos\left(\frac{\pi x_1}{L}\right) \cos\left(\frac{\pi c t}{L}\right) e_1 \tag{20}$$

where c is the velocity of the wave propagation. On Faces (1) and (2), null Neumann conditions were imposed. On the other four faces (Σ_e), Dirichlet conditions were imposed in order to satisfy the analytic

solution (20). The volume external force density f_d was assumed to be vanishing. This imposes that the wave velocity c must verify:

$$c = \sqrt{\frac{E}{\rho(1+\nu)}\left(1 + \frac{\nu}{\rho(1-2\nu)}\right)}$$

Results plotted in Figure 7 give the dependence of the time discretization (size of the space-time slab) Δt on the average size h of the 3D finite elements, to ensure the stability of the method.

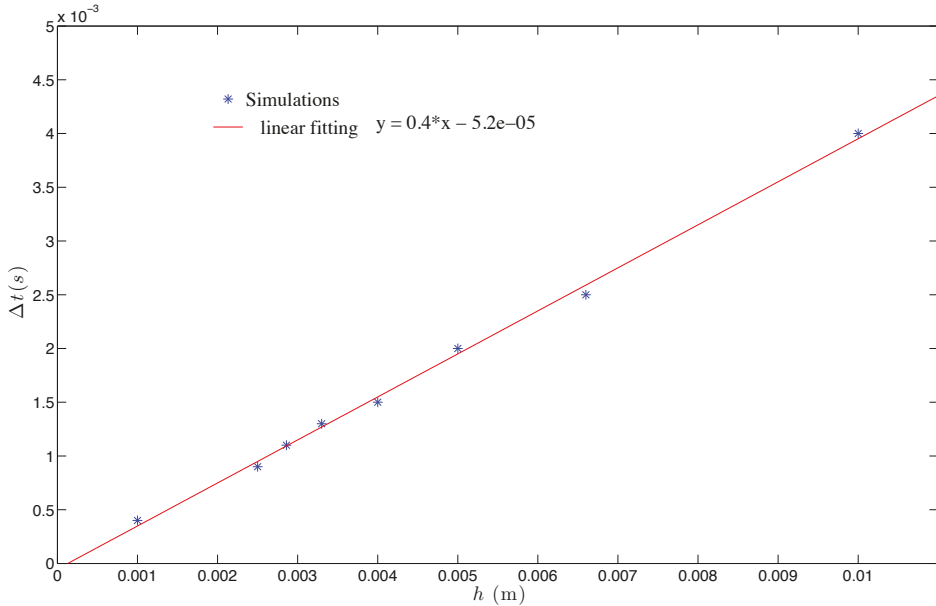


Figure 7. Size of the time step of discretization Δt necessary for stability with respect to the average size h of the 3D finite elements.

Linear fitting suggests that the stability criterion is:

$$\Delta t \leq \alpha h$$

with $\alpha \simeq 1/2c$. Indeed, in our example, $c = 1.407$ m/s.

4.2. Convergence

In the case of simplex finite elements, the convergence with the STFEM method is comparable to the convergence with the Newmark scheme, for the 1D and 2D problem. Concerning the convergence analysis of the STFEM in 4D, we used the previous example. The time step of discretization Δt is scaled with respect to h , using the stability criterion obtained in the previous paragraph. We computed the maximum error over space at the last time step between the analytic solution and the numerical solution for each mesh size h . The results are plotted in Figure 8.

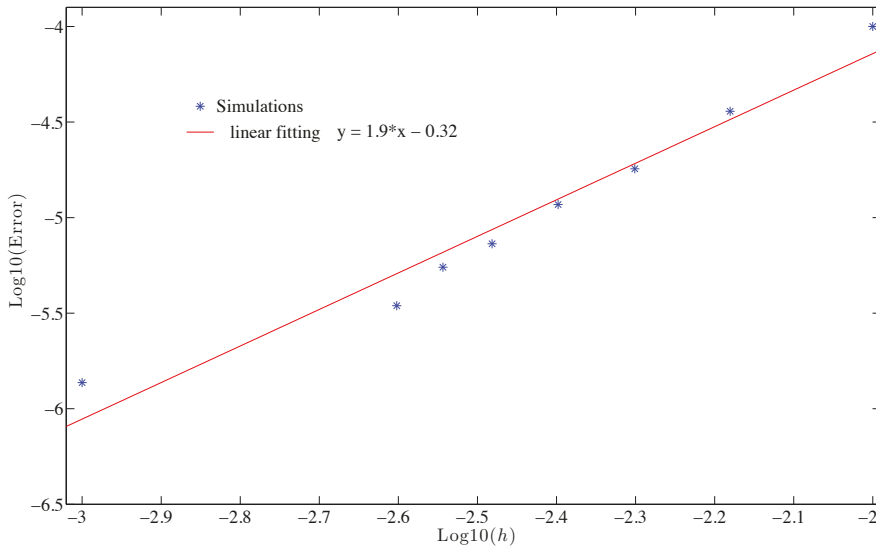


Figure 8. Maximum error over the space, at the last time step, between the analytic solution and the numerical solution for each mesh size h , in the logarithmic scale.

We can note that the convergence rate for the method is nearly quadratic.

5. Numerical Results on Mesh Adaptation

To illustrate our technique of mesh adaptation, we consider the example of a brake disc subjected to the clamping of a plate on one of its faces (see the source model with the coarse mesh in Figure 9) and blocked on the opposite face. The disc is made of steel with a Young’s modulus equal to 210,000 MPa, a Poisson’s ratio equal to 0.3 and a density equal to 7800 kg/m³. The internal radius of the disc is equal to 40 mm; its external radius is equal to 100 mm; and its thickness is 10 mm. Two 3D initial meshes have been tested: a coarse mesh, which contains 634 nodes and 1752 elements, refined only in the area of the clamping, and a fine mesh, which contains 6476 nodes and 25,856 elements and has a uniform mesh fineness over all the sample.

The clamping area is modeled by a constant pressure of 100 MPa. This area is moved along the circumference of the disc with a rotational speed equal to that of the propagating wave $V = \frac{1}{2\pi R} \sqrt{\frac{E}{\rho}}$, where $R = 70$ mm is the average radius of the disc. For both 3D initial meshes, we built an incremental 4D space-time mesh, which preserves the 3D mesh at each time step, by imposing an axial rotation to keep the finest zone of the 3D mesh under the loading area. An illustration is shown schematically in Figure 5.

The results of the calculations presented were obtained for space-time slabs of 10^{-7} s (this is equivalent to using a time step equal to 10^{-7} s). The vertical displacements obtained with fine and coarse meshes have been compared for points located on a circle of control, of radius R equal to 70 mm (see Figure 10).

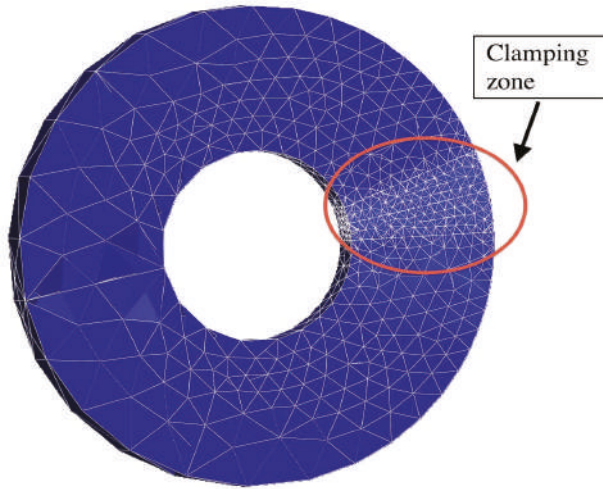


Figure 9. 3D initial coarse mesh: the mesh is finer under the clamping zone.

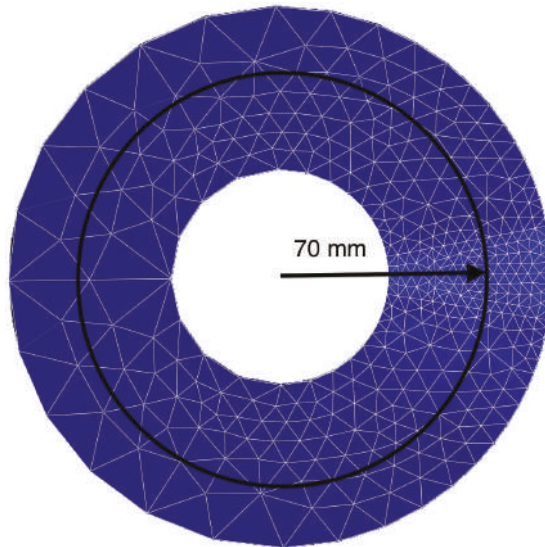


Figure 10. Location zone of checked displacements: circle of radius equal to 70 mm.

Numerical values are gathered in Figure 11 for the results at time $t = 2.10^{-5}$ s and in Figure 12 for the results at time $t = 4.10^{-5}$ s. Each check point is defined by its angle, in polar coordinates.

Numerical comparisons show that the coarse and fine meshes give similar results in the clamping zone. However, apart from this zone, the results are somewhat different. Let us note that nodal displacements cannot be identical because dynamic effects depend on the fineness of the mesh.

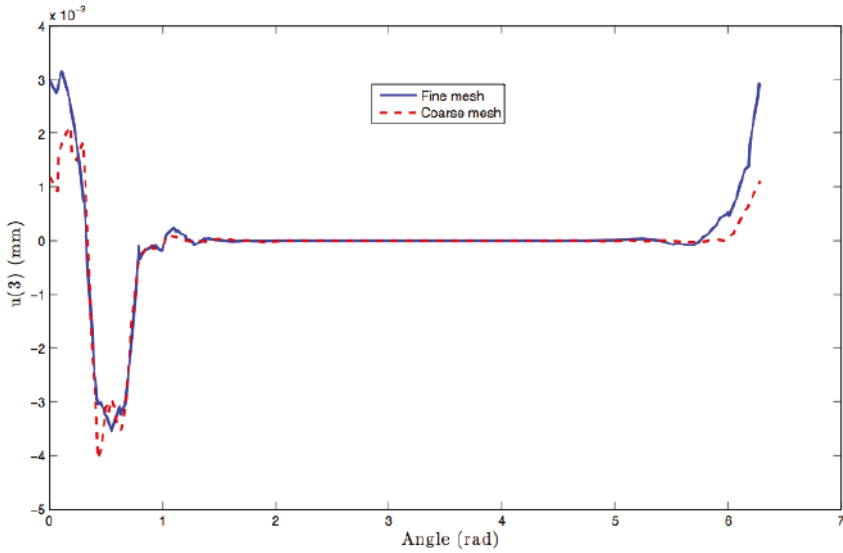


Figure 11. Comparison of vertical displacements for points situated on the circle of control, expressed in mm, at time $t = 2.10^{-5}$ s. Each check point is defined by its angular coordinate, expressed in radians.

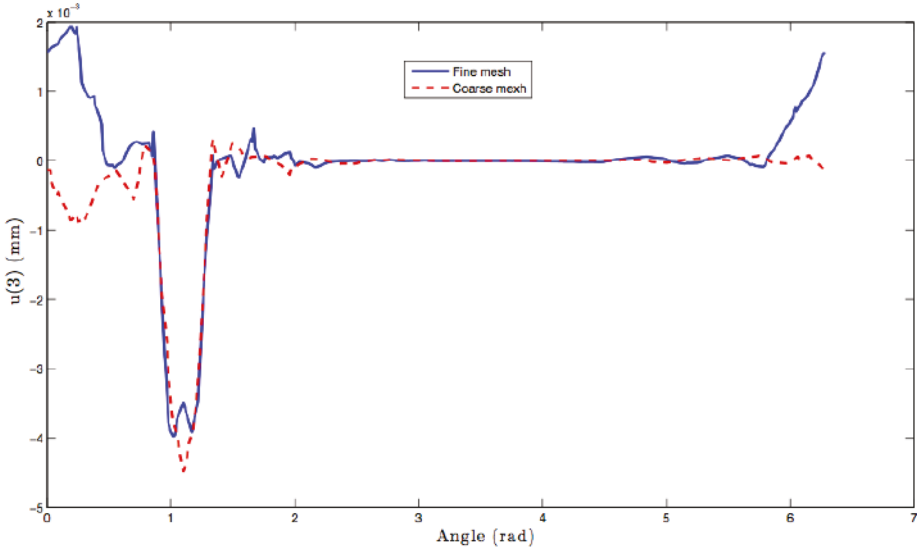


Figure 12. Comparison of vertical displacements for points situated on the circle of control, expressed in mm, at time $t = 4.10^{-5}$ s. Each check point is defined by its angular coordinate, expressed in radians.

Figures 13 and 14 show the norm of incremental displacements at time $t = 2.10^{-5}$ s and $t = 4.10^{-5}$ s for the coarse and the fine mesh, respectively. For the coarse mesh, we can observe that the refined zone really remains under the zone of clamping. The distribution of the norm of node displacements is similar for the two positions of the load. It is important to note that they are incremental displacements and not total displacements.

Finally, it must be noted that the computational time is 6.6-times faster using the coarse mesh.

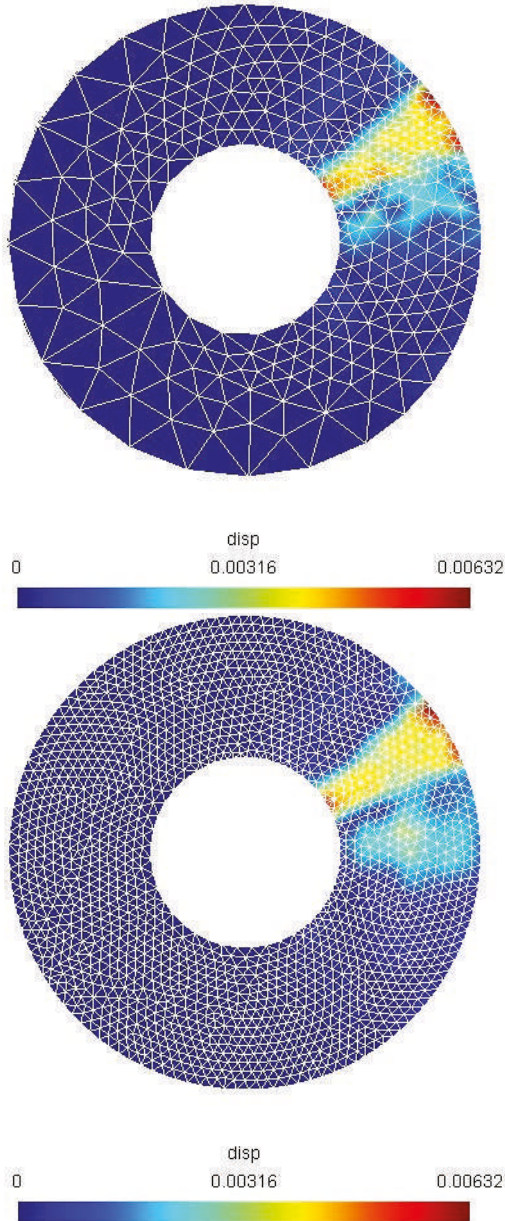


Figure 13. Isovalues of the norm of nodal displacements, expressed in mm, at $t = 2 \cdot 10^{-5}$ s for the coarse mesh (image at the top) and for the fine mesh (image at the bottom).

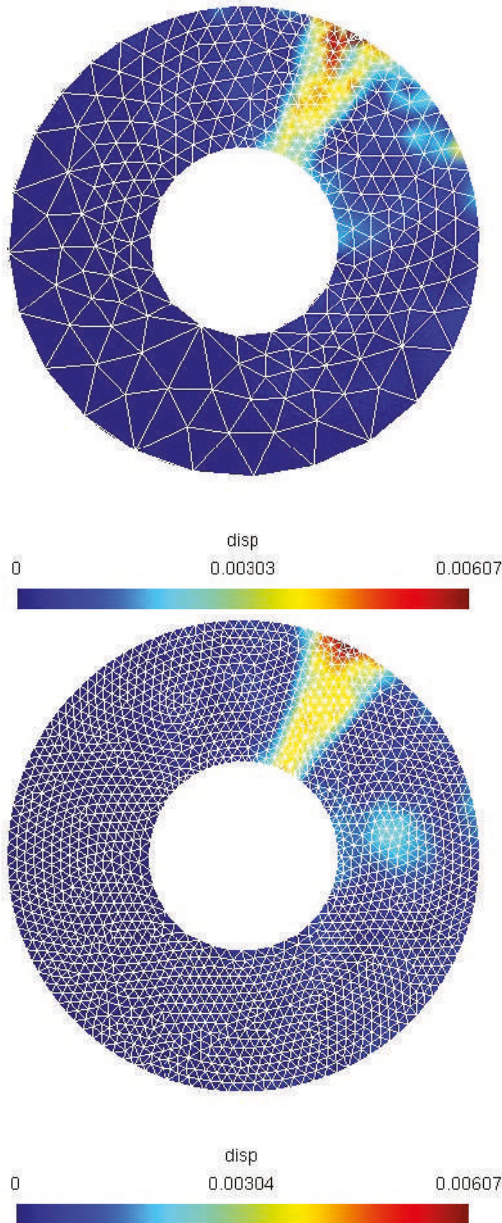


Figure 14. Isovalues of the norm of nodal displacements, expressed in mm, at $t = 4.10^{-5}$ s for the coarse mesh (image on the top) and for the fine mesh (image on the bottom).

6. Conclusions

The method we have presented for space-time mesh generation for 4D domains, using simplex elements, made it possible to develop a technique of mesh adaptation able to follow a mobile loading zone. This original technique has been carried out to ensure a minimal computational time and does

not require coarse-to-fine and fine-to-coarse mesh transfer operators. The convergence and stability of the method were studied and compared with existing methods. This approach opens the way to 4D remeshing. It allows, thanks to simplex elements, remeshing in both space and in time.

However, to demonstrate the all the capacities of this method, it is necessary to go much further in the mechanical applications and to propose a technique of 4D mesh adaptation using the frontal approach, as presented in [14,16,22,25].

Author Contributions: Conceptualization, F. Jourdan; Software, S. Dumont, F. Jourdan; Validation, T. Madani; Original Draft Preparation, S. Dumont, F. Jourdan and T. Madani.

Conflicts of Interest: The authors declare no conflict of interest.

References

1. Ladevèze, P. *Non Linear Computational Structural Mechanics, New Approaches and Non Incremental Methods of Calculation*; Springer: New York, NY, USA, 1999.
2. Hughes, T.J.R.; Hulbert, G.M. Space-time finite element methods for elastodynamics: Formulations and error estimates. *Comput. Methods Appl. Mech. Eng.* **1988**, *66*, 339–363. [[CrossRef](#)]
3. Hulbert, G.M.; Hughes, T.J.R. Space-time finite element methods for second-order hyperbolic equations. *Comput. Methods Appl. Mech. Eng.* **1990**, *84*, 327–348. [[CrossRef](#)]
4. Khalmanova, D.K.; Costanzo, F. A space-time discontinuous Galerkin finite element method for fully coupled linear thermo-elasto-dynamic problems with strain and heat flux discontinuities. *Comput. Methods Appl. Mech. Eng.* **2008**, *197*, 1323–1342. [[CrossRef](#)]
5. Argyris, J.H.; Scharpf, D.W. Finite elements in time and space. *Nucl. Eng. Des.* **1969**, *10*, 456–464. [[CrossRef](#)]
6. Zienkiewicz, O.C.; Parekh, C.J. Transient field problems—two and three dimensional analysis by isoparametric finite elements. *Int. J. Numer. Methods Eng.* **1970**, *2*, 61–71. [[CrossRef](#)]
7. Chien, C.C.; Yang, C.S.; Tang, J.H. Three-dimensional transient elastodynamic analysis by a space and time-discontinuous Galerkin finite element method. *Finite Elem. Anal. Des.* **2003**, *39*, 561–580. [[CrossRef](#)]
8. Anderson, M.; Kim, J.-H. A numerical approach to space-time finite elements for the wave equation. *J. Comput. Phys.* **2007**, *226*, 466–476. [[CrossRef](#)]
9. Idesman, A.V. Solution of linear elastodynamics problems with space-time finite elements on structured and unstructured meshes. *Comput. Methods Appl. Mech. Eng.* **2007**, *196*, 1787–1815. [[CrossRef](#)]
10. Huang, H.; Costanzo, F. On the use of space-time finite elements in the solution of elasto-dynamic problems with strain discontinuities. *Comput. Methods Appl. Mech. Eng.* **2002**, *191*, 5315–5343. [[CrossRef](#)]
11. Karaoglan, L.; Noor, A.K. Space-time finite element methods for sensitivity analysis of contact/impact response of axisymmetric composite structures. *Comput. Methods Appl. Mech. Eng.* **1997**, *144*, 371–389. [[CrossRef](#)]
12. Jourdan, F.; Bussy, P. Large time increment method in dynamic regularization: Sheet cutting simulations. *Comput. Methods Appl. Mech. Eng.* **2000**, *190*, 1245–1259. [[CrossRef](#)]
13. Li, X.D.; Wiberg, N.-E. Implementation and adaptivity of space-time finite element method for structural dynamics. *Comput. Methods Appl. Mech. Eng.* **1998**, *156*, 211–229. [[CrossRef](#)]
14. Adélaïde, L.; Jourdan, F.; Bohatier, C. Frictional contact solver and mesh adaptation in Space-Time Finite Element Method. *Eur. J. Mech. A/Solids* **2003**, *22*, 633–647. [[CrossRef](#)]
15. Donea, R.; Huerta, A.; Sarrate, J. Arbitrary Lagrangian-Eulerian for fluid-rigid body interaction. *Comput. Methods Appl. Mech. Eng.* **2001**, *190*, 3171–3188.
16. Erickson, J.; Guoy, D.; Sullivan, J.M.; Üngör, A. Building spacetime meshes over arbitrary spatial domains. In Proceedings of the 11th International Meshing Round Table, Sandia, Ithaca, NY, USA, 15–18 September 2002; pp. 391–402.
17. Farhat, C.; Degand, C. A three-dimensional torsional spring analogy method for unstructured dynamic meshes. *Comput. Struct.* **2002**, *80*, 305–316.
18. Feng, Y.T.; Peric, D. A time-adaptive space-time finite element method for incompressible Lagrangian flows with free surfaces: Computational issues. *Comput. Methods Appl. Mech. Eng.* **2000**, *190*, 499–518. [[CrossRef](#)]
19. Mohr, R.; Menzel, A.; Steinmann, P. A consistent time FE-method for large strain elasto-plasto-dynamics. *Comput. Methods Appl. Mech. Eng.* **2008**, *197*, 3024–3044. [[CrossRef](#)]

20. Tezduyar, T.E.; Sunil, S. Enhanced-discretization space-time technique (EDSTT). *Comput. Methods Appl. Mech. Eng.* **2004**, *193*, 1385–1401. [[CrossRef](#)]
21. Tezduyar, T.E.; Sathe, S.; Keedy, R.; Stein, K. Space-time finite element techniques for computation of fluid-structure interactions. *Comput. Methods Appl. Mech. Eng.* **2006**, *195*, 2002–2027. [[CrossRef](#)]
22. Adélaïde, L.; Jourdan, F.; Bohatier, C. Méthode des éléments finis espace-temps et remaillage. *Rev. Eur. Elem. Finis* **2003**, *12*, 427–459. [[CrossRef](#)]
23. Idesman, A.; Niekamp, R.; Stein, E. Continuous and discontinuous Galerkin methods with finite elements in space and time for parallel computing of viscoelastic deformation. *Comput. Methods Appl. Mech. Eng.* **2000**, *190*, 1049–1063. [[CrossRef](#)]
24. Adélaïde, L.; Jourdan, F.; Bohatier, C. New results on mesh adaptation in space-time finite element method. In Proceedings of the ASME Engineering Technology Conference on Energy (ETCE 2002/STRUC-29042), Houston, TX, USA, 4–5 February 2002.
25. Miller, S.T.; Kraczek, B.; Haber, R.B.; Johnson, D.D. Multi-field spacetime discontinuous Galerkin methods for linearized elastodynamics. *Comput. Methods Appl. Mech. Eng.* **2009**, *199*, 34–47. [[CrossRef](#)]



© 2018 by the authors. Licensee MDPI, Basel, Switzerland. This article is an open access article distributed under the terms and conditions of the Creative Commons Attribution (CC BY) license (<http://creativecommons.org/licenses/by/4.0/>).



Article

Integration of Direction Fields with Standard Options in Finite Element Programs

Herbert Moldenhauer

Dipl.-Ing. H. Moldenhauer GmbH, Im Brückengarten 9 A, 63322 Rödermark, Germany;
hm@FEM-Moldenhauer.de; Tel.: +49-06074-1394

Received: 11 March 2018; Accepted: 4 May 2018; Published: 7 May 2018

Abstract: The two-dimensional differential equation $y' = f(x,y)$ can be interpreted as a direction field. Commercial Finite Element (FE) programs can be used for this integration task without additional programming, provided that these programs have options for the calculation of orthotropic heat conduction problems. The differential equation to be integrated with arbitrary boundaries is idealized as an FE model with thermal 2D elements. Its orthotropic thermal conductivities are specified as $k_1 = 1$ and $k_2 = 0$. In doing so, k_1 is parallel to y' , and k_2 is oriented perpendicular to this. For this extreme case, it is shown that the isotherms are identical to the solution of $y' = f(x,y)$. The direction fields, for example, can be velocity vectors in fluid mechanics or principal stress directions in structural mechanics. In the case of the latter, possibilities for application in the construction of fiber-reinforced plastics (FRP) arise, since fiber courses, which follow the local principal stress directions, make use of the superior stiffness and strength of the fibers.

Keywords: direction field; tensor line; principal stress; tailored fiber placement; heat conduction

1. Introduction

Orthotropic materials can have extremely different thermal conductivities, for example, in printed circuit boards. The tracks conducting current are made of copper (Cu) and are electrically insulated against the plastic plate. Due to its low thermal conductivity (k_2), the Cu conducting track (k_1) is heated to a constant, relatively high temperature. It can be considered as an isothermal line. The thermal heat flow in the plastic due to conduction is very low. For example, if there are two Cu conducting tracks with constant but different temperatures, then a steady temperature gradient independent of k_2 prevails in the plastic between them, even if $k_2 \rightarrow 0$. The Cu-tracks can be described by their position $y = y(x)$, and they control the temperature distribution in the insulator. Alternatively, the position can be described by $y'(x)$ together with their starting positions. If these tracks are infinitely densely distributed, the direction field of the Cu-conductance k_1 is described by $y' = f(x,y)$. Insulation works perpendicular to the Cu-tracks when $k_2 \ll k_1$. Should the (infinitely densely) guided conduction paths be directed parallel to an arbitrary direction field $y' = f(x,y)$, then the following hypothesis shall be mathematically verified:

Hypothesis: *The isotherms of an orthotropic steady-state 2D thermal conduction problem with the thermal conductivities k_1 and k_2 are tangential to an arbitrarily prescribed direction field $y' = f(x,y)$ provided that the local orientation of k_1 follows the direction field y' , and perfect insulation exists perpendicular to this ($k_2 = 0$).*

The integration method, which can be derived from the hypothesis, is the topic of the dissertation by the author [1]; however, this was published without mathematical verification. Two-dimensional direction fields of the type $y' = f(x,y)$ can describe physically different processes. In fluid mechanics, the vectorial direction field $y' = v(x,y)/u(x,y)$ of the velocity components u and v are tangential to the streamlines. The general solution of the direction field to be integrated provides the flow field in the

form of streamlines. This task is solved by default in Computational Fluid Dynamics (CFD) codes and is therefore not pursued further here. In stress analysis, the visualization of principal stress (PS) lines is not present in commercial FE programs. The visualization of stream and tensor lines is the subject of numerous investigations. A representative selection is given by [2–6].

Beyer [2] investigated in his dissertation principal stress trajectories arising in civil engineering and in constructions of fiber-reinforced plastics. He established an algorithm for their visualization in two and three dimensions. The procedure is similar to the method shown in Figure 1; however, improved accuracy is gained with his variable and iterative step control.

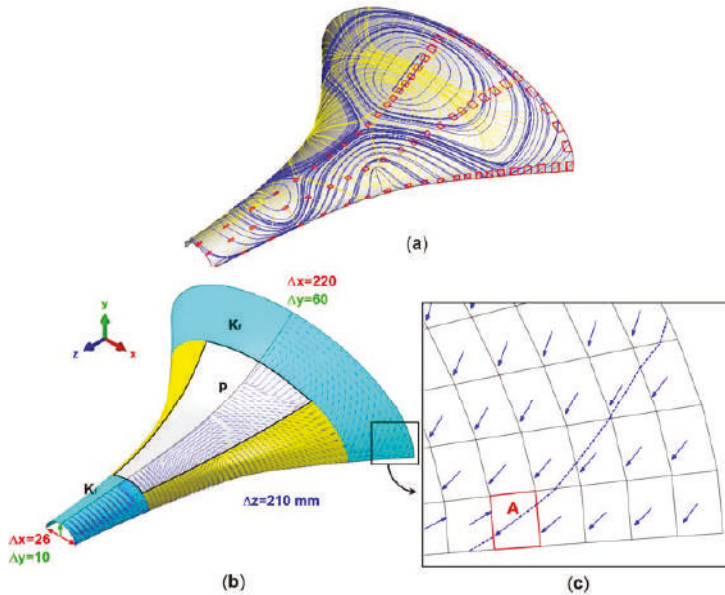


Figure 1. Shell under lateral pressure $p = 0.15$ MPa, bedded elastically ($K_f = 1000$ N/mm); typical dimensions Δx , Δy , and Δz , modulus $E = 50$ GPa, thickness $t = 2$ mm. (a) stress trajectories, standard integration begins in the red start elements; (b) PS directions from a linear static analysis; (c) detail, standard integration begins in element A. Improved accuracy is gained with mesh refinement.

Delmarcelle [3,4] investigated symmetric tensor fields by studying their topological structure. The basic constituents of tensor topology are the degenerate points where eigenvalues (or principal stress values) are equal to each other. Separatrices and degenerate points are the basic constituents of tensor field topology. A separatrix is the tensor line (PS line) between two degenerate points. Knowledge of the topological structure of tensor fields is important, as standard integration methods need this information.

With standard integration methods the uniform distribution of tensor lines depends critically on the placement of starting points (elements), see Figure 1. Jobard’s algorithm [5] for the placement of evenly-spaced PS lines (in his paper: streamlines) is based on a separating distance between adjacent PS lines to control their density. If a PS line is too close to another one, it is abruptly cut. With respect to fiber placement in FRP construction this may have adverse consequences. Trichoche [6] extends the work of Delmarcelle [3,4] to broaden the scope of topology-based vector and tensor field visualization. One focus in his work is on turbulent flows. The streamline distribution is extremely complex for turbulent flows with its local, small-scale details. Another focus is instabilities in structural problems.

Visualization of stress trajectories should permit detection and identification of bifurcation to provide insight into the time-dependent structural evolution. These issues are beyond the scope of this paper.

All these papers lead to specialized algorithms, which are not public. Therefore, it is desirable to investigate the possibilities of integrating vectorial and tensorial direction fields within FE programs without programming efforts or additional software. PS lines in FRP constructions are of particular interest since fiber courses, which follow the local PS directions, make use of the superior stiffness and strength properties of the fibers [1,7–10].

To demonstrate some disadvantages with conventional standard integration methods, Figure 1 shows an integration procedure developed by the author [1] (p. 16) applied to the bottom of a shell structure.

Figure 1b shows the PS directions of the blue principal stress trajectories on the bottom of the shell. In the middle plane and on the top of the shell there are other PS directions since membrane and bending stresses occur simultaneously. These directions stem from an eigenvalue problem of the stress tensor, whose eigenvectors (principal stress directions) remain indefinite in the sign. The PS directions can therefore switch the sign from one element to its neighboring element. The integration pattern in Figure 1c takes this problematic situation into account by replacing the direction vector with a bidirectional element. The bidirectional element intersects two opposing element sides and thereby allows the integration to be continued in the two neighboring elements with their directional elements. Each start element (marked in red) in Figure 1a provides two individual fiber courses with the procedure just described, corresponding to the two PS directions. A regular placement of the start elements in no way guarantees a uniform distribution of the PS lines. A homogenization of the fiber courses is achieved only with considerable effort. A further disadvantage of this procedure is immediately apparent; each individual trajectory (fiber) must be calculated separately. Should the designer change the fiber volume ratio for reasons of strength, then the procedure must be repeated from the beginning.

This problem is substantially simplified through the hypothesis set out above, which can be modeled by means of the orthotropic heat conduction in FE programs. Since the two-dimensional direction field of the principal stresses describes a planar stress condition, shells with an arbitrary boundary can also be processed. An additional advantage is that all of the PS trajectories (fiber courses) can be calculated by means of a single thermal analysis. If the fiber volume ratio is subsequently increased, correspondingly more isotherms (fiber courses) are extracted from the existing continuous temperature field.

The recommended calculation alternative for the integration of $y' = f(x,y)$ is based on the drastically changing properties of Fourier's law for $k_1/k_2 \rightarrow \infty$. The following section provides a mathematical verification of the hypothesis set out above. The practicability of the integration method is based on independence from thermal boundary conditions; the isotherms always follow the direction field in nonsingular areas. However, the (weighted) distance of the isotherms from each other is influenced by the boundary conditions and can be controlled by them. In Section 3, the procedure is based on some rules and these are demonstrated practically through examples. The influence of the orthotropy ratio k_1/k_2 , as well as the influence of singularities on the course of the isotherms, is investigated.

2. The Integration of Direction Fields by Means of the Orthotropic Heat Equation

The direction field is given through an ordinary differential equation of the first order in the Cartesian coordinate system (x,y) :

$$y' = f(x,y). \tag{1}$$

In accordance with the hypothesis in the previous section, it shall be demonstrated that orthotropic heat conduction can be used for the integration of this equation.

2.1. The Anisotropic Fourier Heat Conduction Law and the Heat Conduction Equation

Verification of the hypothesis: In the two-dimensional case, Fourier’s anisotropic heat conduction law with respect to a Cartesian coordinate system is given by Equation (2), and the steady heat balance without internal heat sources by Equation (3), [11]:

$$q_x = -\left(k_{xx} \frac{\partial T}{\partial x} + k_{xy} \frac{\partial T}{\partial y}\right), \tag{2a}$$

$$q_y = -\left(k_{yx} \frac{\partial T}{\partial x} + k_{yy} \frac{\partial T}{\partial y}\right), \tag{2b}$$

$$\frac{\partial q_x}{\partial x} + \frac{\partial q_y}{\partial y} = 0. \tag{3}$$

These equations are combined, resulting in the anisotropic heat conduction equation:

$$\frac{\partial}{\partial x} \left(k_{xx} \frac{\partial T}{\partial x}\right) + \frac{\partial}{\partial x} \left(k_{xy} \frac{\partial T}{\partial y}\right) + \frac{\partial}{\partial y} \left(k_{yx} \frac{\partial T}{\partial x}\right) + \frac{\partial}{\partial y} \left(k_{yy} \frac{\partial T}{\partial y}\right) = 0. \tag{4}$$

Orthotropic (principal) thermal conductivities k_1 and k_2 being oriented according to the direction field of Equation (1) should be transformed into the Cartesian system. The transformation equations for the 2D heat conduction tensor are analogous to a 2D stress tensor, and can be illustrated using trigonometric relationships with Mohr’s (Stress) Circle, as shown in Figure 2.

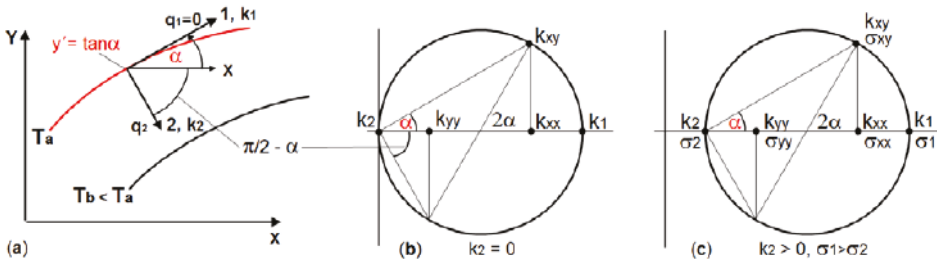


Figure 2. Transformation between local and global conductivity tensors k in the temperature field $T(x,y)$: (a) Angle α and $(\pi/2) - \alpha$ between the local system (1,2) and the global x-axis, \mathbf{q} = heat flux density; (b) Mohr’s Circle for $k_1 > 0$ and $k_2 = 0$; (c) Mohr’s Circle for $k_1 > 0$ and $k_2 > 0$ by analogy with Mohr’s Stress Circle.

$$k_{xx} = k_1 \cos^2 \alpha + k_2 \sin^2 \alpha = \frac{k_1}{1 + \tan^2 \alpha} + \frac{k_2 \tan^2 \alpha}{1 + \tan^2 \alpha} = \frac{k_1}{1 + f^2} + \frac{k_2 f^2}{1 + f^2}, \tag{5a}$$

$$k_{xy} = k_{yx} = (k_1 - k_2) \sin \alpha \cos \alpha = (k_1 - k_2) \frac{f}{1 + f^2}, \tag{5b}$$

$$k_{yy} = k_1 \sin^2 \alpha + k_2 \cos^2 \alpha = \frac{k_1 f^2}{1 + f^2} + \frac{k_2}{1 + f^2}. \tag{5c}$$

The hypothesis in Section 1 is based on extreme orthotropic conductivity ratios, $k_1/k_2 \rightarrow \infty$ and therefore can be validated only for $k_2 = 0$. Setting $k_2 = 0$ in Equation (5) and substituting the simplified expression in Equation (2) we have:

$$q_x = -\left(k_1 \frac{\partial T}{\partial x} + k_1 f \frac{\partial T}{\partial y}\right) / (1 + f^2), \tag{6a}$$

$$q_y = -\left(k_1 f \frac{\partial T}{\partial x} + k_1 f^2 \frac{\partial T}{\partial y}\right) / (1 + f^2). \tag{6b}$$

The heat conduction Equation (4) is solved in the FE programs. Substitution of Equation (5) into (4), together with $k_2 = 0$, results in:

$$\frac{\partial}{\partial x} \left(\frac{k_1}{1 + f^2} \frac{\partial T}{\partial x} \right) + \frac{\partial}{\partial x} \left(\frac{k_1 f}{1 + f^2} \frac{\partial T}{\partial y} \right) + \frac{\partial}{\partial y} \left(\frac{k_1 f}{1 + f^2} \frac{\partial T}{\partial x} \right) + \frac{\partial}{\partial y} \left(\frac{k_1 f^2}{1 + f^2} \frac{\partial T}{\partial y} \right) = 0. \tag{7}$$

The solution $T(x,y)$ of Equation (7) can be visualized by isotherms, which represent a direction field y'_T . An isotherm is characterized by a constant temperature C . Its equation in implicit form is given by $F(x,y) = T(x,y) - C = 0$. A directional element of this curve has the slope:

$$y'_T = -\frac{\partial F / \partial x}{\partial F / \partial y} = -\frac{\partial T / \partial x}{\partial T / \partial y}. \tag{8}$$

The question arises as to which properties Equation (6) shows if the direction fields from Equations (1) and (8) are equated:

$$y' = f(x,y) = f = -\frac{\partial T / \partial x}{\partial T / \partial y} = y'_T, \text{ i.e., } f = -\frac{\partial T / \partial x}{\partial T / \partial y}. \tag{9}$$

Use of “ f ” from Equation (9) in the numerators of Equation (6) results in:

$$q_x = -\left(k_1 \frac{\partial T}{\partial x} + k_1 \left(-\frac{\partial T / \partial x}{\partial T / \partial y}\right) \frac{\partial T}{\partial y}\right) / (1 + f^2) = 0, \tag{10a}$$

$$q_y = -\left(k_1 \left(-\frac{\partial T / \partial x}{\partial T / \partial y}\right) \frac{\partial T}{\partial x} + k_1 \left(-\frac{\partial T / \partial x}{\partial T / \partial y}\right)^2 \frac{\partial T}{\partial y}\right) / (1 + f^2) = 0. \tag{10b}$$

The first and second term for q_x and q_y cancel out, and the right hand sides in Equations (10a) and (10b) become zero. Back-substitution of $(\partial T / \partial x) / (\partial T / \partial y) = -f$ into Equation (10) results in:

$$q_x = q_y = \frac{\partial T}{\partial x} + f \frac{\partial T}{\partial y} = 0. \tag{11}$$

For this extreme case ($k_2 = 0$), both heat flux components $[q_x, q_y] = \mathbf{q}$ are identical to zero. Therefore, the heat flux components q_1 and q_2 parallel to the orthotropic (principal) thermal conductivities (k_1, k_2) in Figure 2a are also zero. The resulting isotherms do not contradict their definition; the heat flux along an isotherm is zero and, perpendicular to this, the heat flux is also zero due to $k_2 = 0$, and the equating of Equations (1) and (8) was justified: If the heat fluxes are zero for any direction field $y' = f(x,y)$, then their divergence $\text{div}(\mathbf{q})$ in the form of Equation (3) or (4) is also zero. The latter is the heat conduction equation, which is solved in FE programs for steady-state problems without internal heat sources. From Fourier’s law with the unknowns T and \mathbf{q} , a directly solvable equation has been formed for T alone provided that $k_2 = 0$. Whether the orthotropic heat conduction problem in Equation (11) is solved, which is not generally available as a calculation option in FE programs, or Equation (7) is solved by means of an FE program, the same isotherms result and are tangential to the given direction field $y' = f(x,y)$. Whenever $k_2 > 0$, the proof does not work.

2.2. The Relationship between the Isotherms of Extremely Orthotropic Heat Conduction and the Characteristics of a Partial Linear Differential Equation of the First Order

A linear partial differential equation of the first order is:

$$A(x,y) \frac{\partial T}{\partial x} + B(x,y) \frac{\partial T}{\partial y} = 0 \tag{12}$$

and is discussed in detail in the literature [12–14]. The required function $T(x,y)$ depicts a surface in three-dimensional space. The theory of the “characteristic method” [12–14] for solving Equation (12) implies that its characteristics are the contour lines of $T(x,y)$ and can be calculated with the ordinary differential equation:

$$\frac{dy}{dx} = B(x, y) / A(x, y) \tag{13}$$

with $A \neq 0$. The similarity of Equations (11) and (12) is obvious for $A = 1$:

$$\frac{\partial T}{\partial x} + B \frac{\partial T}{\partial y} = \frac{\partial T}{\partial x} + f \frac{\partial T}{\partial y} = 0. \tag{14}$$

Along the characteristics, the solution variable T is constant. Therefore, they can be interpreted as isotherms. Equation (14) physically describes the convective transport of the T variable. Equation (12) is valid for a partial differential equation with two independent variables. If x and y are used, then there is a time-independent situation in 2D space. If x is used and t instead of y , then there is a time-dependent situation in 1D space, the latter associates the transport character of Equation (12). A simple transport equation reads [12]:

$$\frac{\partial T}{\partial t} + u \frac{\partial T}{\partial x} = 0 \tag{15}$$

with time t and the convection velocity $u = dx/dt$. The variable T represents temperature here; it could also stand for mass, momentum, or energy. In order to demonstrate the particular properties of Fourier heat conduction ($k_2 = 0$) in a simple example, $f = y' = 1$ is substituted in Equation (11) and $u = 1$ in Equation (15). Therefore, both equations are formally identical. The location variable y in Equation (11) corresponds to the time variable t in Equation (15), y and t are interchangeable. By simple integration of Equation (13), $dy/dx = f = 1$, the isotherms are represented by the straight lines $y = x + C$. Figure 3 shows the corresponding solution for Equations (11) and (15), which was obtained with the FE program ABAQUS (Dassault Systèmes, Vélizy-Villacoublay, France).

The initial condition for $T(t = 0, x_0 \leq x \leq x_1)$ and $T(y = 0, x_0 \leq x \leq x_1)$ is given by a parabolic temperature distribution. The orientation of k_1 is given by the vector (1, 1) in the entire solution area. Extreme orthotropy is achieved by zero-setting of k_2 whereby k_2 is perpendicular to k_1 .

The isotherms in Figure 3 depict both the general solution for the two-dimensional Equation (11) in the x - y plane as well as the time-dependent solution for the one-dimensional Equation (15) in the x - t plane. The isotherms follow the direction field $y' = 1$, not only inside the rectangular area but also on the boundary.

The hypothesis in Section 1 restricts usage to steady state problems. If the FE user investigates the behavior of the (extreme) orthotropic heat conduction beyond this restriction also in the time domain (with three independent variables: x, y, t), then the isotherms are no longer parallel to the specified direction field for finite times. The parabolic start temperature distribution propagates, corresponding to the thermal diffusivity $a = k_1/(c\rho)$ with finite velocity ($c =$ specific heat, $\rho =$ density). As can be seen from Figure 4, the illustratively plotted $0.01 \cdot T_{\max}$ -isotherms at time $t_1 < t_2 < t_3$ are not parallel to the direction field $y' = 1$. This only applies for the steady-state case when $t \rightarrow \infty$.

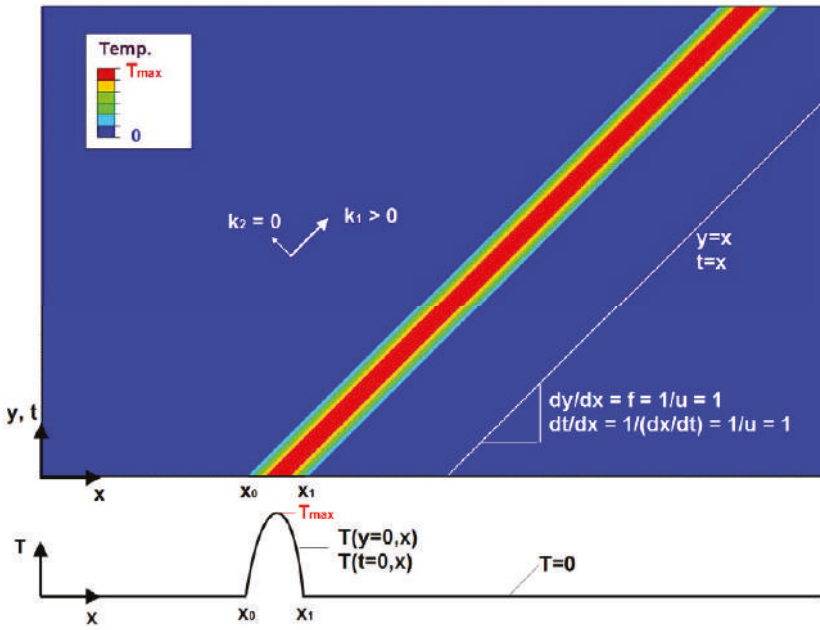


Figure 3. The Fourier heat conduction equation with $k_1/k_2 \rightarrow \infty$ is hyperbolic and has transport character. The diagram is valid for the x-y plane as well as for the x-t plane. As an example, the direction field $y' = f(x,y) = 1$ is integrated with the orthotropic heat conduction ($k_2 = 0$).

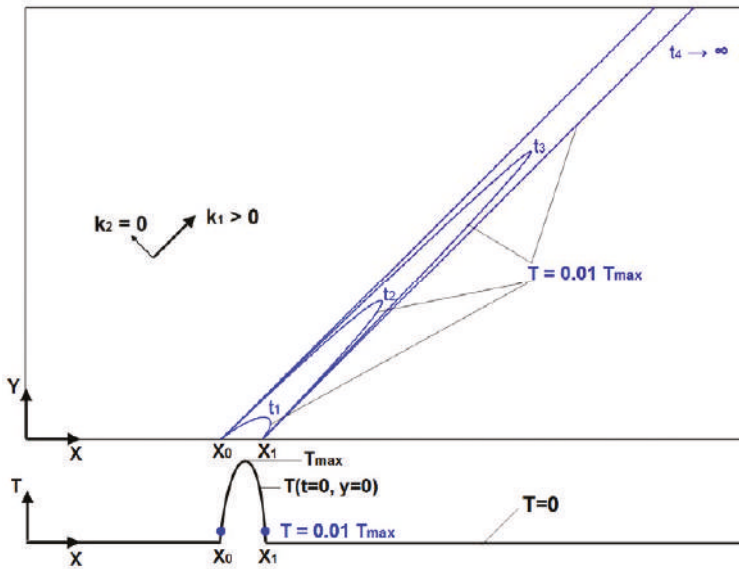


Figure 4. The steady-state problem from Figure 3 analyzed in the time domain. The isotherms are parallel to the given direction field $y' = 1$ only for the final steady state when $t \rightarrow \infty$.

2.3. Temperature Boundary Conditions for Extremely Orthotropic Heat Conduction

The Equations (4) and (7) are solved in FE programs. These are second order and require Dirichlet or Neumann boundary conditions. Non-specified conditions at the boundary include $\partial T/\partial n = \mathbf{q} = 0$ (\mathbf{n} = normal vector perpendicular to the boundary). In case of extreme orthotropy when $k_1 > 0$ and $k_2 = 0$, the latter condition is always fulfilled according to Equation (11) both internally as well as on the boundary; therefore, in principle, no further conditions need to be specified. However, without specification of a reference temperature, the FE solution is singular. If a reference temperature T_{ref} is specified at an arbitrary node, we only obtain the trivial solution $T(x,y) = T_{ref}$. Therefore, at least two different temperatures at two different nodes need to be specified in order to obtain a non-trivial solution. All temperature boundary conditions, which are specified at two or more nodes, provide isotherms that are tangential to the given direction field $y' = f(x,y)$. The difference between a two-node and a multiple-node boundary condition manifests itself through different weightings with respect to the location of the isotherms. In order to obtain appropriate solutions, the direction field must be viewed in connection with the physical task, see Figure 5. This figure shows a disc (half-model) with an elliptical hole under pure bending.

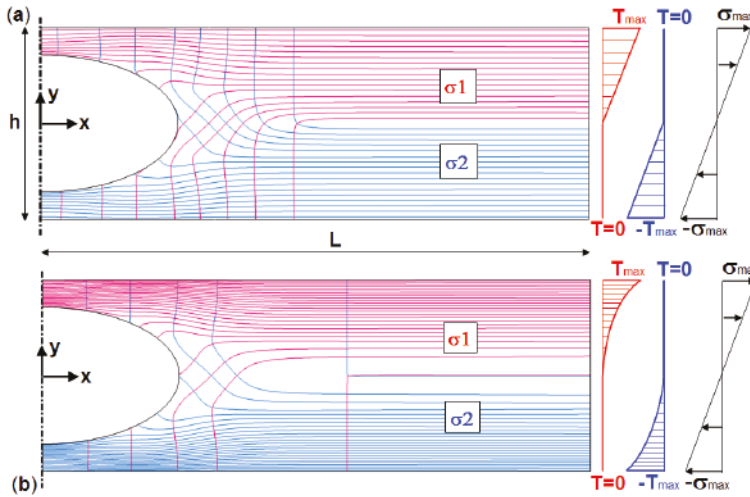


Figure 5. FRP disc with hole under bending: (a) Linearly increasing temperature boundary conditions for σ_1 and σ_2 trajectories yield a uniform distribution of fibers (isotherms); (b) parabolic temperature boundary conditions yield a weighted distribution of fibers, which carries a bending moment more effectively.

From a practical point of view, FRP constructions should have a uniform fiber placement. This is achieved with an orthotropic heat conduction analysis, specifying a linear temperature distribution for $y > 0$ along the right boundary (Figure 5a). The isotherms, as representatives of the σ_1 trajectories, are then distributed equidistantly. For $y < 0$, $T = 0$ is defined. The σ_2 trajectories are calculated in a further orthotropic heat conduction analysis. These require a linear temperature distribution for $y < 0$ and $T = 0$ for $y > 0$. Both isotherm images are superimposed and result in the two fiber layers in Figure 5a.

Should the objective be concentrated on load-related fiber placement, then a linear weighted distribution of isotherms is achieved by defining a parabolic temperature distribution for $y > 0$ (σ_1 trajectories) and $y < 0$ (σ_2 trajectories) along the right boundary; see Figure 5b.

The two-node temperature boundary condition is likewise possible. For example, to determine the σ_1 trajectories, specification of $T(L, h/2) = T_{max}$ and $T(L, 0) = 0$ provides similar results, though the isotherms are not distributed equidistantly on the right boundary; see also Section 3.1.

In Section 2.1 it was shown that in cases of extreme orthotropy ($k_1 > 0, k_2 = 0$), the differential Equation (7) of the second order and the Fourier heat conduction Equation (11) of the first order physically describe the same situation. In Section 2.2, it was shown that the Fourier heat conduction Equation (11) can be traced back to the general linear differential Equation (12). The integration of the corresponding characteristic Equation (13) provides characteristics identical to the isotherms in the Fourier heat conduction Equation (11). The theory of the characteristics also includes the treatment of boundary conditions [14], the rules of which can be applied completely to the Fourier heat conduction Equation (14). Figure 6 shows the most important rule.

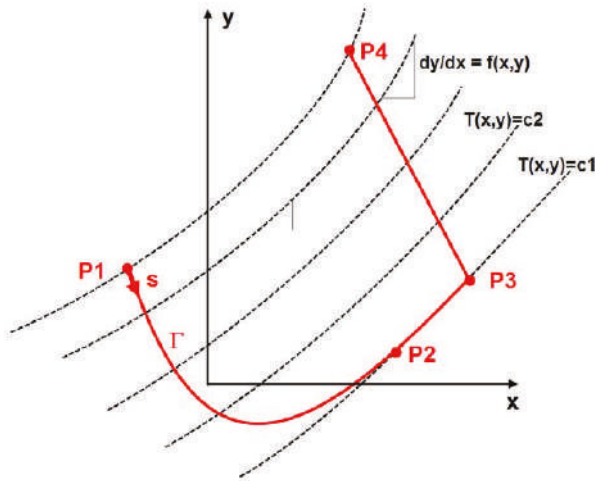


Figure 6. The solution curves $T(x,y)$ of the direction field $y' = f(x,y)$ are simultaneously the characteristics of the Fourier heat conduction Equation (11). The specification of arbitrary boundary conditions along P2P3 is not permitted since this curve is a characteristic or iso-line ($y = \text{const.}$).

According to this, Equation (12) is integrated through the specification of the solution variables T along a curve Γ . However, only the specification on the P1P2 curve is permitted. Since a solution variable is constant on a characteristic, arbitrary specifications along P2P3 are not permitted. Furthermore, arbitrary specifications along P3P4 lead to contradictory definitions with the specifications along P1P2. The curve Γ must not necessarily lie on the exterior boundary, but can also cross the integration area.

3. Procedure and Application Examples

The direction field $y' = f(x,y)$ to be integrated very often originates from FE analysis in the form of PS directions. The procedure for their integration shall be determined with the help of some rules:

1. Calculation of the PS directions in all elements (disc, plate, or shell). If this is not provided by the respective FE program used, they can be calculated via the stress components $[\sigma_{xx} \ \sigma_{yy} \ \sigma_{xy}]$. For example, $y' = dy/dx = \tan \alpha = \sigma_{xy} / (\sigma_{xx} - \sigma_2)$; see also Figure 2c. Plates and shells have variable stresses across the thicknesses. The direction field therefore must be evaluated for every “thickness integration point”.
2. Replacement of the structural elements with thermal elements.
3. Transmission of the PS directions (Step 1) to local systems, depending on the FE program used, (ABAQUS: *Orientation).

4. Assignment of orthotropic thermal conductivities k_1 and k_2 in these local systems with extreme ratios, e.g., $k_1/k_2 > 10^4$. ($k_2 = 0$ is permitted in ABAQUS.)
5. Definition of thermal boundary conditions according to Section 2.3.
6. The ratios $k_1/k_2 > 10^4$ and $k_2/k_1 > 10^4$ provide the PS trajectories for the first and for the second principal stress, respectively.

It should be emphasized that the integration of the PS directions for the calculation of the real fiber course is a separate task, independent of the structural analysis. The PS direction field of the structural calculation is adopted as material orientation for the thermal conductivities in the thermal analysis. The boundary conditions are independent in both analyses and have nothing in common with each other.

3.1. Influence of the Orthotropy Ratio k_1/k_2 on the Integration Accuracy

The influence of the orthotropy ratio k_1/k_2 on the integration accuracy is demonstrated by the following example. Figure 7 shows a perforated disc under axial tension. Due to symmetry, a quarter model is sufficient ($U_x = 0, U_y = 0$). The supplementary material accompanying this paper includes the ABAQUS input for this example.

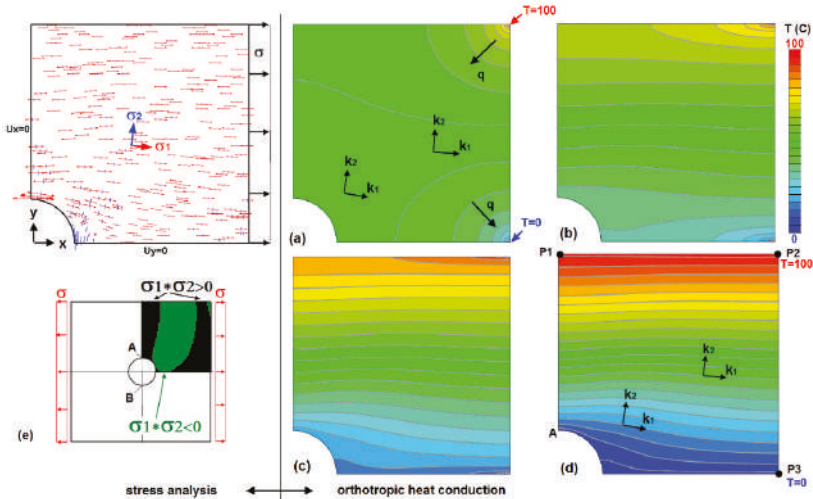


Figure 7. Perforated disc under axial tension and calculation of the PS lines (isotherms) dependent on heat conduction orthotropy k_1/k_2 , where the orientation of k_1 and k_2 corresponds to the PS directions σ_1 and σ_2 : (a) $k_1/k_2 = 1$; (b) $k_1/k_2 = 16$; (c) $k_1/k_2 = 128$; (d) $k_1/k_2 = 4096$; (e) algebraic signs of the two principal stresses; this point is addressed in Section 3.4.

The task is to place the fibers in the direction of the largest principal stress for an FRP construction. The PS directions portray the direction field $y' = f(x,y)$, which shall be integrated. The elements of the mechanical model are replaced with heat conduction elements whose heat conduction k_1 is oriented parallel to the previously calculated PS directions of σ_1 . The k_2 direction is orthogonal to k_1 . Now the ratio k_1/k_2 is successively increased, thus the isotherms get more and more tangential to the PS direction of σ_1 . The influence of the two-node temperature boundary condition at points P2 and P3 (Figure 7d) on the course of isotherms is no longer perceptible for $k_1/k_2 > 10^4$. Under such simple boundary conditions, it must be ensured that their positions are meaningful. If both temperatures are determined at points P1 and P2, then, practically, two different temperatures are defined on one isotherm.

The relatively uniform distribution of the PS trajectories is remarkable, although only a very simple temperature boundary condition was selected. Should the desired outcome be a distribution of isotherms exactly equidistant between P2 and P3, the temperature along this line must be specified as linearly increasing. Since the isotherms represent the fiber course, the constant line load along P3P2 is uniformly carried by the fibers. The maximum load in the perforated disc at points A and B in Figure 7e is approximately three times the applied tension, which is well reflected by the fiber course.

At this point, the transport character of the Fourier heat conduction equation in Figure 7d and Equations (14) and (15) shall be emphasized again. The specification of a linear temperature distribution on the boundary P3P2 is transported along its characteristics without diffusion effects, and these characteristics follow the user defined direction field $y' = f(x,y)$.

3.2. The Influence of Singularities on the Course of the Isotherms

In cases of stress singularities, the following distinctions are made: An isotropic (or neutral) point with an undefined PS direction occurs if the two principal stresses σ_1 and σ_2 are identical. If both principal stresses are zero, then a classic singularity is present. Points with concentrated loads are neither one nor the other. Their isoclines are particularly concentrated at the point of force transmission. What does the course of stress trajectories (represented by isotherms) look like in the vicinity of these points? This can be studied using an example of a circular ring under diametrically opposed single forces. Figure 8a shows the course of the isoclines and stress trajectories that were determined photoelastically by Frocht [15].

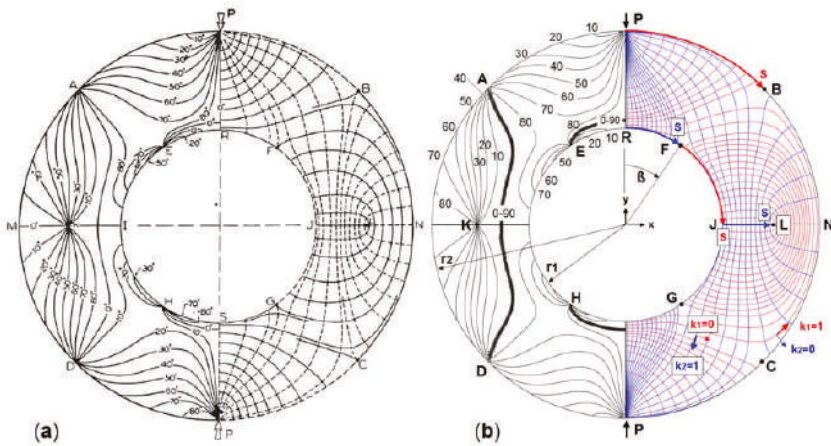


Figure 8. Circular ring under diametrically opposed single forces, $r_2/r_1 = 2$: (a) Photoelastic isoclines (left) and trajectories (right) [15]; (b) Verification with ABAQUS, isoclines (left), σ_1 trajectories and σ_2 trajectories (right).

The experimental results were verified through an FE stress analysis (ABAQUS) followed by an orthotropic heat conduction analysis in order to determine the trajectories, as shown in Figure 8b. Modeling a quarter of the disc is sufficient due to the symmetry. The stress calculation provides the PS directions. In the subsequent heat conduction calculation, these PS directions serve as local systems for the thermal conductivities k_1 and k_2 . Two of these systems are illustratively plotted in the fourth quadrant of Figure 8b. The system $k_1 = 1, k_2 = 0$ provides the isotherms as σ_1 trajectories. With $k_1 = 0, k_2 = 1$, the σ_2 trajectories are determined. The calculation of the isoclines is helpful in order to localize

the singular points A, D, E, H, and K (Figure 8b, left). The isoclines result from Equation (16), i.e., the contour lines of the stress expression on the right side must be visualized; see also Figure 2c.

$$y' = f(x, y) = \tan \alpha = \frac{\sigma_{xy}}{\sigma_{xx} - \sigma_2} = \text{const.} \tag{16}$$

In the trajectories image (right), the singular points appear with the designations B, C, F, G, and L, and are either of the “non-interlocking” type (B, C, F, G) or “interlocking” type (L). This evaluation is useful since a uniform distribution of the isotherms (fibers) is desirable, which is only achievable with knowledge of the singularities. This is shown in Figure 9a for the σ_2 trajectories (with $\sigma_2 < \sigma_1$). A uniform distribution is achieved through a linearly increasing temperature along RF, with continuation along JL.

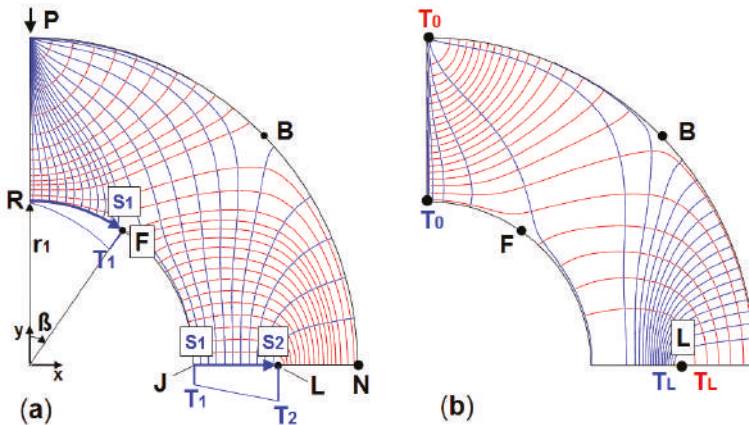


Figure 9. Circular ring analogous to Figure 8: (a) Determination of the σ_2 trajectory through specification of a linearly increasing temperature along RF and JL; (b) Simplified analysis with a two-node temperature boundary condition; T_0 and T_L for the σ_1 trajectories, T_0 and T_L for the σ_2 trajectories.

Specifying a linear increase in temperature from R to J is incorrect since the σ_2 trajectory along RF turns into the σ_1 trajectory at point F along FJ. The FJ boundary segment itself is an isotherm and no variable temperature specification is allowed there.

The existence of a singular point on a load-free boundary of a 2D structure always results in this change of trajectories. This property is responsible for the fact that efforts need to be made regarding the specification of suitable temperature boundary conditions in order to obtain uniformly distributed isotherms. Should the temperature be defined only along RF, then only a part of the structure will show isotherms. A further boundary segment with temperature boundary conditions must then be applied in order to capture the rest of the structure. In Figure 9a, this is segment JL. The procedure is the same when looking for σ_1 trajectories. The temperature is defined as linearly increasing along LN with continuation along LN.

The aim of calculating strictly uniformly distributed isotherms (trajectories) can only be achieved locally. Figure 9a shows uniformly distributed σ_1 trajectories along PB; however, these end up unevenly distributed on the PR boundary.

On the perforated disc (Figure 7), the trajectory change mentioned above does not occur along the right boundary of P2P3. This boundary is free from singularities. The specification of two temperatures at points P2 and P3 is sufficient. We can generally use this simple two-node boundary condition (Section 2.3) for all 2D discs and 3D shells and get—depending on the number

of singularities—correspondingly weighted isotherm distributions. Figure 9b shows this simple procedure for the circular ring with its singularities. The isotherms shown there are less uniformly distributed than in Figure 9a, but this is adequate for a first overview.

The circular ring problem (Figure 8) contains the most important forms of singularities: Isotropic points of the “interlocking” and “non-interlocking” type, as well as concentrated point loads. Errors in representation of isotherms are inevitable since they do not fulfil $y' = f(x,y)$ in the near vicinity of the singularity. In fact, the isotherms in close proximity there evade in a sideways direction depending on the model mesh size. The model in Figure 8b, in comparison to Figure 8a, is clearly fine enough to minimize this error. The element size is virtually the same all over; 60 elements were used (with four nodes respectively) along JN. Through further mesh refinement in the area of singularities, the error can be kept arbitrary small.

3.3. The Principal Stress Trajectories in Shell Structures

A conventional method for the calculation of principal stress trajectories in a shell was shown in Figure 1. Disadvantages resulted from the uneven fiber placement, which originates from the separate calculation of each individual fiber. In integrating the direction field, it is not practically possible to select optimal start positions (start elements) beforehand.

In contrast to this is the method of integration by means of an orthotropic heat conduction calculation. Even with a two-node temperature boundary condition with $Q_0: T = 0\text{ }^\circ\text{C}$, $Q_1: T = 1\text{ }^\circ\text{C}$ in Figure 10a, a better fiber distribution can be attained than is depicted in Figure 1a. This temperature distribution, shown in Figure 10a, provides the approximate position of three local temperature extremes at the positions P_0, P_1 and P_2 .

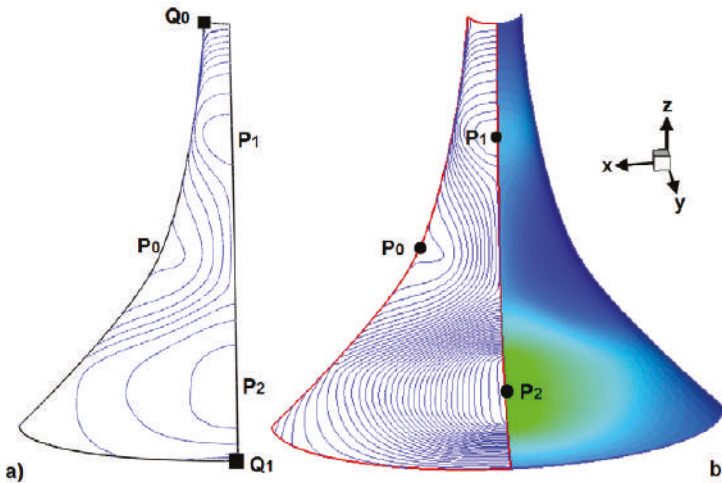


Figure 10. Shell structure analogous to Figure 1: (a) Isotherms with a two-node temperature boundary condition at Q_0 and Q_1 ; (b) Isotherms with a three-node temperature boundary condition at P_0, P_1, P_2 , right: Temperature field for extraction of any number of isotherms (fibers).

By repeating the heat conduction analysis with a three-node temperature boundary condition ($P_0: T = 0\text{ }^\circ\text{C}$, $P_1: T = 1\text{ }^\circ\text{C}$, $P_2: T = 2\text{ }^\circ\text{C}$, Figure 10b), the uniformity of the isotherms is improved. A specification of the linear varying temperatures along boundary segments analogous to the previous section would yield further improvement. However, in light of the result in Figure 10b, it does not appear to be crucial.

The right half of Figure 8b highlights another aspect: The continuous temperature field is infinitely dense with respect to the isotherms, so an arbitrary number of contours can be visualized, avoiding calculation of trajectories one after another (Figure 1).

3.4. Optimization of Fiber Placement in FRP Constructions

In order to demonstrate a useful application beyond the visualization of tensor lines, the fiber placement in FRP constructions is highlighted. Fiber courses, which follow local PS directions, use the superior stiffness and strength properties of the fibers. In plane stress structures the fiber courses due to σ_1 and σ_2 are perpendicular to each other, forming a curvilinear cross-ply (CCP) laminate. With regard to optimality, attention must be paid to the algebraic signs of principal stresses.

Fiber placement in the direction of principal stresses is optimal according to net theory [16], and this is also valid for CCP-laminates if ignoring the support of the matrix. To be on the safe side, the carrying capacity of the construction can be calculated by using a fiber failure criterion. A design based on an inter-fiber failure must additionally take into account the contribution of the matrix. In this case CCP-laminates are optimal only in areas with principal stresses showing different algebraic signs. However, if the algebraic signs are the same, then the curvilinear balanced angle-ply (CBAP) laminate is the better choice according to classical lamination theory [17]. This design differs from the (right-angled) CCP-laminate through a correction angle $\pm\beta$ regarding the σ_1 direction. The direction field y' for the largest principal stress σ_1 is then represented by two direction fields: $y' + \beta$ and $y' - \beta$, as shown in Figure 11.

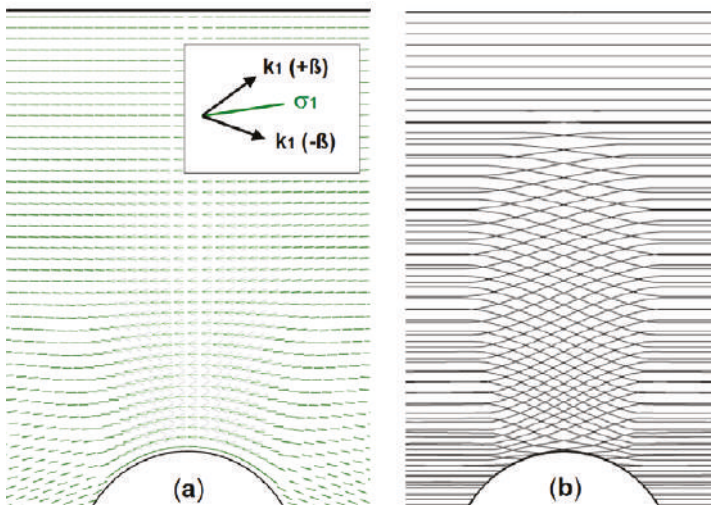


Figure 11. Perforated disc (detail) similar to Figure 7e. In areas with the same principal stress algebraic sign, the CBAP-laminate is optimal: (a) Correction angle $\pm\beta$ regarding the σ_1 direction; (b) Integration of the modified direction field.

For example, the perforated disc (Figure 7e) contains the areas $\sigma_1 \cdot \sigma_2 < 0$ (CCP-laminate is optimal) and $\sigma_1 \cdot \sigma_2 > 0$ (CBAP-laminate is optimal). In the latter case the modified direction fields can also be integrated without restriction by means of the orthotropic heat conduction analysis. The correction angle β is dependent on the material and the principal stress ratio σ_1/σ_2 [17]. It should be noted that the orthotropic heat conduction is suitable for the integration of arbitrary direction fields even if they are modified for reasons determined by the engineer. Reference is made to Moldenhauer [1] (pp. 54–60) and [18] for further details and consideration of particular aspects of load-related optimization (layer

thickness distribution, loading condition range, and nonlinearity of stress distribution over the shell thickness).

4. Discussion and Conclusions

The method presented in this paper is suitable for integrating arbitrary vectorial and tensorial 2D direction fields by means of commercial FE programs, provided that the FE programs have options for the analysis of orthotropic heat conduction. The calculated isotherms represent the integral curves of these direction fields inside and on the edge of the 2D structure (disc or shell). The procedure is based on some rules (Section 3), which concern only the standard input of the FE program. Additional programming is not required. Two temperatures at two different positions shall be specified as a minimum for thermal boundary conditions. The isotherms arising from this can still run in a non-uniform way. Uniformity is achieved while linearly varying temperatures along a boundary segment are specified (Figure 5a). Should the direction field or the differential equation $y' = f(x,y)$ exhibit singularities on the boundary, then the definition of the boundary conditions must be carefully adjusted (Figure 9). In this case, a preliminary visualization of the isoclines, Equation (16), and/or an analysis with the two-node temperature boundary condition is helpful. The precision of the integration depends on the element size of the FE model.

In comparison with the traditional integration methods, significant improvements arise with the new procedure:

- The integration of the direction fields can take place with standard FE programs with options for an orthotropic heat conduction analysis. No additional programming is necessary.
- Any number of isotherms can be extracted from the integrated continuous temperature field.
- Quick and accurate results are obtained with a simple two-node temperature boundary condition; however, the distribution of isotherms may be non-uniform if singular points are present in the direction field.
- As the computed temperature field is continuous, valuable additional information can be extracted from this field. For example, the density of the isotherms (tensor lines) can be computed by displaying the temperature gradients, see [1] (p. 96).
- Applying the proposed integration method to stress tensors it should be noted that principal stress direction fields can originate from linear or nonlinear analyses, see [1] (p. 74). If principal shear stress (or strain) directions are evaluated in the plastic range then the trajectories can be regarded as slip-lines, see [1] (pp. 41–44).
- Civil engineering: Aligning reinforcement in concrete structures parallel to PS directions is a meaningful tool to effectively increase the low tension strength of concrete, see also [1] (p. 78).

Mathematical aspects were the focus of this paper. An important application seems to be on FRP constructions. Aligning fiber courses along PS lines make the most of the superior stiffness and strength properties of fibers. Calculation of these fiber courses by integrating the PS directions followed by the evaluation of this optimized FRP design can be done with one and the same FE program. To evaluate and optimize an FRP construction based on PS lines, some practical aspects should be highlighted.

As with all FRP problems, the optimization success is greatest when a special load case is investigated. In reality, loads and boundary conditions change frequently, and the principal stress directions change accordingly. However, the associated degradation of the optimization method affects alternative optimization strategies as well. If one load case dominates other load cases, the optimization effort can be worthwhile nevertheless. A CCP- or CBAP-laminate can be combined with textile preforms and can be stitched onto standard laminates. This technique is known as tailored fiber placement (TFP). The layer with the fiber course aligned to the trajectories covers the critical load case, and the standard laminate the other load cases. In 2D, the TFP stitching technique has been used for a long time [10]. In 3D, textile preforming or tape laying are possible options.

The effort for the proposed method appears to be very high in the case of plates and shells, since the PS directions for superimposed membrane and bending stress vary across the thickness. The integration of the stress components $[\sigma_{xx} \sigma_{yy} \sigma_{xy}]$ over the thickness produces normal forces $N = [N_{xx} N_{yy} N_{xy}]$ and bending moments $M = [M_{xx} M_{yy} M_{xy}]$. FE programs generally provide these section forces and moments N and M , which are both constant across the thickness. Their principal directions (1,2) can be computed in analogy to Equation (16), i.e., $y_1' = N_{xy}/(N_{xx} - N_{yy})$, $y_2' = -1/y_1'$. It makes sense to arrange the M-layers on the inside and outside and the N-layers in the middle of the shell. Symmetric layers are then obtained with $[M_1/M_2/N_1/N_2]_S$, see also [1] (pp. 64–73).

When evaluating a TFP laminate, one is faced with the variable fiber volume fraction due to the diverging and converging streamline nature of the fiber course. The fiber volume fraction is an important input quantity to define laminate stiffness with dependence on local fiber volume and local fiber orientation. The gradient of the temperature field is a measure for the local fiber volume. Displaying the gradient of the temperature field is identical to displaying the isotropic heat flux, $\mathbf{q} = k \cdot \text{grad}(T)$ with $k = k_1 = k_2$. For extreme orthotropy ($k_1/k_2 \rightarrow \infty$) we have an orthotropic heat flux, which is zero everywhere, see Equation (11). If the temperature field is based on isotropic conduction with constant k , then the isotropic heat flux is the correct gradient. For this reason, the nodal temperatures from the orthotropic analysis must be used as prescribed nodal temperatures in an additional thermal run. More details can be found in [1] (p. 96).

Provided that the course of the isotherms (trajectories) shall be used for fiber placement in FRP constructions, the visualized isotherms must be converted into polylines with x-, y-, and z-coordinates. TECPLOT (Bellevue, WA, USA) is suitable as a commercial solution for this. Alternatively, a Fortran program can be used, for which the source code is contained in DeVries [19].

Supplementary Materials: The following are available online at <http://www.mdpi.com/2297-8747/23/2/24/s1>.

Funding: This research received no external funding.

Conflicts of Interest: The author declares no conflict of interest.

References

1. Moldenhauer, H. Die Orthotrope Wärmeleitung als Numerischer Integrator Allgemeiner Richtungsfelder mit Anwendung zur Optimalen Faserplatzierung und Kraftflussvisualisierung. Available online: <https://publikationen.bibliothek.kit.edu/1000060087> (accessed on 4 May 2018).
2. Beyer, F.R. Hauptspannungstrajektorien in der numerischen Festkörpermechanik—Ein Algorithmus zur Visualisierung der Bauteilbeanspruchung in zwei und drei Dimensionen. Available online: <http://nbn-resolving.de/urn:nbn:de:bsz:14-qucosa-178497> (accessed on 4 May 2018).
3. Delmarcelle, T. The Visualization of Second-Order Tensor Fields. Ph.D. Thesis, Stanford University, Stanford, CA, USA, December 1994.
4. Delmarcelle, T.; Hesselink, L. The Topology of Second-Order Tensor Fields. Available online: https://graphics.ethz.ch/teaching/scivis_common/Literature/DelmarcelleHesselink94.pdf (accessed on 4 May 2018).
5. Jobard, B.; Lefer, W. Creating Evenly-Spaced Streamlines of Arbitrary Density. In Proceedings of the 8th Eurographics Workshop on Visualization in Scientific Computing, Boulogne-sur-Mer, France, 28–30 April 1997; pp. 44–55.
6. Tricoche, X. Vector and Tensor Field Topology Simplification, Tracking and Visualization. Ph.D. Thesis, University of Kaiserslautern, Kaiserslautern, Germany, April 2002.
7. Hyer, M.W.; Charette, R.F. Use of Curvilinear Fiber Format in Composite Structure Design. *AIAA J.* **1991**, *29*, 1011–1015. [CrossRef]
8. Mattheck, C. *Design in Nature*; Springer: Berlin, Germany, 1998.
9. Tosh, M.W.; Kelly, D.W. On the Design, Manufacture and Testing of Trajectorial Fibre Steering for Carbon Fibre Composite Laminates. *Composites Part A Appl. Sci. Manuf.* **2000**, *31*, 1047–1060. [CrossRef]
10. Spickenheuer, A. Zur fertigungsgerechten Auslegung von Faser-Kunststoff-Verbundbauteilen für den extremen Leichtbau auf Basis des variabelaxialen Fadenablageverfahrens Tailored Fiber Placement. Available online: <http://nbn-resolving.de/urn:nbn:de:bsz:14-qucosa-147748> (accessed on 4 May 2018).

11. Hahn, D.W.; Özişik, M.N. *Heat Conduction*, 3rd ed.; John Wiley and Sons: Hoboken, NJ, USA, 2012; p. 625.
12. Hoffman, J.D. *Numerical Methods for Engineers and Scientists*, 2nd ed.; Marcel Dekker: New York, NY, USA, 2001; pp. 501–526.
13. Riley, K.F.; Hobson, M.P.; Bence, S.J. *Mathematical Methods for Physics and Engineering*, 3rd ed.; Cambridge University Press: Cambridge, UK, 2006; pp. 675–706.
14. Pinchover, Y.; Rubinstein, J. *An Introduction to Partial Differential Equations*, 3rd ed.; Cambridge University Press: Cambridge, UK, 2005; pp. 23–36.
15. Frocht, M.M. *Photoelasticity*; John Wiley and Sons: New York, NY, USA, 1946; Volume 1, pp. 209–210.
16. Schürmann, H. *Konstruieren mit Faser-Kunststoff-Verbunden*, 2nd ed.; Springer: Berlin, Germany, 2007; pp. 451–476.
17. Michaeli, W.; Huybrechts, D.; Wegener, M. *Dimensionieren mit Faserverbundkunststoffen*; Hanser: Munich, Germany, 1994; pp. 107–119.
18. Moldenhauer, H. Beanspruchungsgerechte Faserplatzierung in Faser-Kunststoff-Verbunden. *Konstruktion* 2017, 69, 68–74.
19. DeVries, P.L. *Computerphysik*; Spektrum Akademischer Verlag: Heidelberg, Germany, 1994; pp. 417–420.



© 2018 by the author. Licensee MDPI, Basel, Switzerland. This article is an open access article distributed under the terms and conditions of the Creative Commons Attribution (CC BY) license (<http://creativecommons.org/licenses/by/4.0/>).

MDPI
St. Alban-Anlage 66
4052 Basel
Switzerland
Tel. +41 61 683 77 34
Fax +41 61 302 89 18
www.mdpi.com

Mathematical and Computational Applications Editorial Office
E-mail: mca@mdpi.com
www.mdpi.com/journal/mca



MDPI
St. Alban-Anlage 66
4052 Basel
Switzerland

Tel: +41 61 683 77 34
Fax: +41 61 302 89 18

www.mdpi.com



ISBN 978-3-0365-0137-6